

Silicon Based Mirror Coatings For Gravitational Wave Detectors

**Dissertation
zur Erlangung des Doktorgrades
an der Fakultät für Mathematik, Informatik und Naturwissenschaften
Fachbereich Physik
der Universität Hamburg**

**vorgelegt von
Lukas Terkowski**

Hamburg

2022

Gutachter/innen der Dissertation:	Prof. Dr. Roman Schnabel Prof. Dr. Oliver Gerberding
Zusammensetzung der Prüfungskommission:	Prof. Dr. Roman Schnabel Prof. Dr. Oliver Gerberding Prof. Dr. Wolfgang Parak Prof. Dr. Michael Thorwart Dr. Jessica Steinlechner
Vorsitzende/r der Prüfungskommission:	Prof. Dr. Wolfgang Parak
Datum der Disputation:	02.09.2022
Vorsitzender Fach-Promotionsausschusses PHYSIK:	Prof. Dr. Wolfgang Parak
Leiter des Fachbereichs PHYSIK:	Prof. Dr. Günter H. W. Sigl
Dekan der Fakultät MIN:	Prof. Dr. Heinrich Graener

“For centuries, science has beaten back the shrouds of ignorance. And knowing what is really true is the only way we have been able to make progress.”

Derek Muller

Abstract

The detection of gravitational waves opened a novel astronomic and cosmic observation window into the universe. The existing gravitational wave detectors have already provided various scientific results, but so far many questions have remained unanswered. For an in-depth exploration of astrophysical and cosmic sources of gravitational waves, detectors with higher sensitivities are required.

Current detectors are based on large laser interferometers with suspended mirrors, whose distance briefly and periodically changes upon arrival of a gravitational wave. To increase the sensitivity, the thermal noise of the mirror coatings should, among other things, be reduced. Due to large mechanical losses, the materials used so far have only a limited suitability. Thus, alternative materials and techniques for mirror coatings are required. Amorphous silicon as a coating material offers significant potential for a thermal noise reduction. However, in order to utilise amorphous silicon, its optical absorption has to be reduced. Overall, the use of different silicon based technologies could achieve a reduction in thermal noise of at least 32 % at room temperature compared to currently used coatings. Even further improvements can be expected at cryogenic temperatures.

In this thesis, I show how silicon based coatings can potentially be used for the main mirrors of gravitational-wave detectors. I have studied the behaviour of amorphous silicon for different deposition parameters and gained insights into the reduction of optical absorption and the mechanisms behind it. Furthermore, the properties of so called nanolayers consisting of amorphous silicon and silicon dioxide were examined. The background is a possible influence of the layer thickness on the undesirable crystallization caused by the usual heat treatment of coatings. Utilising various bonding and removal techniques, crystalline silicon could form a single, uppermost layer for the mirrors, which was, within the scope of this thesis, applied and investigated for the first time in this field of research. This technology could significantly improve the optical and mechanical properties of the main detector mirrors. However, further steps are required beforehand, such as the production of a complete mirror demonstrator. The investigations carried out in this thesis contribute to the current research, so that the potential improvement in thermal noise by the utilisation of silicon can be fully exploited.

Kurzfassung

Die Detektion von Gravitationswellen öffnet ein neuartiges astronomisches und kosmisches Beobachtungsfenster ins Universum. Die existierenden Gravitationswellendetektoren haben bereits diverse wissenschaftliche Erkenntnisse erbracht, jedoch blieben bisher viele Fragestellungen unbeantwortet. Für eine tiefgehende Erforschung astrophysikalischer und kosmischer Quellen von Gravitationswellen werden Detektoren mit höheren Sensitivitäten benötigt.

Derzeitige Detektoren basieren auf großen Laserinterferometern mit aufgehängten Spiegeln, deren Abstand sich beim Eintreffen einer Gravitationswelle kurzzeitig periodisch ändert. Zur Erhöhung der Empfindlichkeit soll, unter anderem, das thermische Rauschen der Spiegelbeschichtungen verringert werden. Aufgrund großer mechanischer Verluste sind bisher verwendete Materialien nur begrenzt dazu geeignet und alternative Materialien sowie Techniken für Spiegelbeschichtungen werden daher benötigt. Amorphes Silicium als Beschichtungsmaterial bietet ein erhebliches Potential zur Verringerung des thermischen Rauschens. Allerdings muss zur dessen Verwendung die optische Absorption verringert werden. Insgesamt könnte durch den Einsatz unterschiedlicher siliciumbasierter Technologien eine Reduktion des thermischen Rauschens um mindestens 32 % bei Raumtemperatur gegenüber heute verwendeten Beschichtungen erreicht werden. Bei kryogenen Temperaturen können sogar weitere Verbesserungen erwartet werden.

In dieser Arbeit zeige ich, wie siliciumbasierte Beschichtungen potentiell für den Einsatz auf den Hauptspiegeln von Gravitationswellendetektoren geeignet sein können. Ich habe das Verhalten von amorphem Silicium für unterschiedliche Depositionsparameter untersucht und Erkenntnisse über die Verringerung optischer Absorption sowie die dahinterstehenden Mechanismen erhalten. Des Weiteren wurden die Eigenschaften von sogenannten Nano-Schichten bestehend aus amorphem Silicium und Siliciumdioxid untersucht. Hintergrund ist ein möglicher Einfluss der Schichtdicke auf die unerwünschte Kristallisation durch die übliche Wärmebehandlung von Beschichtungen. Kristallines Silicium könnte mit Hilfe von verschiedenen Füge- und Abtrage-Techniken eine einzelne, oberste Schicht der Spiegel bilden, was im Rahmen dieser Arbeit erstmals auf diesem Gebiet angewandt und untersucht wurde. Diese Technik könnte die optischen und mechanischen Eigenschaften der Hauptspiegel deutlich verbessern. Allerdings sind vorher weitere Schritte wie die Herstellung eines vollständigen Spiegeldemonstrators erforderlich. Die in dieser Arbeit durchgeführten Untersuchungen tragen dazu bei, dass die potentielle Verbesserung des thermischen Rauschens durch die Verwendung von Silicium möglichst vollständig ausgeschöpft werden kann.

Contents

Abstract	v
Kurzfassung	vii
Contents	ix
List of Figures	xiii
List of Tables	xv
List of Abbreviations	xvii
List of Symbols	xix
1 Introduction	1
2 Gravitational Waves Detection	3
2.1 Basics of Gravitational Waves	3
2.2 Functionality of Gravitational Waves Detectors	4
2.3 Noise Sources	6
2.3.1 Quantum Fluctuations	6
2.3.2 Seismic Vibrations	7
2.3.3 Newtonian Gravity	7
2.3.4 Residual Gas	8
2.3.5 Suspension Thermal Noise	8
2.3.6 Mirror Coating Brownian Noise	8
2.3.7 Mirror Coating Thermo-Optic Noise	9
2.3.8 Mirror Substrate Brownian Noise	9
2.4 Current Detectors	9
2.5 Future Detectors	10
3 Test Mass Mirrors for Gravitational Wave Detectors	13
3.1 Highly Reflective Mirrors	13
3.2 Optical Absorption	16
3.3 Coating Thermal Noise	18
3.4 Multi-Material Coatings	20
3.5 Coating Materials	21

3.5.1	Silicon Dioxide	22
3.5.2	Tantalum Pentoxide	23
3.5.3	Aluminium Trioxide	23
3.5.4	Hafnium Dioxide	24
3.5.5	Mixture of Titanium Dioxide and Germanium Dioxide	24
3.5.6	Amorphous Silicon	25
3.5.7	Silicon Nitride	26
3.5.8	Aluminium Gallium Arsenide	26
4	Photothermal Common-Path Interferometry	29
4.1	Measurement Concept	29
4.1.1	The Signal Formation	29
4.1.2	The Imaging Stage	34
4.2	The Hamburg PCI System	38
4.3	PCI Measurements	40
5	Deposition of Amorphous Silicon Layers	43
5.1	Pulsed Laser Deposition	43
5.1.1	The PLD Process	43
5.1.2	The Hamburg PLD System	45
5.1.3	Sample Production	46
5.2	Analysing Methods	49
5.2.1	Transmission Spectra Analysis	49
5.2.2	Examination of Microscopic Images	53
5.3	Analysis Results	53
5.3.1	Microscopic Crystals	54
5.3.2	Deposition Parameters	55
5.3.3	Deposition Rate	58
5.3.4	Refractive Index	62
5.3.5	Mobility Gap Energy	64
5.4	Discussion	66
5.4.1	Absorption Mechanisms	67
5.4.2	Influences of the Substrate Material	68
6	Amorphous Silicon and Silica Nano-layer Coatings	71
6.1	Introduction to Nano-layers	71
6.2	Characterisation of the Nano-layer Stack	73
6.2.1	Transmission Spectra	73
6.2.2	Optical Absorption	76
6.2.3	Microscopic Images	77
6.3	Discussion and Outlook	78
7	Crystalline Silicon Toplayer	79

7.1	Concept	79
7.2	Sample Production Process	80
7.3	Prototype Samples	81
7.4	Analysis and Discussion	84
8	Conclusion	87
8.1	Summary	87
8.2	Outlook	88
	Appendix	91
A	PCI Simulation Code	93
B	List of Produced aSi Coatings Using PLD	103
C	Resources	107
	Bibliography	109
	Acknowledgements	125
	Eidesstattliche Versicherung / Declaration on oath	127

List of Figures

2.1	Schematic depiction of a basic Michelson interferometer	4
2.2	Schematic depiction of a modified Michelson interferometer used in GWDs	5
2.3	Design sensitivity curve of the Advanced LIGO GWDs	6
3.1	Schematic depiction of light reflected from a single layer coating on a substrate	14
4.1	Schematic depiction of the beam crossing point in the PCI technique	30
4.2	PCI: simulation of the intensity variations of the probe beam after 3 mm	32
4.3	PCI: simulation of the intensity variations of the probe beam as a function of the distance to the beam crossing point	34
4.4	PCI: simulation of the intensity variations of the probe beam as a function of the distance from the beam crossing point to the 1. lens of the imaging stage (butterfly curve)	36
4.5	PCI: simulation of the detected butterfly curve	37
4.6	Schematic depiction of the PCI system at the University of Hamburg	39
4.7	Example absorption measurement by the Hamburg PCI system	40
5.1	The pulsed laser deposition process	44
5.2	Schematic depiction of University Hamburg's PLD system	45
5.3	Transmission spectra of C7980 and C7979 substrates	48
5.4	Depiction of the density of states as described by the OJL model	50
5.5	Examples of Scout fits compared to the measured aSi transmission spectra	52
5.6	Example of a microscopic image of a PLD produced aSi coating and its processing	53
5.7	Scattering of aSi layers as a function of their crystal covered area	54
5.8	Extinction coefficient of aSi layers as a function of various deposition parameters	56
5.9	Extinction coefficient of aSi layers at 1550 nm as a function of the deposition rate	59
5.10	Extinction coefficient of aSi layers at other wavelengths as a function of the deposition rate	61
5.11	Refractive index of aSi layers at 1550 nm as a function of various deposition parameters	63
5.12	Extinction coefficient of aSi layers as a function of their mobility gap energy	65

6.1	Schematic depiction of a nano-layer structure in comparison to an equivalent single layer coating	73
6.2	Wavelength dependent refractive indices of aSi, silica and the virtual fitting material	74
6.3	Examples of Scout fits compared to the measured nano-layer transmission spectra	75
6.4	Optical absorption of the nano-layers at 1064 nm as a function of the heat treatment temperature	76
6.5	Examples of microscopic images of the heat treated nano-layer samples	77
7.1	Schematic depiction of the production process to implement a crystalline silicon toplayer on an amorphous layer stack	80
7.2	Example photos of a bonded prototype cSi toplayer sample	81
7.3	Cross-section of the 3D modelled steel beaker used for etching of the bonded cSi toplayer samples	83
7.4	The cSi toplayer prototype sample after etching	84
7.5	Scout fit compared to the transmission spectrum of the cSi toplayer prototype sample	85

List of Tables

4.1	Basic parameters used for the simulations of the PCI technique	31
4.2	Basic parameters used for the simulations of the effects of the imaging stage	35
5.1	List of analysed aSi coatings produced using PLD	47
B.1	List of disregarded, PLD produced aSi coatings	103
B.2	Complete chronological list of produced aSi coatings using PLD, part 1 . . .	104
B.3	Complete chronological list of produced aSi coatings using PLD, part 2 . . .	105

List of Abbreviations

aLIGO	Advanced LIGO
aSi	amorphous silicon
AdvVirgo	Advanced Virgo
BS	beam splitter
C7979	<i>Corning 7979</i> silica
C7980	<i>Corning 7980</i> silica
CE	Cosmic Explorer
cSi	crystalline silicon
ET	Einstein Telescope
GWD	gravitational wave detector
HR	highly reflective
PCI	photothermal common-path interferometry
ppm	parts per million
RT	room temperature
SLM	standard litre per minute

List of Symbols

a	optical absorption
c	speed of light in the vacuum, $2.997\,924\,58 \times 10^8$ m/s
C_1, C_2	scattering constants of the Scout model
d	thickness
d_c	coating thickness
d_l	thickness of a single coating layer
dn/dT	temperature dependence of the refractive index
e	Euler's number, $\approx 2.718\,282$
E	energy
E_g	mobility gap energy of amorphous silicon
E_p	laser pulse energy
E_w	electric field of an electromagnetic wave
$E_{w,0}$	initial electric field amplitude of an electromagnetic wave
f	frequency
f_p	laser pulse repetition rate
F_g	gas flow rate
i	imaginary unit
J	joint density of states of the OJL model
k	extinction coefficient, imaginary part of the complex refractive index
k_B	Boltzmann constant, $1.380\,649$ J/K
\mathbf{n}	complex refractive index
n	refractive index, real part of the complex refractive index
n_{photon}	average photon number of a light mode
N_v, N_c	distributions of electronic states in the valence and conduction band of an amorphous semiconductor according to the OJL model
P	power
Q	quality factor of an oscillator
R_i	power reflection coefficient for light independent from polarisation
R_p, R_s	power reflection coefficients for parallel and perpendicular polarised light
s	signal generated by a PCI system
S_x	thermal noise power spectral density
t	time
T	temperature
T_i	power transmission coefficient for light independent from polarisation

T_p, T_s	power transmission coefficients for parallel and perpendicular polarised light
w	radius of a Gaussian laser beam at which the intensity dropped to $1/e^2$ of its maximum value at the centre
w_0	waist radius of a Gaussian laser beam
x	position along the x axis
y	position along the y axis
Y	Young's modulus
z	position along the z axis
z_R	Rayleigh length of a Gaussian laser beam
α	angle of incidence for light at the boundary of two media
β	angle of refraction for light at the boundary of two media
γ	material correction factor for PCI measurements
Δs	optical path length difference
ϵ_r	relative, complex-valued dielectric function
ϵ', ϵ''	real and imaginary part of the relative dielectric function
λ	wavelength of light
μ_r	relative magnetic permeability
π	ratio of a circle's circumference to its diameter, $\approx 3.141\ 593$
σ	Poisson's ratio
ϕ	mechanical loss angle
χ	electric susceptibility
ψ	Gouy phase of a Gaussian laser beam
ω	angular frequency

Chapter 1

Introduction

Nearly 100 years after gravitational waves were predicted by Einstein [Ein16b], they were directly detected for the first time on September 14, 2015 by the Advanced LIGO (aLIGO) detectors [Abb16c]. Since then, a multitude of other gravitational wave events have been observed by the aLIGO and Advanced Virgo (AdvVirgo) detectors [Abb21b]. Prior to the detection of gravitational waves, the only means to explore the universe was through recording electromagnetic radiation, from radio waves over the visible spectrum up to gamma rays, and by detecting matter particles such as protons and neutrinos. Gravitational waves however provide another, completely new method to observe the cosmos. The direct detection of gravitational waves was therefore a major breakthrough in modern astronomy, cosmology and general relativity as it opened up a new access to research these areas [Abb17, Abb19a, Abb19b, Abb21a, Abb21c, Abb21d, SS19].

Gravitational waves are ripples in space-time that can cause miniscule length differences in space. Their detection is only possible through the extreme precision of modern gravitational wave detectors. Since their first commissioning in the early 2000s, they have been steadily worked upon to improve their sensitivity [Abb20, Acc11, Bar19]. The ‘heart’ of the detectors are kilometre-scale laser interferometers which continuously measure the distance variations between their main mirrors serving as reference masses. Passing gravitational waves can cause changes in these distances, if the orientation of the waves and the interferometers are correspondingly aligned.

Future gravitational wave detectors are planned to be constructed with even higher sensitivities [Abe11a, Rei19], which requires considerable improvements in several areas. One major concern are the highly reflective main mirrors of the interferometers as their coating thermal noise is a major limiting noise source in the most sensitive frequency range of current detectors [Bar18]. New coating materials are required to sufficiently lower the coating thermal noise. One promising material candidate is amorphous silicon [Ste18b]. However, the relatively high optical absorption of amorphous silicon is restricting to what extent it can be utilised in prospective coatings [Cra19, Ste21]. Therefore, current research aims to lower the absorption of amorphous silicon coatings by modifying their deposition parameters and heat treatment procedures [Bir18, Ste16b]. In addition, advanced coating

techniques like multi-material [Ste15, Yam15] or nano-layered [Pan14] coatings have been major areas of active research to develop improved designs for future coatings.

Another material with excellent properties regarding coatings for gravitational wave detectors is crystalline silicon. Both, the thermal noise and optical absorption are well within the coating requirements of proposed future detectors [Abe11a, Deg13, Hal21, Kee95, McG78, Naw08]. However, crystalline silicon cannot be partnered with amorphous materials in multilayered highly reflective coatings as the crystal structure has to be preserved to grow further layers and a suitable crystalline partner material has yet to be found. Nonetheless, it might be possible to implement a single crystalline silicon toplayer using a special production process, which would already significantly improve the properties of future coatings [Ste16a].

In this thesis, I researched amorphous silicon as a material for coatings of gravitational wave detectors and I investigated the production process to create a crystalline silicon toplayer. In chapter 2, the basics of gravitational waves are discussed. The operation principle of gravitational wave detectors and their different noise types are explained. Afterwards, an overview on the properties of current and future detectors is given. In chapter 3, the test mass mirrors of gravitational wave detectors are discussed. Their general structure, optical absorption and coating thermal noise are explained. The principle of multi-material coatings, as a concept for coating improvement, is briefly described and an overview of the different materials considered for mirrors of gravitational wave detectors is given. In chapter 4, the measurement of optical absorption using photothermal common-path interferometry is explained and the system I set up at the University of Hamburg is described. In chapter 5, my investigation on amorphous silicon coatings produced using pulsed laser deposition is discussed, in order to examine correlations between the deposition parameters and the optical absorption. The analysis techniques employed as well as the results are explained. In chapter 6, I examined nano-layer coatings made of amorphous silicon and silica with the aim to investigate the effect on the crystallisation temperature of the amorphous silicon by reducing the layer thickness. In chapter 7, a world first application of the proposed production process for crystalline silicon toplayers is examined and discussed, with a simplified prototype sample being produced and studied. Finally in chapter 8, I summarise the results of this thesis and give an outlook on further related coating research. In addition, by combining the different discussed materials and techniques, the potential improvements in thermal noise of silicon based mirror coatings over the coatings currently used in gravitational wave detectors is estimated.

Chapter 2

Gravitational Waves Detection

2.1 Basics of Gravitational Waves

According to Einstein's general theory of relativity [Ein16a], space-time is not rigid but can be bent by massive objects, resulting in a local curvature of space-time surrounding the object. If the position of a mass changes, so does the curvature of the space-time in which it resides. This change is not instantaneous but travels at the speed of light. Hence, assuming as an example that masses vary their positions periodically or in other words are periodically accelerated, this results in a propagating, regularly changing curvature of space-time. These ripples of space-time are called gravitational waves [Tho95]. In general, all systems with non rotationally symmetric accelerating masses emit gravitational waves. They manifest themselves by stretching and compressing the space-time in the plane orthogonal to the direction of propagation, resulting in varying distances between resting reference points. The waves are quadrupolar meaning that while space is compressed in one orientation, it is stretched in the orthogonal one. This relative distance variation is known as the strain of the gravitational waves. A mathematically rigorous and more physically in depth description of gravitational waves can be found for example in [Fla05].

The distance variations created by gravitational waves are so miniscule, that only very large, strongly accelerating masses can emit gravitational waves that are strong enough to be measured on Earth. The most prominent sources are the inspiraling and following merging of binary systems of compact objects like black holes or neutron stars. When two compact objects are circling around each other, gravitational waves are emitted as described above. These waves carry some energy, which is lost by the system resulting in a reduction of its kinetic energy [Tho95]. Subsequently, the distance between both objects is reduced, leading to an increase in both frequency and amplitude of the emitted gravitational waves. Eventually, the distance is so small that the objects merge, during which the energy discharge is at its maximum. However, even in these cases, the strain reaching the Earth at most amounts to 10^{-21} at peak output [Abb16b, Abb16c]. Detectors for gravitational waves therefore need to be extremely precise. They are the most sensitive position meters that ever have been created [LIG]. The basics and functionality of gravitational wave detectors are described in the following section.

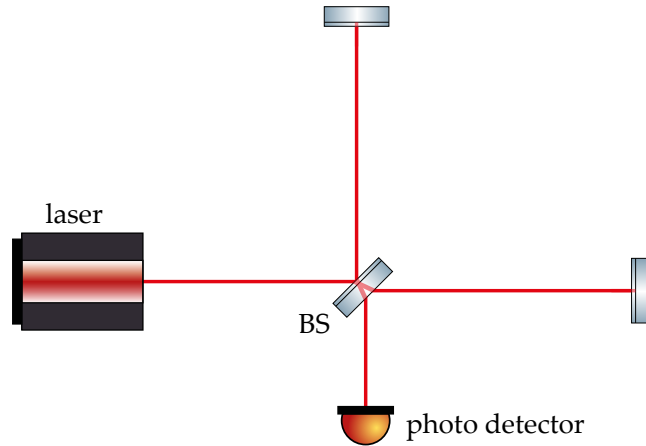


FIGURE 2.1: Schematic depiction of a basic Michelson interferometer.

Gravitational waves are interesting for a variety of astronomical and cosmic studies as they open up a completely new ‘window’ for astronomical observations beyond the electromagnetic spectrum. In addition, they propagate through space completely unobstructed by matter of any kind, so they reveal objects and events hidden from the electromagnetic wave spectrum. This unique combination gives hope for discovering new physical phenomena and gaining new insights to existing observations and physical questions.

Tests have already been conducted of Einstein’s theory of general relativity in the extreme regimes of colliding black holes [Abb19b, Abb21d] and properties of the population of compact objects in the universe have been inferred [Abb19a, Abb21c] using the detections of gravitational waves. Furthermore, independent measurements of the Hubble parameter have been conducted by utilising gravitational wave sources as cosmological standard sirens [Abb17, Abb21a, SS19]. In the future with the next generation of detectors, further findings about compact objects are expected. In particular, the equation of state of neutron stars, their maximum mass and other physical properties are of interest. In addition, coalescences of black holes in the early universe or with higher masses are hoped to be observed. It could be possible to study other sources of gravitational waves as well, such as core collapse supernovae or the theoretically posited stochastic gravitational wave background produced in the early universe [Abe11a, Rei19].

2.2 Functionality of Gravitational Waves Detectors

The basic principle of modern gravitational wave detectors (GWDs) is that of a Michelson interferometer, shown in figure 2.1. A laser beam is divided into two partial beams by a 50/50 beam splitter (BS). After travelling an approximately equal distance, each partial beam is reflected by a mirror. Afterwards, the laser beams recombine and interfere with each other at the same beam splitter. The nature of the interference depends on the difference in optical path length that each laser beam has travelled and therefore on the length of the interferometer arms. By monitoring the power of the laser beam in the output port,

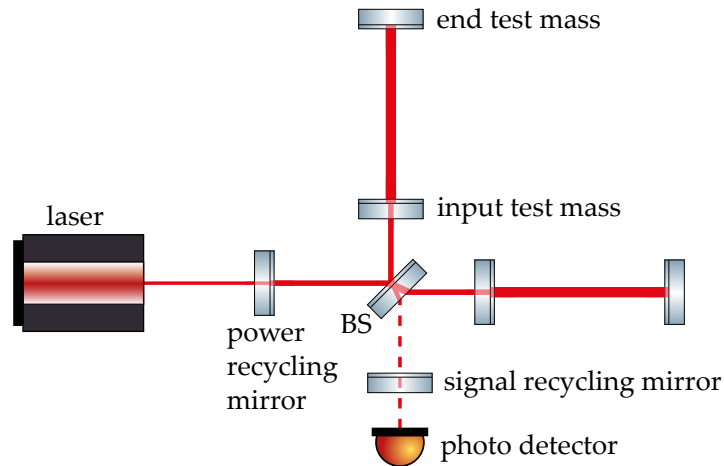


FIGURE 2.2: Schematic depiction of a modified Michelson interferometer used in GWs.

the difference in arm lengths can be continuously measured with high precision. A gravitational wave in the right orientation would periodically change the arm lengths and can in principle be observed by such an instrument if its precision is sufficient.

The challenge consists of building an interferometer with the required sensitivity. In order to achieve this, the basic design needs to be modified and applied with utmost precision. The configuration of a modern GWD interferometer can be seen in figure 2.2. The longer its arms are, the smaller is the detectable strain caused by a passing gravitational wave since the constant relative length change amounts to a higher absolute difference over the complete length of the interferometer arms. A higher total power in the interferometer arms leads to a larger change in power during an arm length jitter caused by gravitational waves. Therefore, arm cavities are introduced. The mirrors close to the beam splitter are also called the input test masses, while those at the ends of the arms are known as the end test masses. In addition, a so called power recycling mirror is placed at the input port of the interferometer. These additional interferometer mirrors usually enhance the circulating power by more than a thousandfold [Abb16a, Som12]. The cavities also ‘virtually’ lengthen the interferometer arms by storing the light for many round trips. Next, a signal recycling mirror is placed at the output port. It fulfils the same function as the power recycling mirror but it enhances the possible signal instead of the base power. The interferometer is operated near the dark port configuration, meaning that its arm lengths are aligned, so that the two parts of the laser interfere mostly destructively in the output port and almost all power is reflected back to the laser. To reduce the coupling of outside vibrations to the measurement, all main optics, especially the arm cavity mirrors, are suspended on multiple pendulum stages inside a vacuum. In addition, active vibration isolation systems are used.

An integral property of gravitational waves, like all waves, is their frequency. To determine different components of the photodetector signal and therefore their physical sources, the signal is analysed in the frequency domain, resulting in a frequency spectrum

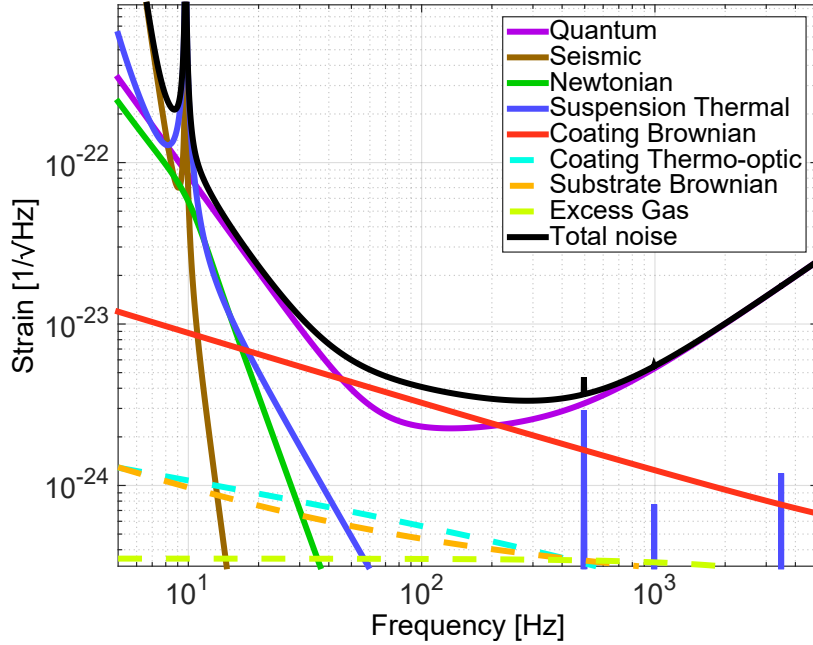


FIGURE 2.3: Simulated design sensitivity curve of the Advanced LIGO GWs, broken down by noise type. Figure was taken from [Bar18].

with a frequency dependent power spectral density [Rau07]. The unit of measurement is m^2/Hz . However, as usually the amplitude of gravitational waves is of interest instead of their power, the square root of the power spectral density is calculated and then normalized to the detector arm length. The result is a spectral strain measurement in $\text{Hz}^{-1/2}$, which is also used to describe the frequency dependent sensitivity of GWs.

2.3 Noise Sources

The sensitivity of a GWD is limited by multiple noise sources. Each noise source is caused by and classified after distinct physical phenomena that cause fluctuating measurements of the interferometer output power by the photodetector. In the following, I give a brief description of the most prominent noise sources, their cause and, if applicable, how in principle to reduce them. As an example, an overview of the noise sources in the Advanced LIGO detectors is shown in figure 2.3. The reduction of mirror coating Brownian noise using amorphous and crystalline silicon is the main topic of this thesis. It is one of the two prevailing noise sources around the most sensitive frequency range near 100 Hz. Highly reflective mirrors for GWs in general and their coating Brownian noise are discussed in detail in chapter 3.

2.3.1 Quantum Fluctuations

The quantized nature of light itself leads to a Poissonian distribution of the photon numbers during an interaction of matter with a mode of light. The standard deviation for a mode with a high average photon number n_{photon} matches that of a Gaussian distribution and is equal to $\sqrt{n_{\text{photon}}}$. This phenomenon has two effects on the noise of GWs. First,

the fluctuating photon number directly causes an equal fluctuation of power on the photodetector. Second, the photons reflecting at the interferometer mirrors each transfer a small amount of momentum to the mirror causing it to vibrate. The former effect is called shot noise while the latter is referred to as radiation pressure noise. The strength of both noises depends on the laser power and measurement frequency. At low frequencies the radiation pressure noise is the predominant source while at higher frequencies the shot noise prevails.

The impact of the radiation pressure noise can be reduced by an increase in mass of the main mirrors due to their growth in inertia. While an increase in power leads to a lower shot noise, since the relative fluctuation is reduced with $1/\sqrt{n_{\text{photon}}}$, the radiation pressure noise is increased by the higher fluctuating photon number with $\sqrt{n_{\text{photon}}}$. Also, the point where the predominant source changes is shifted to a higher frequency. The minimum noise that can be reached for a system at any given frequency with any light power is known as the standard quantum limit. It cannot be undercut by classical approaches. However, in GWDs it is possible to reach a noise level below the standard quantum limit with the application of nonclassical squeezed states of light, injected into the dark port of the interferometer. A thorough description and analysis of the topic of quantum fluctuations and squeezed states of light in GWDs can be found in [Sch17].

2.3.2 Seismic Vibrations

The Earth itself is not a rigid, unmoving object. There are constantly smaller and bigger movements and shifts in its crust and on its surface like earthquakes, ocean waves, weather patterns and human activity which create propagating seismic waves. These can cause the optics of GWDs to vibrate [Bad21]. The strength of the different seismic vibrations depends on the environment and soil material near the GWD. The total noise from seismic vibrations is therefore highly location dependent and quiet environments are preferable. Even when environmental factors are taken into consideration, the strength of the vibrations still has to be greatly reduced for the noise to reach an acceptable level. This is achieved by the utilisation of active and passive isolation systems for the main interferometer optics. In Advanced LIGO for example, the active systems consist of several vibration sensors and permanent magnet actuators. Attached to the active isolation is the passive system with four pendulum stages, each one reducing the coupling of noise even further [Ast12, Mat15].

2.3.3 Newtonian Gravity

GWDs are influenced by noise from a fluctuating gravitational field caused by changing densities in the environment of the interferometer. This phenomenon is called Newtonian gravity noise or simply Newtonian noise. The biggest contributions in the relevant frequency range are seismic displacements, varying atmospheric densities and movements of nearby objects like vehicles. These sources are highly location dependent and as such

quiet sites are preferable for GWDs. It is not possible to directly isolate objects from gravitational fields. However, as it is mostly caused by seismic surface waves and activity on the surface and in the atmosphere, it is possible to reduce the impact of Newtonian noise by building GWDs underground [Bek12].

2.3.4 Residual Gas

The main optics of modern GWDs are placed inside vacuum chambers, that have been evacuated to pressures below 10^{-8} mbar. However, the vacuum still contains some residual gas. These atoms and molecules move randomly inside the vacuum chambers and collide with the interferometer optics. The impacts transfer a small amount of momentum each time, which slightly shakes the optics and causes them to vibrate. In addition, the residual gas in the arm cavities can alter the phase of the light during transit as well as scatter light which occasionally is coupled back into the interferometer. All three phenomena ultimately affect the amount of detected light in the output port resulting in noise. The extent of the noise is directly influenced by the amount of residual gas and thus can be reduced by lowering the pressure inside the vacuum chambers of the GWDs [Mar16].

2.3.5 Suspension Thermal Noise

The suspensions which hold the interferometer optics themselves typically have several normal modes at frequencies inside the observed spectrum during operation of the GWD. These modes are thermally excited, which means that the random movement of the suspension material itself causes the excitement. The mechanism behind that phenomenon is described by the fluctuation-dissipation theorem [Kub66]. The excited modes cause the optics to move which is translated into power fluctuations in the output port.

The biggest noise contributions are near the normal mode frequencies. In-between them a much lower noise floor is situated. The mode frequencies are mainly in two different regimes [Gon00, Ast12]. The first order pendulum modes are typically around the 1 Hz regime and their harmonics are located at higher frequencies correspondingly. The frequencies of the violin and bouncing modes range from a few hundred hertz up to several thousand. The suspension thermal noise can be reduced by cooling down the optics and suspensions to lessen the random material movements. The noise floor can also be lowered by higher Q factors of the modes which however in return enhance the mode peaks. Though, the Q factor of a given suspension is usually temperature dependent and it could be negatively affected by cooling, possibly resulting in a slight offset of the noise reduction. Finally, by adjusting the normal mode frequencies, their impact on the gravitational wave measurements can be decreased.

2.3.6 Mirror Coating Brownian Noise

The interferometer mirrors and their coatings operate at a non-zero temperature and thus the coating atoms experience a random movement restricted only by the properties of

the solid material. For that reason, the mirror surfaces fluctuate randomly in their position by a small amount. Although strictly speaking the fluctuations cannot be classified as Brownian motion, since the atoms are not freely suspended in a medium, this noise is still called mirror coating Brownian noise or simply thermal noise. The coatings behave like mechanical oscillators and the noise is consequently affected by their material properties, in particular their mechanical loss. Therefore, it is necessary to choose materials with not only suitable optical but also mechanical properties. A reduction of the random movement by lowering the temperature or using coating materials with better mechanical quality can reduce the thermal noise. However, a change in temperature also affects many material properties which could have a negative influence to the noise level. Coating thermal noise is discussed in detail in section 3.3.

2.3.7 Mirror Coating Thermo-Optic Noise

The local temperature of different points of the main optics is constantly fluctuating due to thermal dissipation in the material. The mirror coatings are usually made of materials that have a temperature dependent refractive index ($dn/dT \neq 0$). Thus, the reflectivity of the mirror depends likewise on the temperature and as the coatings experience the aforementioned temperature fluctuations, the reflectivity and transmission also fluctuate. In addition, the thermal expansion of the coating leads to a varying position of the optics surfaces and changes the coating thickness, which in turn influences the reflectivity even more [Eva08]. As for other thermal noises, the thermo-optic noise can be reduced by cooling the optics to a lower temperature. In addition, materials with a small dn/dT and low thermal expansion coefficient at the operation temperature of the GWD can help to lower the noise.

2.3.8 Mirror Substrate Brownian Noise

The substrate Brownian noise is very similar to the coating Brownian noise as it is caused and influenced by the same mechanisms. Random movements of the atoms in the substrate materials cause position fluctuations of the optics. Its strength is determined by the optic's temperature and mechanical loss. Their reduction would directly lead to a lower substrate Brownian noise.

2.4 Current Detectors

There are currently five GWDs worldwide in operation: two aLIGO detectors in Hanford, USA and Livingston, USA, the AdvVirgo detector in Pisa, Italy, the KAGRA detector in Hida, Japan, as well as the GEO600 detector near Hannover, Germany. As of today, the former three detected in their first three observing runs a total of 90 gravitational wave signals [Abb21b], while the latter two detectors have not been able to detect any signals, yet [Abb22].

There are a lot of similarities in the setups of the current detectors. The interferometer arm lengths range from a folded 600 m (GEO600, effectively 1.2 km) through 3 km (AdvVirgo, KAGRA) to 4 km (aLIGO). All detectors operate at a laser wavelength of 1064 nm. They utilise large fused silica substrates held at room temperature with the exception of KAGRA, which operates at 20 K with sapphire substrates. The substrate diameters range from 18 cm in GEO600, through 20 cm in KAGRA up to 34 cm and 35 cm for the aLIGO and AdvVirgo detectors respectively. GEO600 is the only detector which does not have arm cavities and instead uses only its power recycling mirror for the power build up. KAGRA on the other hand is the only detector constructed underground. The main optics of all detectors are coated with multiple bilayers of the same materials, namely silica (SiO_2) and tantala (Ta_2O_5). However, the aLIGO and AdvVirgo detectors use a titania (TiO_2) doping in their respective tantala layers to reduce coating thermal noise, while KAGRA and GEO600 use pure tantala [Abb16a, Ace14, Aff14, Aso13, Hei14, Som12].

The sensitivities of the current GWDs have steadily been improved over the past years. In LIGO's third observation run, a total strain noise as low as $5 \times 10^{-24} \text{ Hz}^{-1/2}$ had been reached at the most sensitive frequencies at around 200 Hz. In the range from approximately 40 Hz to 1.3 kHz the noise of the Livingston detector was almost consistently below $10^{-23} \text{ Hz}^{-1/2}$. The Hanford detector, on the other hand, only achieved values below this threshold from about 50 Hz to 850 Hz. AdvVirgo has reached a minimum strain noise of about $10^{-23} \text{ Hz}^{-1/2}$ around 100 Hz with a spectrum of roughly 55 Hz to 450 Hz below $2 \times 10^{-23} \text{ Hz}^{-1/2}$. The KAGRA and GEO600 detectors were less sensitive with a total noise level of about $4 \times 10^{-23} \text{ Hz}^{-1/2}$ and $1.4 \times 10^{-22} \text{ Hz}^{-1/2}$ at each minimum respectively [Abb20, Lou21]. Despite the already impressive sensitivities of the current GWDs, a further increase in coming observing runs is expected due to various ongoing research activities.

2.5 Future Detectors

There are several proposals for so called third generation GWDs that will have reduced noise compared to current detectors, possibly combined with an expanded frequency range or with operation in completely different frequency regimes. In the sub-hertz frequency regime below the current detection band, space-based antennas like LISA [AS17] and DECIGO [Sat17] have been conceived. New ground-based facilities like the Einstein Telescope (ET) [Abe11a] and Cosmic Explorer (CE) [Hal21, Rei19] are proposed mainly for improvements in a similar frequency regime as current ground-based detectors and slightly below. In addition, some proposals utilize existing sites by performing extensive upgrades to operating GWDs, for example LIGO Voyager [Adh20].

The future ground-based detectors are planned to reduce many noise types in order to reach their sensitivity goals of a minimum strain noise well below $10^{-24} \text{ Hz}^{-1/2}$ while being sensitive over a much wider frequency range. To achieve that, extensive changes and developments in all detector areas are needed. Most notable are increased arm lengths of

10 km (ET) and 40 km (CE) combined with the division of some detectors in interferometers operating at room temperature or at cryogenic temperatures. For ET, a total of six interlaced interferometers are planned to be operated at the same time with three interferometers being run at room temperature while the other three are cooled to cryogenic temperatures. This design is implemented to allow ET to detect gravitational waves in different frequency regimes: the cryogenic interferometers for lower frequencies and the room temperature interferometers for higher frequencies. CE has a more classical approach of utilising only one interferometer, which is planned to operate at first at room temperature and is later cooled to cryogenic temperatures.

For the room temperature interferometers, mainly the currently used technology is improved and planned to be used. The main optics made of fused silica are projected to grow significantly in size with test masses of about 200 kg (ET) and 320 kg (CE) and diameters of about 62 cm (ET) and 70 cm (CE) compared to the currently largest size of 42 cm and 35 cm in AdvVirgo. The laser wavelength will be kept at 1064 nm, but the circulating light powers in the arm cavities are planned to be increased to 3 MW (ET) and 1.4 MW (CE).

The temperatures contemplated for cryogenic interferometers range from 10 K to 123 K. At these temperatures, fused silica is no longer well suited as a substrate material for the main optics due to its mechanical loss. Therefore, new materials are being investigated with crystalline silicon being the most promising candidate. Test masses of large sizes are planned to be used with weights of about 211 kg (ET) as well as 320 kg (CE) and diameters of at least 45 cm (ET) and 80 cm (CE). The operating laser wavelength needs to be increased as silicon is not transparent at 1064 nm. Wavelengths of 1550 nm or about 2000 nm are currently being investigated regarding their implementation in GWDs.

New optical coatings are required to reach the sensitivity goals of future detectors. The coatings are already partly limiting the sensitivity of current room temperature GWDs, but improvements are required especially for future cryogenic interferometers. The reason is the mechanical loss of the current coatings which increases significantly at low temperatures and therefore counteracts the reduction of thermal noise from the reduced temperature [Har06, Mar08, Mar10, Mar14, Ste18a]. There are several materials considered for cryogenic low noise optical coatings. In this thesis work, my focus was on amorphous and crystalline silicon as coating materials for GWD mirror designs. In the next chapter GWD mirrors, and challenges associated with improving them, are discussed in more detail. Along with this, an overview of many candidate coating materials for future detector mirrors is presented.

Chapter 3

Test Mass Mirrors for Gravitational Wave Detectors

3.1 Highly Reflective Mirrors

In practically all advanced optical experiments, highly reflective (HR) mirrors are required, especially for those involving lasers or other narrow bandwidth light sources. They are essential for the manipulation of light, from a simple redirection, over a focussing or defocussing function up to advanced techniques like dispersion control using chirped mirrors [Kä97]. While their reflectivity can extend into a more broadband domain, HR mirrors are usually designed for only one or a few narrow wavelength regions. At design wavelengths it is possible for the reflectivity to exceed 99.999 % [Che02].

The physical principle of a typical HR mirror is that of a dielectric or Bragg mirror. Multiple layers of materials with a high and low refractive index n are deposited in alternation on a substrate. At each transition between different media the incident light is partly reflected and partly transmitted. Snell's law describes the relation between the incident angle α and the refracted angle β of the transmitted light [Dem09]:

$$\frac{\sin \alpha}{\sin \beta} = \frac{n_1}{n_2}. \quad (3.1)$$

Here, n_1 is the refractive index of the first medium in which the light originated from and n_2 is the second medium the light transits into. The light power is divided into the reflected and transmitted part in accordance to the Fresnel equations [Dem09]. For materials with a relative magnetic permeability μ_r close to 1, which is usually the case in optical applications, the power reflection coefficients for perpendicular polarized light R_s (German *senkrecht*) and parallel polarized light R_p are

$$R_s = \left(\frac{n_1 \cos \alpha - n_2 \cos \beta}{n_1 \cos \alpha + n_2 \cos \beta} \right)^2 = \left(\frac{\sin(\alpha - \beta)}{\sin(\alpha + \beta)} \right)^2, \quad (3.2)$$

$$R_p = \left(\frac{n_1 \cos \alpha - n_2 \cos \beta}{n_1 \cos \alpha + n_2 \cos \beta} \right)^2 = \left(\frac{\tan(\alpha - \beta)}{\tan(\alpha + \beta)} \right)^2. \quad (3.3)$$

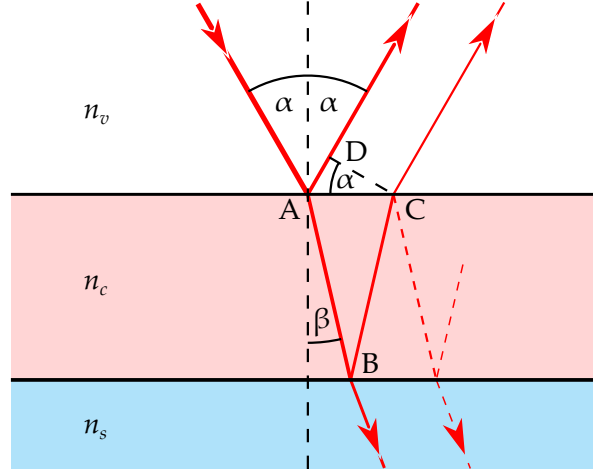


FIGURE 3.1: Schematic depiction of light reflected from a single layer coating on a substrate. At the transition between different media, light is reflected and refracted depending on the refractive indices n_v , n_c and n_s as described by the Fresnel equations and Snell's law. Here, $n_v < n_s < n_c$.

Both Snell's law and the Fresnel equations can directly be derived from the electro-magnetic wave equation in conjunction with their boundary conditions [Dem09]. As required by the conservation of energy, the power transmission coefficients T_s and T_p are simply the part of the light that is not reflected:

$$T_s = 1 - R_s, \quad (3.4)$$

$$T_p = 1 - R_p. \quad (3.5)$$

Please note that there is no absorption directly at the boundary, but only during the transmission through the material. The effects of optical absorption on mirrors and GWDs will be discussed in section 3.2. For now it is assumed to be absent. In addition, scattering effects could effectively reduce all coefficients. However, for the high precision optics of GWDs, the scattering is very low. Averaged over the central part of the aLIGO main cavity mirrors, it is in the range of a few ppm with the majority taking place at distinct scattering points [Pin17]. Its influence on the power reflection and transmission coefficients at a single media transition can therefore be neglected. The incident angle for the test masses of the GWDs is $\alpha = 0$. It follows, that there is no longer any distinction between different polarisations. As a result, equations 3.2 to 3.5 are simplified to polarisation independent coefficients R_i and T_i :

$$R_i = \left(\frac{n_1 - n_2}{n_1 + n_2} \right)^2, \quad (3.6)$$

$$T_i = 1 - R_i. \quad (3.7)$$

The above described phenomenon of reflection, transmission and refraction occurs at every transition inside an HR coating. For simplification, let's consider a single thin layer

with a refractive index of n_c on a substrate with n_s inside a vacuum with $n_v = 1$ as displayed in figure 3.1. Initially, the irradiating light is partly reflected. After the transmission at the surface, the remaining light encounters the second media change between the coating and the substrate. Here, it is again partly transmitted and reflected. The now reflected part travels back to the surface and eventually into the vacuum again. This process of continuing reflection and transmission repeats itself till the light power is depleted. Since the layer thicknesses of optical coatings are very thin in comparison to the diameter of a reflected light beam, the different reflected parts from the coating overlap and interfere with each other. The nature of the interference depends on the phase relation of the different reflections, which in turn depend on the optical path length difference Δs :

$$\Delta s = n_c(\overline{AC} + \overline{BC}) - n_v \times \overline{AD} \quad (3.8)$$

with

$$\overline{AB} = \overline{BC} = \frac{d_l}{\cos \beta'} \quad (3.9)$$

$$\overline{AC} = 2d_l \tan \beta, \quad (3.10)$$

$$\overline{AD} = \overline{AC} \times \sin \alpha. \quad (3.11)$$

Here, d_l is the thickness of the coating layer. Using Snell's law (Equation 3.1) one finds

$$\Delta s = 2d_l n_c \cos \beta. \quad (3.12)$$

A phase change can also occur at each reflection or transmission. There are multiple valid mathematical interpretations of the phase relations [Lou03]. The most common one is that the light reflected at an optical denser medium undergoes a phase change of $\pi = 180^\circ$. If we assume $n_c > n_s$ on the considered coating, it means, that the phase flip occurs only at point A. The reflectivity of the coating is maximized for light of the wavelength λ if constructive interference between the reflected parts occur and the transmitted parts interfere destructively. Taking the phase flip into account, it follows for the coating thickness

$$d_{l,\text{HR}} = \frac{(m + 1/2) \lambda}{2n_c \cos \beta}, m \in \mathbb{N}. \quad (3.13)$$

For reasons described at the end of this section, it is beneficial for the coating to be as thin as possible, meaning $m = 0$. Applying $\beta = 0$ for the case of GWDs, equation 3.13 is simplified to

$$d_{l,\text{HR}} = \frac{\lambda}{4n_c}. \quad (3.14)$$

A coating layer with such a thickness is commonly known as a quarter wave layer.

For a mirror to reach a high reflectivity, multiple quarter wave layers with different refractive indices need to be stacked. The usual practice is to stack alternating layers of two

materials, one with a high refractive index and one with a low refractive index, starting and ending with the high refractive index material. A pair of these layers with different refractive indices are generally called a bilayer. Novel designs however suggest the usage of a third or even more materials for the coatings of GWD test masses (see section 3.4). By adjusting the number of bilayers in combination with the possibility to slightly vary some of the layer thicknesses, it is theoretically possible to tune the reflectivity of an HR coating to any value. In reality, the limit is determined by optical losses due to absorption and scattering.

The total thickness of a potential coating is an important characteristic to consider for its implementation in GWDs as test mass coatings should generally be kept as thin as possible. A thin coating not only lowers the time and costs for the manufacturing, it also improves on the optical absorption and reduces the coating thermal noise as described in sections 3.2 and 3.3 respectively. There are two factors that determine the coating thickness for a given reflectivity. Firstly, it can be directly deduced from equation 3.14 that the higher the refractive index of a material is, the thinner a quarter wave layer of said material becomes. Secondly, the reflectivity of a given bilayer depends on the difference between the refractive indices of the involved materials as described by equation 3.6: the higher the difference, the greater is also the reflectivity. It follows that a reduced number of bilayers is needed for a high difference in indices compared to a low difference resulting in a thinner coating. It should be noted that the latter factor has a greater influence on the total thickness than the former, meaning that it is beneficial for a material complementing a given high refractive index material to have a relatively low refractive index although it means that its quarter wave layer thickness increases as a consequence.

3.2 Optical Absorption

The absorption of light in matter is a fundamental physical phenomenon and generally occurs in all optics. Its strength can differ vastly over many orders of magnitude, ranging from sub ppm levels to nearly 100% per component. Optical absorption is wavelength dependent and arises during the transmission of light through a material and is therefore material specific. Generally, there is absorption in the bulk material, but it can also occur at impurities or point defects that then form point absorbers.

There are different ways of quantifying optical absorption. The most common and intuitive way is simply stating the amount of absorption as a fraction of the input power incident on the given optical component. However, as the absorption is directly affected by the length of transmitted material as well as changes of the electric field intensity inside the component due to interferences, simply stating the absorption is not suitable for the comparison of materials considered for coatings or substrates. Therefore, a length normalized expression for a single pass of light through the material without interference effects is generally adopted. For bulk absorption in substrates, it is often stated in units of $1/\text{cm}$. For coatings, the aforementioned unit is unpractical to use, as the coating thickness

is usually in the region of micrometres. A suitable possibility to display the absorption for coatings is the extinction coefficient k , the imaginary part of the complex refractive index $\mathbf{n} = n + ik$. Throughout this thesis, I refer to the real part n of the complex refractive index simply as the refractive index. The effect of the extinction coefficient can be seen by describing the electric field E_w of an electromagnetic wave with the complex wave equation [Dem09]

$$E_w = E_{w,0} \exp \left(i \left(2\pi \frac{z}{\lambda} n - \omega t \right) \right), \quad (3.15)$$

where $E_{w,0}$ is the initial electric field amplitude, z is the position along the z axis, the direction in which the electromagnetic wave is propagating, λ is the wavelength, ω is the angular frequency and t is the time. By inserting the complex refractive index in equation 3.15, the wave equation can be separated into two parts, the oscillation of the electric field over time and space and its attenuation.

$$E_w = E_{w,0} \exp \left(i \left(2\pi \frac{z}{\lambda} n - \omega t \right) \right) \exp \left(-2\pi \frac{z}{\lambda} k \right) \quad (3.16)$$

Thereby, k determines the strength of the optical absorption during a material transmission, normalized to the thickness in relation to the considered wavelength of the light. It is proportional to the absolute value for small absorptions. As an example, calculating k for a component with 1% absorption by assuming the prior mentioned proportionality would amount to a maximum systematic relative error of only 0.5%, with an ever decreasing error at lower absorption levels.

The optics of current GWDs are extraordinary in regards to their absorption. It is generally attempted to keep the absorption as low as possible. As a reference, for the coatings of the input and end test masses of aLIGO, total values of about 0.22 ppm and 0.27 ppm respectively were achieved [Pin17]. A very low absorption in GWDs is necessary for several reasons explained in the following paragraphs.

Absorption mostly occurs in the coatings and is also not uniformly distributed there due to the Gaussian beam shape and existing point absorbers [Pin17]. Every instance of absorption of light power increases the local temperature of the optic after which the heat is conducted through the body of the optic and to its surrounding environment. As the conduction is not instantaneous but limited in its speed, the optics temperature during operation of the GWD is not uniform, which leads to two effects. Firstly, a deformation of the optic by thermal expansion occurs, resulting in changing radii of curvature and therefore focal lengths. Secondly, the temperature dependent refractive index of the coating materials alters the local reflectivity of the mirror. Both effects can lead to beam distortions or the formation of thermal lenses. Such a dealignment of the high precision interferometer setup might disturb the measurements of the detector, depending on the strength of the described phenomena.

The unequal heating can in part be countered by the so called thermal compensation systems of modern GWDs [Aie19, Bro16]. They work by deliberately heating the parts

of the interferometer optics that are less affected by the main laser beam to reduce the induced temperature gradient. However, this will introduce additional heating to the optics. For cryogenic detectors, the absorption and its compensation systems present a problem to the cooling of the optics. Its severity depends on the total amount of energy introduced as the cooling power of the optics are severely limited by the low amount of thermal radiation and heat conducted through the suspension fibres [Cum13, Sha17]. Lastly, optical absorption is a type of optical loss, which should generally be avoided as it affects the circulating light power inside the interferometer.

The measurements of optical absorption presented in this thesis were all carried out by photothermal common-path interferometry (PCI). PCI uses a pump-probe technique to compare the absorption of a sample to a calibration piece with known absorption. The exact working principle and the setup at the University of Hamburg is described in detail in chapter 4.

3.3 Coating Thermal Noise

One of the fundamental noise types in a GWD is mirror coating thermal noise or Brownian noise (see section 2.3). It is caused by random movements of the atoms inside the coating resulting in an effectively fluctuating mirror surface position. Thermal noise is one of the prevailing noise sources in current ground based gravitational wave detectors in their most sensitive frequency regime [Ace14, Aso13, Gro10, Hei14, Bar18].

In principle, an interferometer mirror behaves like a mechanical oscillator. That means, mechanical eigenmodes are excited by the random Brownian-like movements of atoms as described by the fluctuation-dissipation theorem [Kub66]. The strength of the movement not only at the eigenmode frequencies but also at frequencies below and above them is determined by the portion of energy stored in each mode and the total energy in the system, meaning its temperature. The amount of energy in each mode depends on the mechanical properties of the coating and substrate materials, namely their mechanical losses, Young's moduli and Poisson's ratios as well as on the geometries of the sample. In this context, the mechanical loss is usually given by the mechanical loss angle ϕ defined as [Sau90]

$$\phi = \frac{1}{Q}, \quad (3.17)$$

where Q is the quality factor of the oscillator.

Let's consider a Gaussian laser beam on a mirror at an incident angle of $\alpha = 0$. The width of the beam is described by the beam radius w where the intensity drops to $1/e^2$ of its maximum. The combined coating and substrate thermal noise power spectral density S_x

is then given by [Har12]

$$S_x = \frac{2k_B T(1 - \sigma_s^2)}{\sqrt{\pi^3} f \omega Y_s} \left(\phi_s(T, f) + \frac{d_c}{\sqrt{\pi} \omega} A \phi_c(T, f) \right), \quad (3.18)$$

where

$$A = \frac{Y_c^2(1 + \sigma_s)^2(1 - 2\sigma_s)^2 + Y_s^2(1 + \sigma_c)^2(1 - 2\sigma_c)}{Y_s Y_c (1 - \sigma_c^2)(1 - \sigma_s^2)}. \quad (3.19)$$

Here, k_B is the Boltzmann constant, T is the temperature of the system, d_c is the coating thickness, f is the considered frequency for the evaluated spectral density, σ_s and σ_c are the Poisson's ratios of the substrate and coating respectively, Y_s and Y_c are their Young's moduli and $\phi_s(T, f)$ along with $\phi_c(T, f)$ are their temperature and frequency dependent mechanical loss angles. To give a rough estimate of the power spectral density, an often used simplification is to omit the influence of the Poisson's ratios by setting both to 0. Furthermore, the remaining term in parenthesis in equation 3.18 is often separated into two expressions for the coating and substrate thermal noise power spectral densities, resulting in

$$S_{x,c} \approx \frac{2k_B T d_c}{\pi^2 f \omega^2 Y_s} \phi_c(T, f) \left(\frac{Y_c}{Y_s} + \frac{Y_s}{Y_c} \right), \quad (3.20)$$

$$S_{x,s} \approx \frac{2k_B T}{\sqrt{\pi^3} f \omega Y_s} \phi_s(T, f). \quad (3.21)$$

Please note that in the expression for the coating thermal noise $S_{x,c}$ the Young's modulus for the substrate Y_s still remains, making a complete separation from the substrate properties impossible. Of all mechanical properties the mechanical loss has the greatest influence on the coating thermal noise as the loss takes on the by far the widest range of values while the thermal noise power is directly proportional to it.

Since HR coatings consist of multiple materials, their effective mechanical losses, Young's moduli and Poisson's ratios can be treated as a mixture of the values of the pure materials used. The Young's moduli for composite coatings of m materials is specified by the standard rule of mixture [Jon75]:

$$Y_c = \sum_m r_m Y_m. \quad (3.22)$$

Here, r_m is the thickness ratio of the m -th material with $\sum_m r_m = 1$. The mechanical loss for composite coatings, assuming it is independent of the layer thicknesses and there is no additional loss introduced at the layer interfaces, can be estimated as [Jon75]

$$\phi_c = \sum_m r_m \frac{Y_m \phi_m}{Y_c}. \quad (3.23)$$

The composite Poisson's ratio cannot be easily determined from the unmixed values of the initial materials. There is no analytic expression for the general case as it can only be

determined by numerical methods. Only in the binary case can a complex expression be found, which depends on the mixing ratio of both materials, their Poisson's ratios and Young's moduli [Bar94].

It can be easily seen from equation 3.20, that for a low level of coating thermal noise in GWDs an operation at low temperatures is beneficial. Cooling the GWD test masses from room temperature to, for example, 20 K could in theory yield an improvement of a factor of $\sqrt{293/20} \approx 4$ in strain sensitivity, which is proportional to the square root of the power spectral density (see section 2.2). In reality, the temperature dependent mechanical loss could lessen the expected reduction in thermal noise, depending on the material. Considering the silica-tantala coatings currently used in aLIGO and AdvVirgo, the thermal noise would only be reduced by about a factor of 2 due to an increase in losses [Ste18a].

An increase of the laser beam radius also lowers the thermal noise as shown by equation 3.20. However, the beam size is limited by the size of the interferometer test masses and other optics. A change in size would require major rework of current facilities. Future detectors are already planned with bigger optics in mind to account for this (see section 2.5). Using the same materials, modifying the coating thickness would also alter the reflectivity of the optics. Any sensitivity gain caused by a lower thickness would vanish by the influence of the reduced circulating light power. Only a change of refractive indices and therefore different materials could lower the thickness while maintaining the required reflectivity. Similarly, the mechanical properties namely loss, Young's moduli and Poisson's ratios only depend on the materials used. However, the influence on the thermal noise is generally not equally distributed on the used materials, some layers contribute more than others. By modifying the thickness of the coating layers with the goal to minimise the share of the stronger contributing parts, meaning effectively deviating from the ordinary quarter wave layers, it is possible to lessen the mechanical loss of the coating. Although, more bilayers are required for an identical reflectivity raising the total coating thickness, a slight reduction of the total thermal noise can be achieved [Agr06, Vil10]. Apart from that, additional improvement require new appropriate materials or at least modified ones. To conclude, any major advancements in terms of coating thermal noise require utilizing different coating materials than those currently used in GWDs.

3.4 Multi-Material Coatings

The reduction of coating thermal noise in modern GWDs proves to be a challenging undertaking. Numerous materials demonstrate to have a much lower mechanical loss than the currently used silica-tantala coatings, both at room temperature and at cryogenic temperatures. However, their other properties prevent a direct implementation in a classic two-material HR coating. The reasons for that are diverse, but the materials in question often display an optical absorption exceeding the tolerable levels of future detectors. Therefore, the challenge consists of producing novel coatings with a significantly

reduced thermal noise while at the same time maintaining a sufficiently low total absorption. Multi-material coating designs make it possible to utilize relatively high absorbent materials while circumventing the increase in absorption that would be present in conventional HR coatings [Ste15, Yam15].

The working principle of a multi-material approach is to implement various materials at different depths in the coating. At the top, where the mean intensity of the electromagnetic light field is the highest, the coating layers consists of low and high refractive index materials which have the lowest optical absorption but an elevated mechanical loss. The upper layers reflect part of the light and therefore lowers its intensity in the following layers. Once the field intensity decreases enough other materials with higher absorption can be used. While the total absorption still slightly increases, the contribution of the bottom layers are lowered by the factor by which the light intensity is decreased inside the coating by the top layers. The contributions to the mechanical loss on the other hand are independent of the light intensity. They are equally distributed according to each material's thickness ratio and Young's modulus as described by equation 3.23. There is however a weighting factor which alters each layers contribution to the total thermal noise based on the fluctuations in the round-trip phase the light experiences in the respective coating layers [Hon13, Kon11, Yam15]. These fluctuations are proportional to the peak light intensity in the layers and ultimately lead to a slightly higher weighting of the coating layers positioned near the substrate compared to the ones close to the surface. As a result, high absorbent low mechanical loss materials in the bottom layers can significantly improve on the total coating thermal noise while having a limited addition to the optical absorption.

The possible employment of multi-material coatings opens up a pallet of new materials that can now be utilized in GWDs. The exact depth where the switch to low loss bilayers occurs depends on the amount of total absorption that is still tolerable. This means, the lower the absorption of a given material, the earlier it can be implemented. In conclusion, multi-material coating designs offer a trade off between a thermal noise reduction and an increase in optical absorption.

3.5 Coating Materials

Current GWDs are partly limited by the coating thermal noise of their main optics and any significant reduction requires the implementation of new materials and coating designs. There are several different materials considered for both the low and high refractive index coating layers of future GWD test masses. The candidates are mainly amorphous oxides, but also other amorphous or crystalline materials are being researched. The exact properties of a deposited coating layer are not only determined by the material itself, but in general they are also heavily influenced by the deposition parameters like the growth rate and temperature, especially for amorphous materials as they offer a much wider range in how their atomic structure is organised compared to crystalline materials [Bir18, MR21].

In addition, heat treatment after the coating is deposited can greatly influence the mechanical loss and optical absorption [Abe11b, Mar10, Ste16b, Ste18b]. Therefore, both deposition parameters and heat treatment had to be taken into account when investigating suitable materials for test mass coatings of future GWDs.

In this section, I give a short overview of the materials considered. Their respective advantages and disadvantages are briefly discussed in regards to their utilisation as coatings in the interferometers of future GWDs (see section 2.5). This includes classic room temperature (RT) detectors as well as detectors held at cryogenic temperatures with operating wavelengths from 1064 nm to about 2000 nm. The most promising candidate materials are

- silicon dioxide (SiO_2),
- tantalum pentoxide (Ta_2O_5),
- aluminium trioxide (Al_2O_3),
- hafnium dioxide (HfO_2),
- a mixture of titanium dioxide and germanium dioxide ($\text{TiO}_2\text{-GeO}_2$),
- amorphous silicon (aSi),
- silicon nitride (SiN_xH_y),
- aluminium gallium arsenide (AlGaAs).

3.5.1 Silicon Dioxide

Depending on its purity, SiO_2 (silica) has a very low absorption over a wide spectral range [Gra20a]. This includes the wavelengths used or considered in current or future GWDs, where the refractive index of silica is about 1.44 [Mal65]. The influence of its deposition and post deposition heat treatment is well understood as it is regularly utilized as a material in commercial coatings and makes up the low refractive index layers of all current generation GWDs. It remains the top option for future RT detectors. However, at cryogenic temperatures silica is problematic due to the increase of mechanical loss [Mar14, Rob18]. Even so, it is still a possible choice in the top layers of multi-material designs due to its excellent optical properties. Furthermore, recent research shows an improved loss angle by utilisation of a silica-titania (TiO_2) nano-layer coating stack where each individual layer has a thickness of 3.6 nm and 1.8 nm respectively [Kuo19]. However, such a stack increases the effective refractive index to 1.76 resulting in a thicker HR coating with more layers, thus partly counteracting the lowered thermal noise by the improved mechanical loss. Still, further research might yield silica-titania nano-layers to be indeed viable to be used as the sole low refractive index material in coatings for cryogenic test mass mirrors.

3.5.2 Tantalum Pentoxide

The optical properties of Ta_2O_5 (tantala) are superb as it shows only miniscule absorption and scattering at relevant wavelengths, where the refractive index is about 2.09 [Gao12]. This enables tantala to be used as a high refractive index material in HR mirror coatings. At first, tantala was used in its pure form in test mass coatings for GWDs, but as of today only tantala doped by varying metal oxides is of interest. There are mainly two dopants currently in consideration with different advantages and varying states of their respective research regarding their implementation in GWDs.

Titanium Dioxide doping TiO_2 (titania) is today's most common dopant since titania doped tantala is currently used as the high refractive index material in GWDs. The deposition and heat treatment is therefore well understood. It has a relatively high mechanical loss however [Gra20a], which increases even further at cryogenic temperatures [Mar09]. As a result, it is the main cause of coating thermal noise and a limiting factor for the sensitivity of current GWDs. There were multiple research activities in the past regarding the deposition parameters of titania doped tantala with the goal to lessen the mechanical loss, but a major improvement beyond the current state of the art coatings seems improbable [Rei16]. Still, as a well known material with excellent optical properties, it might be utilized in a few layers at the top of multi-material coatings for future GWDs, even at cryogenic temperatures.

Zirconium Dioxide doping ZrO_2 (zirconia) is also considered as a dopant for tantala in future test mass coatings. The atomic structure of zirconia doped tantala and its influence has been researched. It was found to increase the crystallization temperature of amorphous thin films allowing for higher heat treatment temperatures of up to 800°C instead of a maximum 600°C . This is beneficial for the mechanical loss value and reduces thermal noise compared to titania doped tantala coatings. Simultaneously, the optical absorption remained at a very low level of 0.5 ppm for an HR coating but scattering increased nine-fold [Abe21, Pra19]. However, microscopic argon inclusions could be part of the cause for the increased scattering. This problem is currently under investigation [Cum21] and might be solved in the future. There are also attempts of adding zirconia to already titania doped tantala coatings to raise the heat treatment temperature while still benefiting from the titania dopant [Lal21]. All factors considered, zirconia doped tantala is an interesting candidate material for mirror coatings future detectors.

3.5.3 Aluminium Trioxide

In its bulk form Al_2O_3 (alumina) is often referred to as sapphire or sapphire glass, where it is mostly used in crystalline form. As an amorphous layer, it has suitable optical properties for GWD mirror coatings and show a relatively low mechanical loss. However, the refractive index of alumina is about 1.65 at relevant wavelengths. As such it can not serve as a high refractive index material in an HR coating. The required number of layers

would be significantly more compared to current coatings, drastically increasing the coating thickness and offsetting its potential thermal noise advantage with a lower mechanical loss [Mar12]. As a low refractive index material at RT, alumina is inferior to silica, which has a lower refractive index and mechanical loss [Fla10]. At cryogenic temperatures on the other hand, alumina might come to be a viable option as the thermal noise of silica suffers from an increasing mechanical loss while the loss of alumina slightly decreases [Rob18].

3.5.4 Hafnium Dioxide

The refractive index of HfO_2 (hafnia) is about 1.88 at relevant wavelengths, making it an interesting candidate for GWD mirror coatings as it also offers a relatively low optical absorption. In combination with silica, hafnia could serve as a high refractive index material, or it could be employed in combination with amorphous silicon as a low refractive index material. The mechanical loss is above that of tantala at RT but lower at temperatures below 100 K as it does not show any loss peaks [Abe11b], thus making hafnia based coatings a viable option only for cryogenic detectors. However, its easily crystallising nature is disadvantageous as it allows only for low heat treatment temperatures, possibly negatively affecting other coating materials. In addition, the coating process itself might result in a partly crystallised layer. Although these partly crystallised coatings still show a good mechanical loss value, the increased scattering renders such a coating unusable for GWDs [Abe11b]. Doping hafnia with silica has shown to make the coatings more resilient to crystallisation while maintaining their low mechanical loss. The optical absorption of hafnia is too high for a classic two-material coating to be used in GWDs. Contrarily, multi-material coatings consisting of silica, tantala, hafnia and amorphous silicon are able to meet the strict requirements in absorption and thermal noise for the test mass mirrors of the cryogenic, low frequency Einstein telescope interferometer as reported by its conceptual design study [Abe11a, Cra19].

3.5.5 Mixture of Titanium Dioxide and Germanium Dioxide

A material mixture of 44 % TiO_2 (titania) and 56 % GeO_2 (germania) has recently been identified to have promising properties for potential HR test mass coatings used in future GWDs [Vaj21]. With a refractive index of 1.88 at 1064 nm the mixture could serve as a high refractive index material for GWD test mass coatings. After the heat treatment, it shows a low mechanical loss at RT as well as a low optical absorption that only slightly surpasses the requirements for the next update of the aLIGO detectors. However, based on absorption measurements of pure germania single layers it is thought to be possible to reduce the absorption by optimisation of the coating deposition parameters. The total thermal noise at RT of an HR coating made of this titania-germania mixture and silica as a low refractive index material would be lower by about a factor of two compared to the current coatings used in aLIGO. At cryogenic temperatures, the mechanical loss was not investigated for the titania-germania mixture because the loss is expected to be relatively

high and surpass the requirements of future GWDs since a high loss is reported for pure germania at low temperatures [Rau95, Top96].

3.5.6 Amorphous Silicon

A very promising candidate material for coatings of future GWD test masses is amorphous silicon (aSi). The properties and deposition parameters of aSi were the main areas of research for this thesis. It is the only material currently considered that is made of only one atomic species. A benefit thereof is that the proper stoichiometric deposition of material onto the mirror substrate does not need to be monitored, eliminating a potential point of failure during the production of the test mass coatings. The refractive index of aSi at relevant wavelengths is the highest of all materials considered, although it strongly varies with the deposition parameters and potentially with heat treatment. It ranges from about 2.7 as found in some coatings from my own deposition experiments (see section 5.3.4) up to 4 in the literature [Fre82]. An HR coating using aSi as a high refractive index material would therefore be much thinner compared to a coating using one of the oxides discussed here, resulting in a significantly reduced coating thermal noise. The aSi coatings with a very low refractive index were produced using deposition parameters which I now deem unlikely for coatings intended for use in GWDs because the production process including the refractive index will be optimised to reduce the thermal noise. I would therefore expect a refractive index of at least 3.4.

The mechanical loss of aSi is miniscule at cryogenic temperatures but also at RT it is still moderate compared to currently used titania doped tantala [Liu14, MR21, Mur15, Ste18a, Ste18b]. In combination with the expected low total thickness, it shows the potential for a coating with greatly reduced thermal noise. However as a sole high refractive index material, the optical properties of aSi currently does not fulfil the design requirements of future GWDs. The optical absorption of aSi is strongly dependent on the considered wavelength. In the near infrared, higher wavelengths correlate to lower absorption values [Pie72, Ste18b], urging for higher wavelength to be utilized. Although there were already big improvements in the past by optimising the deposition method and speed as well as the heat treatment temperature [Bir18, Ste16b], the optical absorption of aSi still exceeds the planned specifications and its further reduction is the subject of ongoing research activities. The optical absorption of aSi in my own associated experiments are discussed in detail in chapter 5. Nevertheless, as of today aSi could in combination with silica, titania doped tantala and perhaps hafnia already be implemented in multi-material coating designs to improve the thermal noise of GWDs [Cra19, Ste21, Tai20]. Here, the amount of thermal noise reduction is determined by the amount of aSi that could be implemented in such coating designs which in turn is limited by its absorption. In summary, aSi is mainly an option for cryogenic interferometers at higher wavelengths, but also RT detectors might slightly benefit from utilizing it.

3.5.7 Silicon Nitride

The material mixture of silicon with variable amounts of nitrogen and hydrogen (SiN_xH_y) is currently being researched as a potential coating material for test masses of cryogenic GWDs. The mixture is an amorphous solid and commonly referred to as silicon nitride. Due to its varying stoichiometry the properties of different silicon nitride compositions cover a relatively wide range. The refractive index ranges from about 1.8 to 2.3 between 1000 nm and 2000 nm [Pan18b, Ste17]. The mechanical loss of silicon nitride can be exceptionally low at cryogenic temperatures depending on its exact composition, but also at RT a slight improvement compared to current titania doped tantala layers was measured [Pan18b]. Therefore, silicon nitride could, at RT, serve as a high index material in combination with silica or in cryogenic interferometers as a low index material accompanying amorphous silicon. The optical absorption however is currently still too high for implementation in a classic two-material HR coating [Gra20b, Ste17]. Nevertheless, it is anticipated to be improved in future research as silica nitride coating layers have a wide possible range of compositions and only a few have been studied so far [Pan18a]. All in all, silicon nitride is a promising candidate material mainly for cryogenic GWDs if the absorption improves as expected in future studies.

3.5.8 Aluminium Gallium Arsenide

A multilayered, monocrystalline HR mirror coating can be manufactured using only aluminium gallium arsenide (AlGaAs) by changing the amount of aluminium in the different layers. The low refractive index layers have a very high amount of aluminium typically around 92 % and only a small amount of gallium with 8 % while the high index layers normally consists of pure gallium arsenide (GaAs) without any aluminium doping. The refractive indices are quite high at 2.98 and 3.48 respectively for the described case. AlGaAs coatings show both excellent optical and mechanical properties at RT and at cryogenic temperatures as well [Col13, Col16, Mar18]. An optical scattering as low as 3 ppm was reported for an HR coating while the absorption even reaches sub-ppm levels. In combination with the miniscule mechanical loss, a more than tenfold suppression of thermal noise compared to current test mass coatings seems possible.

The disadvantage of AlGaAs as a coating material for interferometer mirrors of GWDs lies in its production process and its implementation in GWDs. As a monocrystalline material, the coatings need to be grown on substrates made of materials with suitable crystal lattices. In addition, restrictions for the thickness during the epitaxial growth limit the substrates to thin wafers. This means the coatings have to be grown on GaAs wafers and afterwards transferred to suitable substrates to be used in GWDs. Although the transfer process could introduce additional defects or deviations, it was shown that an HR AlGaAs coating produced in this way only narrowly misses the strict requirements of present interferometers [Koc19]. However, GaAs wafers are currently not available at the sizes needed for future GWDs. It might be possible to extend the production sizes to a fitting format for GWDs but it is unclear how this would affect the quality of the coating

especially regarding the influence of the transfer process. In summary, AlGaAs coatings would be excellently suited for future GWDs if the problems regarding their production process can be solved.

Chapter 4

Photothermal Common-Path Interferometry

4.1 Measurement Concept

Photothermal common-path interferometry (PCI) is a technique for measuring the optical absorption of optical components. It utilizes a pump-probe approach to sense the disturbance of a laser beam created by a local temperature increase inside an optic, which in turn is caused by the absorbed light power of a second laser beam. By comparison to the signal of a known calibration sample, it is possible to determine the strength of the absorption. The PCI technique was used to measure all absorption values presented in this thesis.

The PCI principle can be divided into two parts. In the first part, the actual absorption signal arises while the second part consists of the so called imaging stage which makes the measurement of the absorption signal possible in the first place by shifting the ideal measurement position onto a photodetector.

4.1.1 The Signal Formation

Two Gaussian laser beams of different wavelengths are required for PCI measurements: one pump beam and one probe beam. The pump beam has a much higher power compared to the probe beam and is focused down to a smaller beam waist of about a factor of two to four [Lei15]. As a consequence of its small waist, the pump beam creates an area of high intensity at its focus. Both beams overlap at an angle so that their foci are at the same position, as it is depicted by figure 4.1. The spacial evolution of both beams is given by the spot size parameter $w(z)$. It describes the $1/e^2$ beam radius at point z relative to the waist position for a Gaussian beam propagating in z direction and is given by [Car80]

$$w(z) = w_0 \sqrt{1 + \left(\frac{z}{z_R}\right)^2}, \quad (4.1)$$

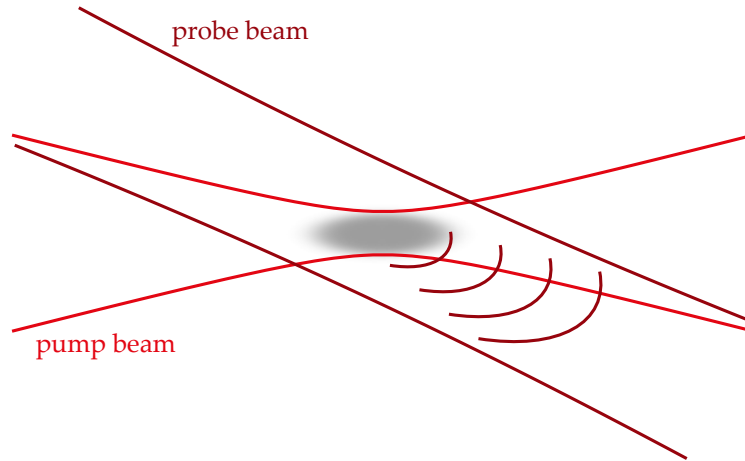


FIGURE 4.1: Schematic depiction of the beam crossing point in the PCI technique. The high-power, small-focus pump beam is partly absorbed by a medium and creates an area of elevated temperature. The low-power, larger-focus probe beam is disturbed at its centre causing light to partly scatter into a new mode. Afterwards, both modes interfere with each other, creating an alteration of the original transversal beam profile.

where

$$z_R = \frac{\pi w_0^2 n}{\lambda} \quad (4.2)$$

is the Rayleigh length, w_0 is the waist size, λ is the wavelength and n is the refractive index.

For the absorption measurement, the sample of interest is placed at the beam crossing point. The pump beam is then partly absorbed and heats the sample, especially at the described high intensity area. As a consequence, several effects can occur with their strength depending on the material properties of the sample [Ale09]. In general, the refractive index n changes with the temperature T ($dn/dT \neq 0$). Also, a thermal expansion of the sample material can arise, slightly changing the sample's geometry. In addition, the thermal expansion can produce a photoelastic refractive index change due to induced local stresses inside the material. All described phenomena effectively result in the formation of a small thermal lens at the focus of the pump beam.

The larger-focus probe beam crosses the heated area and experiences the induced thermal lens at its centre. Please note, that due to the beam crossing angle, the thermal lens appears to be tilted for the probe beam making it slightly asymmetric. However, if we assume a small crossing angle, the influence of the asymmetry can be neglected. The central beam distortion creates a perturbation of the beam front, which can be described by the appearance of a new weak light mode of the same wavelength and propagating in the same direction as the original probe beam [Ale09]. Since the heating effect of the pump beam is of Gaussian shape, so is the distortion of the probe beam and in extension also its new mode. Therefore, it is initially equal in size to the smaller pump beam. There is a linear correlation between the amount of absorbed light power and the strength of

TABLE 4.1: List of basic parameters used for the simulations of the PCI technique. The chosen parameters correspond to the Hamburg PCI system.

Parameter	Value	Unit
pump beam waist size	35	μm
probe beam waist size	105	μm
probe beam wavelength	1310	nm
probe beam power	1	mW
strength of perturbation	1	%

the perturbation mode, which is the prerequisite to later determine the absorption of the sample.

During their continued common-path propagation, the undisturbed probe beam and the weak perturbation interfere with each other. The nature of the interference changes with the propagation distance as a result of the difference in size which is leading to two effects: Both parts not only undergo different divergences as described by equation 4.1, but also experience distinct Gouy phase shifts [Fen01]. For a Gaussian beam propagating in z direction, the Gouy phase shift $\psi(z)$ is given by

$$\psi(z) = \arctan\left(\frac{z}{z_R}\right). \quad (4.3)$$

At last, the interference of the beams generates local intensity variations compared to an undisturbed probe beam. To continuously measure these variations, the pump beam is chopped at typically a few hundred hertz. That way, the sample is periodically heated. By monitoring the intensity variations, a signal at the chopper frequency proportional to the absorbed light power can be detected.

The analytical and mathematically rigorous description of the induced intensity variations and their origin through the formation of the thermal lens requires extensive theoretical work. Such a description for a slightly modified PCI setup can be found in [Vla18]. For a better understanding of the PCI technique, I have simulated the formation and detection of the absorption signal using a simplified model. For that I used the open source simulation software *Finesse* embedded in its *Python* wrapper *PyKat*. The complete code including the simulation of the imaging stage described in the next subsection can be found in appendix A.

The simulation model consists of two Gaussian laser beams superimposed on a beam splitter. The beams represent the undisturbed part of the probe beam and its weak perturbation by the thermal lens while the position of the beam splitter represents the beam crossing point. The waist positions and sizes are chosen accordingly to reproduce the physics of an actual PCI system. The parameters I picked for the simulations presented here are shown in table 4.1. They mirror the parameters of the PCI system I set up as part of this thesis project at the University of Hamburg, which is described in section 4.2.

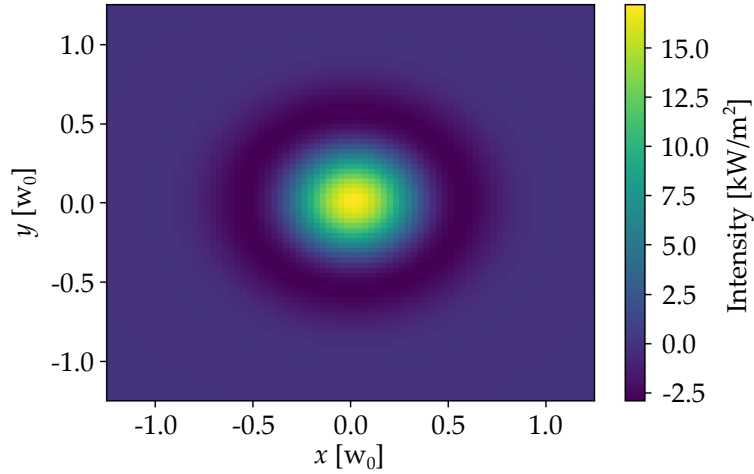


FIGURE 4.2: Simulation of the transversal intensity map of the difference between the undisturbed and perturbed probe beam. The x and y positions are displayed in terms of $w_0 = 105 \mu\text{m}$. The distance to the beam crossing point is 3 mm.

However, due to the simplification of the model, certain aspects of a real PCI system cannot be emulated. First, both simulated beams are perfectly Gaussian disregarding any spacial imperfections that could be present in the pump or probe beams. The aforementioned asymmetry as the result of the beam crossing angle is also ignored. In addition, the perfect overlap of both beam foci omit the influence of not perfectly aligned waist positions. Finally, the actual formation of the thermal lens and its influence on the beam profile is more complex than the addition of a second Gaussian beam, which is limiting the accuracy of the simulation results. Nevertheless, based on the behaviour of the Hamburg PCI system, the simulation still offers an accurate representation of real, well aligned PCI systems, even with these limitations present. It can therefore be used to study some fundamental correlations of the PCI measurement technique.

The simulation result of the difference between the undisturbed probe beam and the beam when it experiences the absorption induced thermal lens is shown in figure 4.2. Depicted is a transversal intensity map at a distance of 3 mm after the beam crossing point. The positions in x and y direction are displayed in units of the original waist size of the beam at $w_0 = 105 \mu\text{m}$. In the centre, the disturbed laser beam has a significantly higher intensity than the originally undisturbed beam. Around this central part, there is an area of lower intensity, which is necessary to fulfil the energy conservation as the probe beam has the same total power in both cases. In the far field, there are no differences between the two cases as it would be expected. That means, if the power of the whole probe beam is measured, there would be no difference detected between both cases. Therefore, to deduce the strength of the perturbation, only the central part of the beam should be detected.

The strength of the optical absorption can now be calculated as the probe beam perturbation is linearly correlated to the absorbed light power. By measuring the absorption signal generated by a known sample at given light powers of the probe and pump beams, the PCI system can be calibrated. Afterwards, the signal strength of an unknown sample

needs to be compared to the calibration signal. The level of the optical absorption a can now be evaluated using the following equation [Sta21].

$$a_s = \frac{a_c s_s P_{c,pump} P_{c,probe} \gamma}{s_c P_{s,pump} P_{s,probe}} \quad (4.4)$$

Here, a_s and a_c are the absorptions of the unknown sample and calibration optic respectively, s_s and s_c are their signal strengths generated by the PCI system, $P_{c,pump}$ is the power of the pump beam and $P_{c,probe}$ is the power of the probe beam during the calibration measurement as well as $P_{s,probe}$ and $P_{s,pump}$ are the respective powers during the sample measurement. The exact features of the thermal lens depend on the properties of the measured substrate material. Therefore, a correction factor γ needs to be introduced. It compensates for different materials at the calibration and sample measurement. If the same substrate materials are used, the correction factor can be disregarded, as in that case $\gamma = 1$.

In principle, there are two possibilities to omit the outer area of the probe beam at a power measurement in a PCI system. First, an aperture could be used to chop off the outer beam parts. Afterwards, the complete beam would need to be observed. As the second possibility, a photodetector of the size of the central area could be utilized. If it is placed right at the centre of the beam, only the higher intensity parts would be measured. Both cases are equivalent to each other and would allow for a meaningful comparison of the undisturbed beam with the perturbed one. However, the distance to the beam crossing point is only 3 mm in the simulation shown in figure 4.2. As a result, the high-power pump beam would not be separated enough from the low-power probe beam for a sensitive measurement to take place. Furthermore, a lot of samples are thicker than 3 mm, meaning that for an actual measurement of the simulated signal created by a coating on the sample frontside, it would need to take place inside the sample. In addition, the optimal measurement area would only have a diameter of about $0.75w_0 \approx 79 \mu\text{m}$, which would impede on the correct alignment of a real PCI system. Therefore, a bigger distance to the beam crossing point and a larger measurement area are required.

The spacial evolution of the transversal intensity variations is depicted in figure 4.3(a), while in figure 4.3(b), only the intensity at the centre of the beam is shown. As the variations are rotational symmetric, it is sufficient to display only one transversal direction. The maximum difference in intensity between the undisturbed and perturbed probe beam occurs at a distance of only 2.6 mm after the beam crossing. Interestingly, this is only about $0.72z_R$ of the weak beam perturbation ($w_0 = 35 \mu\text{m}$) and thus less than the often quoted optimal distance of z_R [Ale09]. The difference in these values stems from the often used plane wave approximation of the undisturbed part of the probe beam effectively neglecting the influence of its Gouy phase shift and spacial evolution. At further distances, the beam size increases, which would allow for an easier measurement and alignment of the system, but the absorption signal gets rapidly weaker at the same time. At only 30 mm, the signal strength at the centre already dropped to about 6.3 % of its maximum value. As a consequence, an imaging system is needed so that the measurement of the absorption

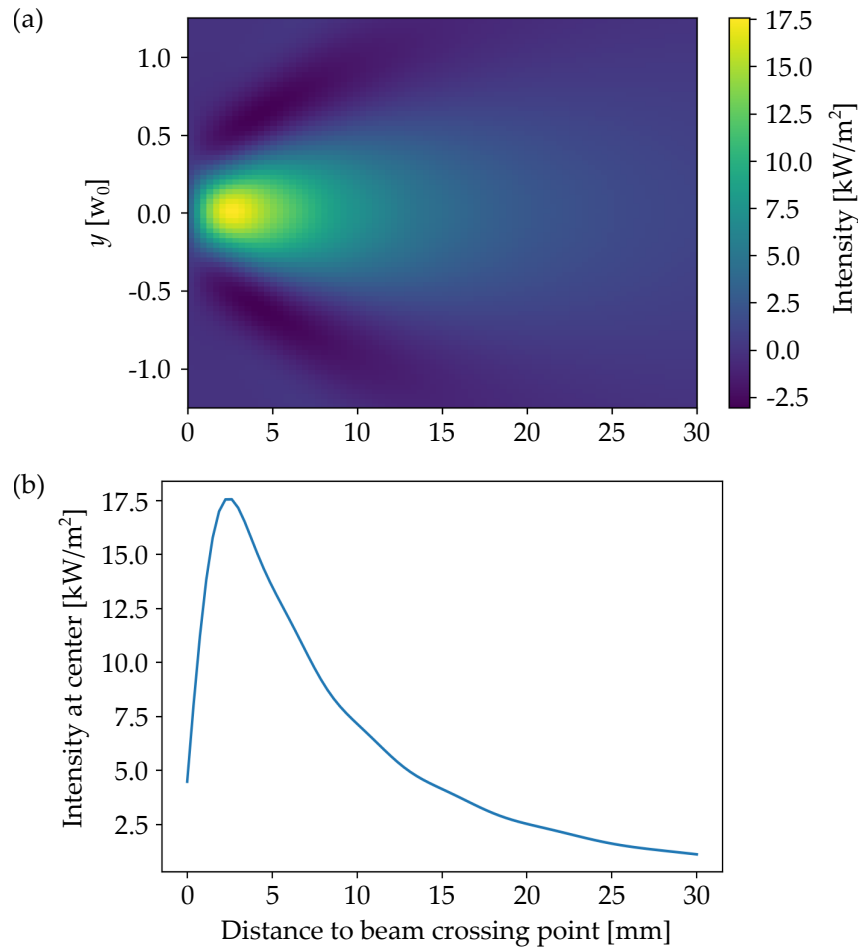


FIGURE 4.3: Simulation of the intensity difference between the undisturbed and perturbed probe beam as a function of the distance to the beam crossing point. Shown is the spatial evolution of the transversal intensity distribution where the y position is displayed in terms of $w_0 = 105 \mu\text{m}$ (a) and the intensity at the centre of the beam (b).

signal can take place over an acceptable large area at a reasonable distance.

4.1.2 The Imaging Stage

The purpose of the imaging stage is to increase the area of measurement for the thermal lens induced beam perturbation and its distance to the beam crossing point, so that it is possible to use a common photodiode as the detector for the PCI technique. In addition, the imaging stage enables to compensate for varying thicknesses of different samples. Its basic principle is that of a Galilean telescope, which consists of two lenses. The first lens focusses the incoming light while the second diverges it again to create the magnification effect. Similar to that, the imaging stage uses a focussing and a diverging lens to enable the absorption measurements via PCI. However, the imaging stage principle often requires the second lens to have a very short focal length, that usually cannot be attained by ordinary lenses. Therefore, strongly curved mirrors sometimes referred to as 'reflecting lenses' are typically used. An example of an imaging stage is shown in the schematic

TABLE 4.2: List of basic parameters used for the simulations of the effects of the imaging stage. The chosen parameters correspond to the Hamburg PCI system.

Parameter	Value	Unit
focal length of the 1. lens	40.0	mm
focal length of the 2. lens	-1.5	mm
distance between the lenses	53.5	mm
distance between 2. lens and photodiode	85.0	mm
photodiode diameter	1.0	mm

depiction of the Hamburg PCI system in figure 4.6, where a polished steel bearing acted as the second lens.

I have simulated the effects of the imaging stage on the discussed intensity variations. The parameters used for the presented simulations correspond again to the Hamburg setup. They are summarized in table 4.2. The lenses are modelled as thin lenses without any aberrations, meaning that their thicknesses are considered to be 0. This might introduce further inconsistencies compared to a real setup, but for the purpose of discussing the imaging stage effects and PCI technique as a whole, it is an adequate simplification.

The transversal intensity distribution at the photodiode position for a varying distance between the beam crossing and the first lens of the imaging stage is depicted in figure 4.4(a). The absolute value of the intensity at the centre of the beam is shown in figure 4.4(b), which is often referred to as butterfly curve. The distances between the lenses and the photodiode were kept constant. The transversal position in x direction is displayed in units of the resulting waist size of the probe beam after it experienced both lenses of the imaging stage at $w_0 \approx 15.8 \mu\text{m}$.

The effects of the imaging stage on the induced intensity variations are substantial. There are now two regions in the intensity distribution of the beam where an absorption signal is present. The region between about 147 mm and 170 mm corresponds to the intensity variations directly after the beam crossing point shown in figure 4.3. There is now a strong signal present, even after the beam propagated a total distance of around 288 mm from the beam crossing point to the photodiode position. Also, the size of the signal area increased significantly compared to the case without an imaging stage. The diameter of the area at the distance where the highest intensity difference is present grew from about $79 \mu\text{m}$ to now $113w_0 \approx 1.79 \text{ mm}$. The region between 120 mm and about 147 mm is an image of a virtual signal region, that is located in front of the measured sample. This region would be present if the perturbed part of the probe beam would exist before it experienced the induced thermal lens. Here, the intensity at the centre of the beam is lower when the probe beam experienced the thermal lens in contrast to the other region, where the opposite is true. The butterfly curve is asymmetric as the size of the probe beam varies with the distance to the beam crossing point. Since the strength of the beam

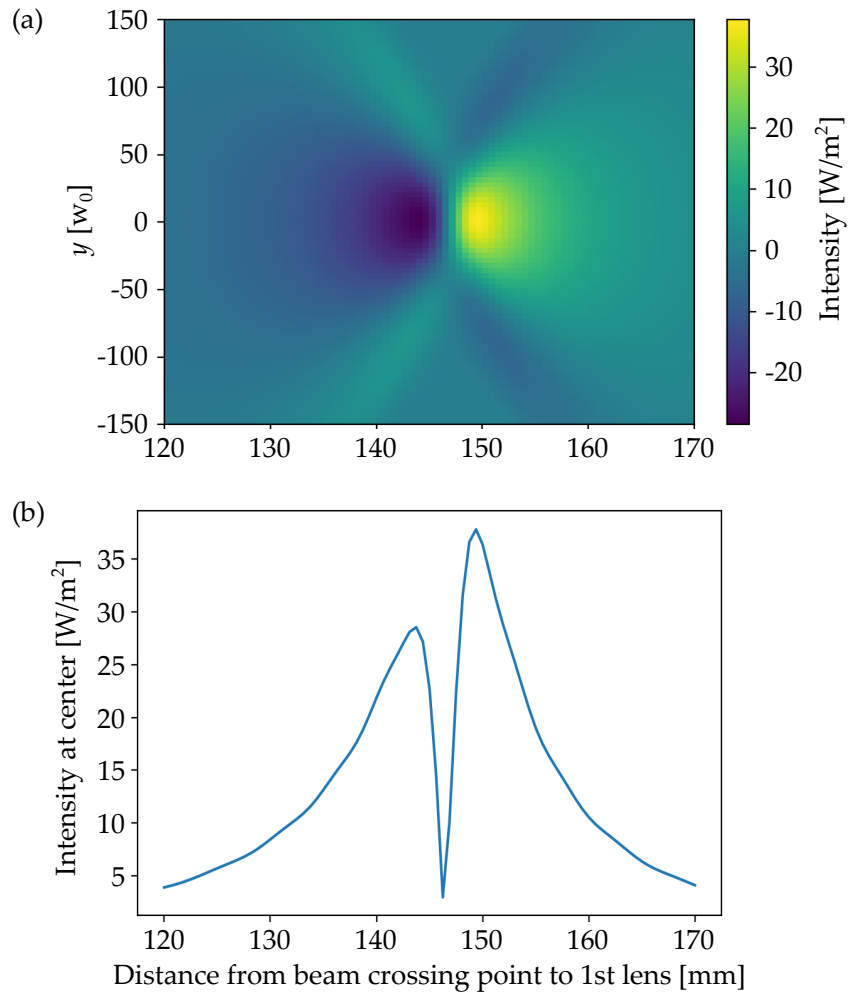


FIGURE 4.4: Simulation of the intensity difference between the undisturbed and perturbed probe beam as a function of the distance from the beam crossing point to the first lens of the imaging stage. Shown is the transversal intensity distribution at the photodiode where the y position is displayed in terms of $w_0 \approx 15.8 \mu\text{m}$ (a) and the intensity at the centre of the beam (b), which is also known as the butterfly curve.

perturbation is detected by measuring the intensity variations, both signal regions can be utilized to determine the absorption level of the sample.

The photodiode measures the power of the central area of the final beam corresponding to its size. The magnitude of the signal is not only dependent on the central intensity variations shown in figure 4.4(b) but also on the overlap of the beam region that is carrying the signal and the area of measurement determined by the photodiode. Depending on the distance from the beam crossing point to the imaging stage, the measurement area can be smaller, larger or equal in size compared to the signal region. The simulated detection of the butterfly curve by the photodiode is shown in figure 4.5(a). Compared to the intensity variations at the beam centre, each signal maxima shifted slightly, from originally 143.8 mm and 149.4 mm to 143.1 mm and 150.0 mm respectively. At these distances, the absorption signal strength has only marginally decreased, while the signal region overlaps greatly with the photodiode, as can be seen in figure 4.5(b). Shown are the transversal

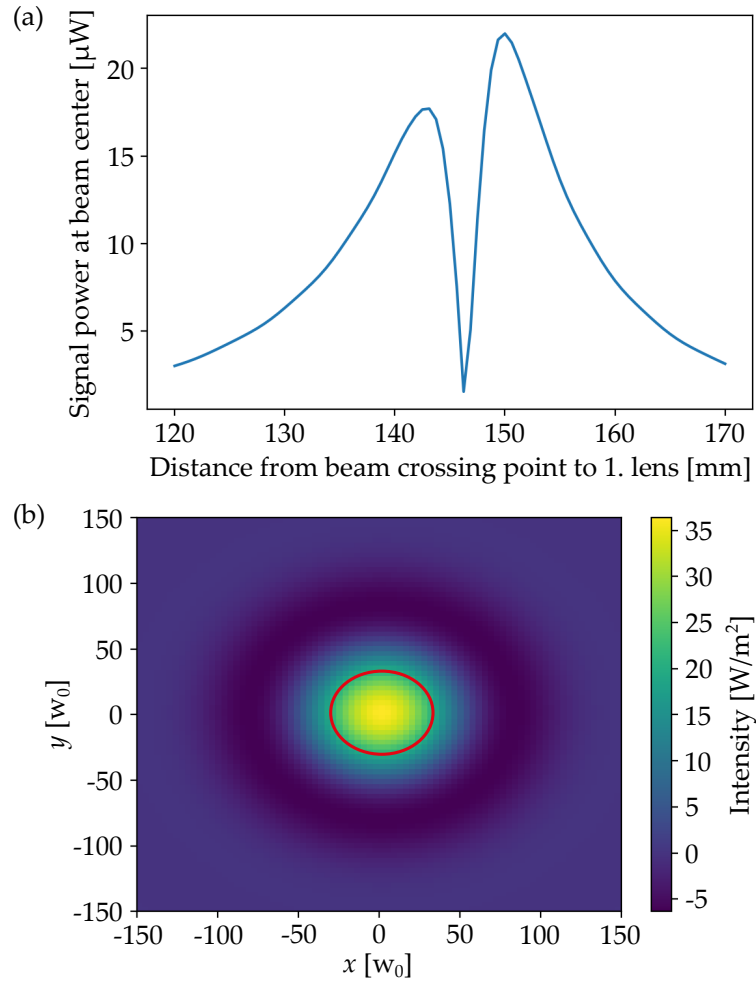


FIGURE 4.5: Simulation of the detection of the butterfly curve by the photodiode. Shown are the butterfly curve itself (a) and the transversal intensity variations at a distance of 150 mm from the beam crossing point to the position of the first lens (b). At this distance, the highest signal is detected by the photodiode. Its size is depicted by the red ellipse. The x and y positions are displayed in terms of $w_0 \approx 15.8 \mu\text{m}$.

intensity variations at 150 mm, where the size of the photodiode of 1 mm is depicted by the red ellipse.

The calibration of the PCI system and the subsequent measurements should always take place at the same maximum of the butterfly curve to ensure an identical sensitivity of the system. All samples need to have flat surfaces because any curvature would create an additional lens affecting the whole imaging system. In addition, samples with different refractive indices or of different thicknesses introduce an offset to the distance where the butterfly curve appears. The reason for that is the differences in refractive indices between the samples and the surrounding air. This effects the Rayleigh length (see equation 4.2) and in extension also the self-interference of the probe beam. Different sample thicknesses therefore need to be compensated for by shifting the imaging stage appropriately as it is described by the following equation [Sta21], which can be directly deduced from the effect

of the refractive index on the Rayleigh length.

$$z_{\text{IS, new}} = z_{\text{IS, old}} - \frac{(n_{\text{old}} - 1)d_{\text{old}}}{n_{\text{old}}} + \frac{(n_{\text{new}} - 1)d_{\text{new}}}{n_{\text{new}}} \quad (4.5)$$

Here, $z_{\text{IS, new}}$ and $z_{\text{IS, old}}$ are the new and old positions of the imaging stage, n_{new} and n_{old} are the refractive indices of the old and new sample and d_{new} and d_{old} are their respective thicknesses.

The PCI technique is suitable for measuring the surface absorption of thin coatings as well as the bulk absorption of thick samples. A bulk absorption signal resembles many surface signals overlapping and interfering with each other. This interference depends on the sensitivity of the PCI system, its general alignment and the beam crossing angle which dictates the interaction length between the pump and probe beam. While it is in principle possible to calculate the influence of the interference on the response of the PCI system, it is arduous and often inaccurate. A much more practical solution is the usage of different calibrations for both absorption types. For this thesis, I only measured the surface absorption of coated samples.

4.2 The Hamburg PCI System

During the course of this thesis project, I set up a PCI system at the *Institute of Laser Physics* of the University of Hamburg. It was used to measure some of the absorption values presented in this thesis. A schematic depiction of the system's setup is shown in figure 4.6. The remaining measurements were done by various colleagues using a similar system at the *School of Physics and Astronomy* of the University of Glasgow [Tai21].

The Hamburg PCI system employed two pump lasers of different wavelengths. The first was a *Mephisto 2000NE* manufactured by *Coherent*, formerly *Innolight*. It is a solid state laser with a wavelength of 1064 nm capable of up to 2 W of optical power. The laser beam was coupled to a short single-mode fibre, which acted as a mode cleaner, resulting in a clean TEM_{00} pump mode. The second laser beam at 2128 nm was generated by a setup build by Christian Darsow-Fromm *et al.* [DF20] in a neighbouring laboratory using optical-parametric oscillation of a 1064 nm beam. It was transferred via a single mode fibre to the optical table of the PCI system. The pump beams were chopped at 407 Hz and redirected by various HR mirrors to the beam crossing point, at which they were focused down to a beam waist of about $w_0 = 35 \mu\text{m}$. During all absorption measurements only one of the beams was active while the other one was blocked. The samples to be measured, situated at the beam crossing point, partly absorbed the active pump beam which resulted in the formation of the thermal lens. During each measurement, the pump power was monitored by a thermal power meter.

The probe laser was a fibre coupled semiconductor laser manufactured by *Thorlabs*. The wavelength was 1310 nm and during the absorption measurements its power amounted to approximately 2.2 mW. Like the pump lasers it was redirected to the beam crossing

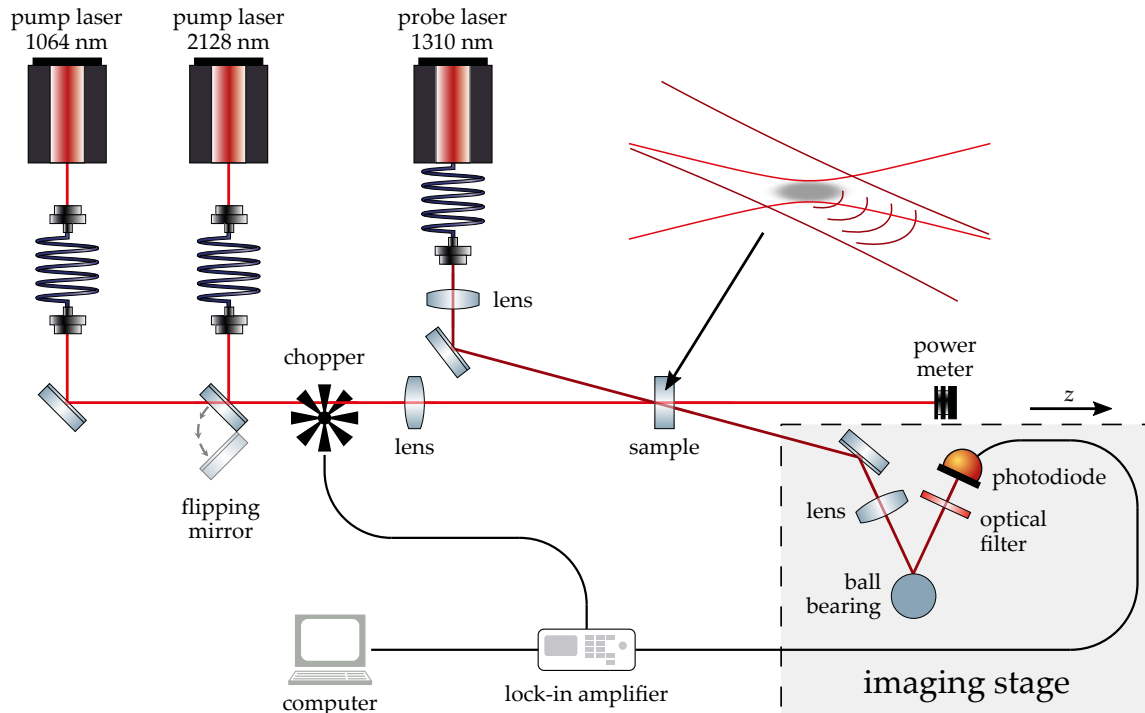


FIGURE 4.6: Schematic depiction of the PCI system at the University of Hamburg. The sample is held in an xyz translation stage and the whole imaging stage can be moved in the z direction.

point and focussed down to a waist of about $w_0 = 105 \mu\text{m}$, where the beam picked up the thermal lens induced absorption signal created by the active pump beam. The beam crossing angle was 15° . The imaging stage consisted of a redirection mirror, a focussing lens with a focal length of 40 mm, a polished steel ball bearing acting as the diverging lens with a diameter of 6 mm, an optical bandpass filter at 1310 nm and a photodiode. The whole stage was built on a translating table, enabling the stage to be moved in the z direction to compensate for different sample thicknesses and for an easier alignment of the system. The optical filter prevented the photodiode to detect ambient light or scattered parts of the pump beams and therefore ensured an accurate detection of only the probe beam.

The photodiode absorbs the light of the probe beam and converts it into a voltage. The output was electronically split into an, on the short timescale, constant signal referred to as the DC part and an alternating part. A lock-in amplifier was used to filter the alternating part for the absorption signal at the chopper frequency. This signal is referred to as the AC part. The lock-in amplifier was connected to a computer, which was used to analyse the resulting signals and to determine the optical absorption of the measurement sample.

The PCI system was aligned at the second maximum of the butterfly curve for all absorption measurements presented in this thesis. Its form and position matched, within measurement accuracy, the curve produced by the simulation shown in figure 4.5(a). The largest inaccuracies stemmed from the various measurements of the distances the probe

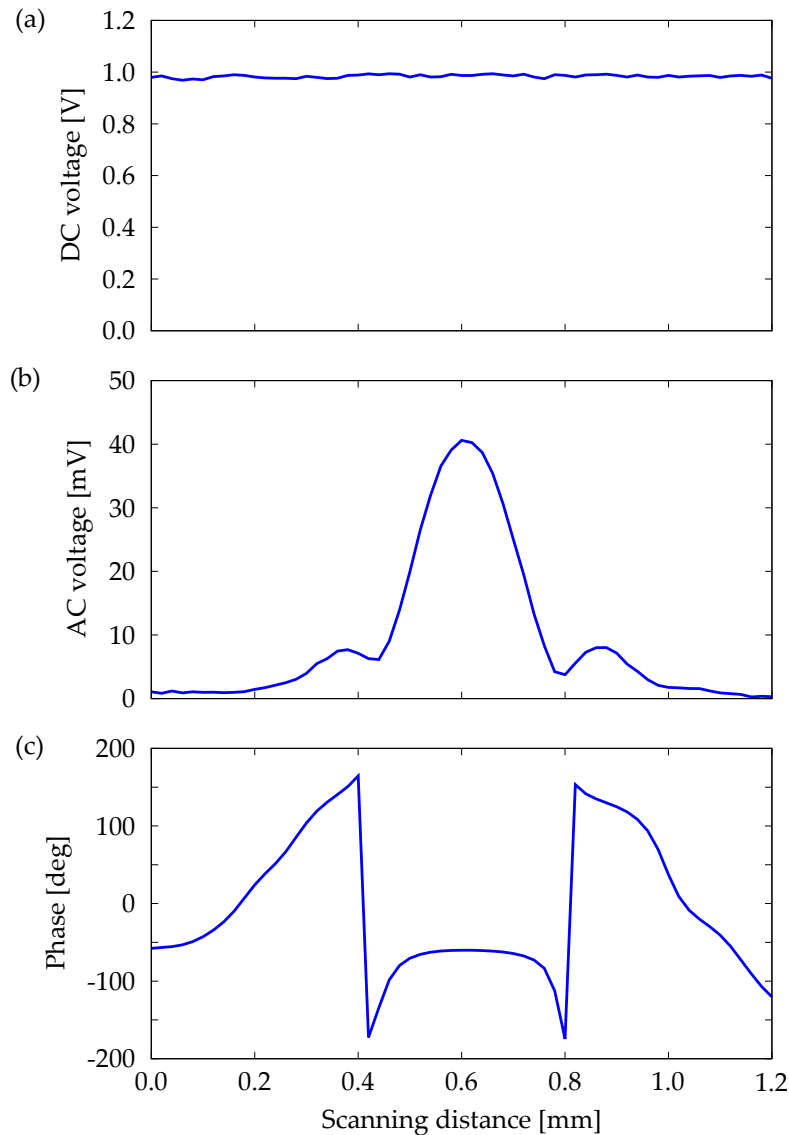


FIGURE 4.7: Example absorption measurement of a coated sample carried out by the Hamburg PCI system. Shown are the DC voltage (a), AC voltage (b) and its phase (c) in dependency of the z position of the sample.

beam travels in the real system between the different components, which were only precise to about 1 mm each.

4.3 PCI Measurements

During an absorption measurement, the sample is moved in steps on the z axis through the beam crossing point. For every step, the photodiode data is recorded. An example measurement of a coated sample with negligible substrate absorption is presented in figure 4.7. Shown are the DC signal (a), the AC signal (b) and the relative phase between the chopper position and the AC signal (c). The DC voltage experienced only small fluctuations as the probe beam power was held constant and the optical setup was relatively stable. The AC voltage on the other hand showed a strong variation as the sample is

moved through the beam crossing. The central maximum correlates to the total absorption of the coating. The peak height is calibrated with a known sample, to which the AC signals of subsequent measurements are compared as described by equation 4.4.

The phase of the signal at its central peak is about -60° . A phase of 0° corresponds to the absorption signal appearing at the moment where the pump beam is unblocked by the chopper. The phase depends on the time it takes for the thermal lens to form and in addition to some extent on the specific setup as the exact detection of probe beam perturbations varies to some extent. There are two smaller side peaks present on the AC signal. These correspond to probe beam interferences similar to the area around the central signal on the transversal intensity map depicted in figure 4.5(b), which could be measured by moving the photodiode off centre. For these interferences, the absorption induced intensity changes of the probe beam are reversed compared to the central peak, which is interpreted as an 180° phase flip. The phase would also be flipped for the complete measurement if the setup was aligned on the first maximum of the butterfly curve. The phase can therefore serve as a powerful alignment tool to find the correct imaging stage distances and photodiode position.

The pump laser experiences a varying amount of power build up inside the coatings of different samples during their measurement. This build up depends on the exact layer design of the respective coating (see section 3.1), which also influences the optical absorption of the coating (see section 3.2). As a PCI system measures the total absorption of a coating, a further evaluation of the measurements of single layered coatings is required to receive the thickness normalized absorption of the coating materials. For the coatings presented in this thesis, the evaluation was done using a *MATLAB* script written by Zeno Tornasi (University of Glasgow). The script calculates the thickness normalized absorption in form of the extinction coefficient k , which was introduced in section 3.2, by utilising a model that takes interference effects into account. Multilayer coatings cannot be analysed in the same way to receive the individual k values of the employed materials as their different contributions cannot be separated from each other.

For each absorption measurement, I assumed an error of approximately 10% of its value due to slight variances in the calibration and subsequent measurement processes. The absorption of each coating was measured multiple times at varying positions to check for inconsistencies due to impurities or dirt on the sample. These values were then averaged on their standard deviations were calculated, which mostly were well below the initial 10% error. The later depicted errors on the absorption values therefore represent this 10% or correspond to the standard deviation in the occasional cases where it exceeds that value. In the end, it was thereby possible to directly compare coating materials and deposition parameters independent of the influences from different power build ups or coating thicknesses.

Chapter 5

Deposition of Amorphous Silicon Layers

5.1 Pulsed Laser Deposition

Pulsed laser deposition (PLD) is a technique for growing thin films on substrates. It belongs to the category of physical vapour depositions, meaning some physical effect caused the to-be-deposited material to go into a gaseous or plasma state prior condensing on a substrate. In the case of PLD, short, high-energy laser pulses are focused on a target composed of the deposition material. This leads to the evaporation of material, which then accumulates over time on a substrate, forming a thin film. It is a 'clean' process that does not utilize other atomic species unlike many other deposition methods such as the commonly used ion beam sputtering.

In the present day, the PLD technique is scientifically and commercially used in various thin film technologies, like microelectromechanical systems and coated-conductor applications [Gre13]. As part of this thesis, PLD was utilised to deposit amorphous silicon layers (see subsection 5.1.3) that were analysed in terms of their properties relevant for a possible application in mirrors for GWDs (see section 5.3). A thorough discussion on PLD in general and its applications can be found in [Eas07].

5.1.1 The PLD Process

In this subsection, the process of PLD is described in a compact way, following the discussion found in [Sch09]. The PLD process is visualized in figure 5.1 and can be divided into five steps, that are repeated with every consecutive laser pulse:

1. The target absorbs a short, high-energy laser pulse.
2. The target material experiences an initially one dimensional expansion.
3. The expansion of the target material becomes three dimensional.
4. The ablated material is potentially slowed down by a background gas.
5. The ablated material is accumulated on a substrate.

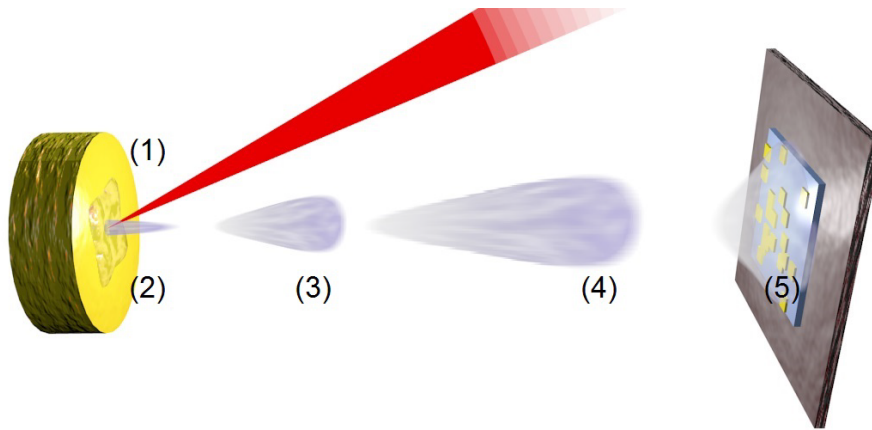


FIGURE 5.1: Visualisation of the five steps of the PLD process. Figure was taken from [Wae16].

At first, a focussed, high-energy laser pulse irradiates the target inside a vacuum chamber. The light is absorbed and subsequently heats the material to temperatures far exceeding its boiling point (1). This leads to an explosive expansion and the material is ejected in a plasma plume perpendicular to the target surface (2). Typically, a thermal equilibrium is already reached after tens of picoseconds and thus the expansion starts long before the pulse, which length is usually in the nanosecond range, vanishes. In this early expansion, the pulse is directly absorbed by the ejected atoms, ions and electrons. The temperature of the plasma plume during this stage can rise up to 20 000 K and the pressure inside the plume may reach up to 10 bar. In the later progression, the plume expands adiabatically in three dimensions while moving in a strong forward direction (3). In a vacuum, the ablated particles will eventually reach a constant velocity. A background gas on the other hand slows the ablated material further down until the particles in the previously confined plume mix with the background gas (4). This process typically happens on a timescale of about tens of microseconds. During this stage, the ejected atoms are prone to chemical reactions, which can deliberately be used in combination with reactive gases such as oxygen or nitrogen to produce for example oxides and nitrites. In the end, part of the ablated material meets the substrate where it can accumulate to form a thin film on the substrate (5).

Between each pulse, the position at which the laser irradiates the target is shifted slightly to prevent the formation of a narrow hole in the target's surface. This not only warrants a larger ablation area of the target and therefore a more efficient use of its material, but also prevents possible changes in the formation of the plasma plume. These changes could arise due to a rising local temperature and an increasing amount of surrounding material, which would physically restrict the plasma plume as the forming hole becomes deeper.

The detailed behaviour of each of the described steps can strongly depend on the deposition parameters and on the target material. However, the typical deposition parameters used in PLD often minimize the differences between different target materials, especially in steps one to three. Therefore their influence on the final coating properties is reduced

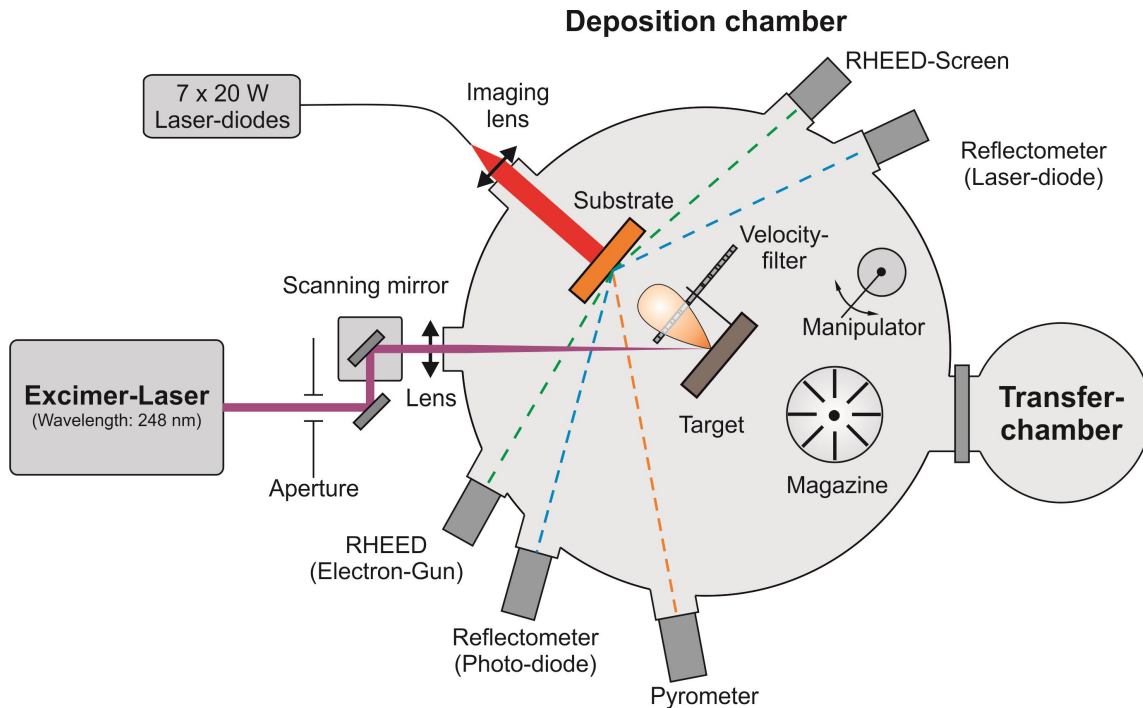


FIGURE 5.2: Schematic depiction of the PLD system at the University of Hamburg. Figure was taken from [Wae13]

as well [Kre03]. This complex behaviour is especially important to consider if targets consisting of multiple atomic species are used to ensure stoichiometric deposition and to get the desired atomic mixture for the produced coating [Fab00]. However, as PLD was only utilized during this thesis project to produce pure silicon layers, stoichiometry affecting phenomena were here of no concern.

5.1.2 The Hamburg PLD System

The PLD system at the *Institute of Laser Physics* of the University of Hamburg is schematically depicted in figure 5.2. It consists of an excimer laser, two connected vacuum chambers and several auxiliaries. Excimer lasers are gas lasers, that mostly use noble gas halides to generate ultraviolet laser pulses. In the Hamburg system, a *LPX 305I* laser manufactured by *Coherent*, formerly *Lambda Physik*, was utilized. This laser is able to generate pulses at 248 nm with a pulse length of about 20 ns. The pulse energy can reach up to 1.2 J while the repetition rate can be varied in 1 Hz steps from 1 Hz to 50 Hz.

In the deposition chamber, the target and substrate were located during the PLD process. In front of the target a rotating vane velocity filter was installed to reduce the amount of undesired, slower-moving particles reaching the substrate like big atomic clusters that might be produced during the normal laser ablation process [Tel12]. The thin film growth was monitored by a reflectometer: The beam of a laser diode with a wavelength of about 690 nm was reflected by the sample at an angle of 20° and afterwards detected by a photodiode. As the reflectivity varies with the thickness of the thin film, its growth could be approximately retraced in real time. The temperature of the sample was monitored

by an infrared pyrometer. The crystal structure of the deposited thin film could be examined by an implemented reflection high-energy electron diffraction (RHEED) system. However, as only amorphous coatings were produced using the PLD setup, it was not meaningful to make use of this possibility. An array of seven laser diodes with a variety of wavelengths in the near infrared spectrum and a power of up to 140 W could be used to heat the substrates. Their light was transferred via a fibre optic cable into the deposition chamber where it irradiated an optical absorber positioned on the backside of the substrate. The absorber transferred the heat into the substrate through a 50 μm thin silver foil, which was used to improve the thermal contact. The smaller transfer chamber in combination with a motorized manipulator arm and a sample magazine in the main chamber made it possible to keep the deposition chamber evacuated while changing the targets and substrates after every coating run.

5.1.3 Sample Production

I utilized the PLD setup at the University of Hamburg to produce all samples discussed in this chapter. During the course of this thesis, a total number of 46 amorphous silicon (aSi) coatings was deposited on two different types of fused silica substrates. This was carried out in cooperation with Daniel Axmann, Malte Behrendsen and Felix Pein, who I supervised during their respective bachelors and masters theses [Axm18, Beh18, Beh21, Pei19].

Not all coatings produced could be used in meaningful scientific research. Some coatings were produced to test adjustments or alignments of the setup, new equipment or the general state of the system. In addition, errors or unforeseen influences could occur during the deposition procedures which rendered some samples to be only partly useful or even unusable. The most common error was the accidental ablation of parts of the target holder due to an incorrectly adjusted ablation area. In the end, I thoroughly analysed a total of 28 aSi coatings, which are listed in table 5.1. However, there were still some inconsistencies present in some layers or during their respective depositions, which I did not deem substantial enough to immediately disregard these coatings as well. Still, these circumstances made it necessary to consider their comparison with the other coatings with care. The inconsistencies are explained with more detail in section 5.3, where also the results of the coating analysis are presented. A complete list of all produced samples including their key deposition parameters and the reasons for disregarding certain coatings can be found in appendix B.

The aSi layers were deposited in five series with each series consisting of nine or ten coatings. For each of the first three series, one parameter was systematically varied, while the remaining parameters were held constant to investigate their respective influence on the deposited aSi. These parameters were the laser pulse energy E_p , the laser pulse repetition rate f_p and the substrate temperature during the deposition T_{sub} . The coatings of the former two series were deposited on *Corning* 7980 silica (C7980) substrates using 150 000 pulses per coating. For the third series, we used 200 000 pulses to create slightly thicker

TABLE 5.1: List of analysed aSi coatings produced using PLD including their defining deposition parameters and occurred inconsistencies.

Designation	E_p (mJ)	f_p (Hz)	T_{sub} (°C)	F_g (SLM)	Inconsistencies
E1	400	10	RT	-	-
E2	550	10	RT	-	-
E3	550	10	RT	-	-
E4	650	10	RT	-	-
E5	750	10	RT	-	-
E6	850	10	RT	-	-
F1	550	5	RT	-	-
F2	550	10	RT	-	-
F3	550	20	RT	-	-
F4	550	30	RT	-	rising pressure
F5	550	40	RT	-	-
F6	550	50	RT	-	possible ablation of target holder
T1	550	15	RT	-	-
T2	550	15	100	-	-
T3	550	15	200	-	-
T4	550	15	300	-	-
T5	550	15	400	-	-
T6	550	15	470	-	unusual thickness distribution
T7	550	15	500	-	unusual thickness distribution, silver foil residues
P1	700	15	RT	-	-
P2	700	15	RT	0.7	-
P3	700	15	RT	1.4	high crystallisation
P4	700	15	RT	2.1	-
P5	700	15	RT	2.9	high crystallisation
P6	700	15	RT	4.2	-
P7	700	15	RT	5.4	high crystallisation
P8	700	15	RT	6.7	-
P9	700	15	RT	8.4	-

layers. In addition, we substituted the C7980 substrates for *Corning* 7979 silica (C7979) ones due to their lower content of residual water and hydroxyl (OH) groups. These residuals create some typical absorption peaks in the near infrared spectrum which overlay the coating absorption at these wavelengths. The difference between both substrates can be seen in figure 5.3, which depicts the measurement of their respective transmission spectra from 200 nm to 3000 nm.

After the third deposition series, a long time break followed where no coatings were produced. It was necessary to replace substantial parts of the systems control electronics and software. This combination required to test and adjust the system anew by depositing several additional coatings. However, it was not possible to exactly recreate the system to the state it was in before, as some alignment information could not be restored from the

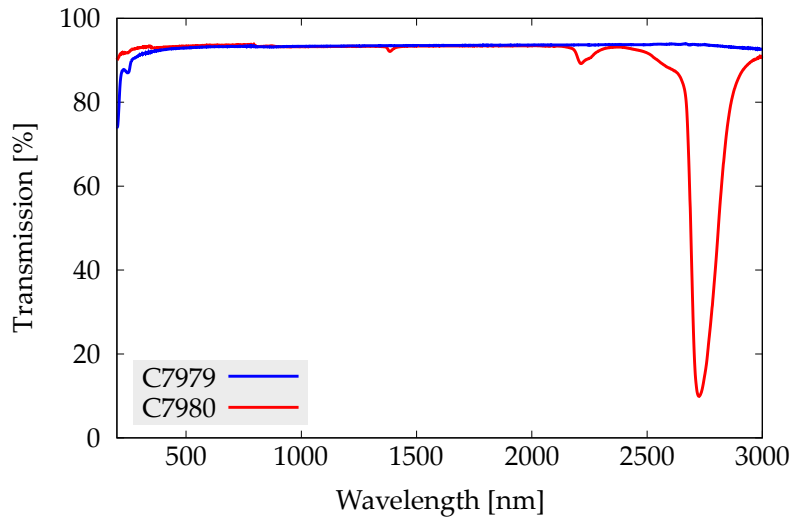


FIGURE 5.3: Transmission spectra measurement of the used C7980 and C7979 substrates. The difference between both substrates stem from the present amount of water and OH groups.

replaced, broken electronics. Moreover, due to the maintenance of the excimer laser, the pulse shape slightly changed altering the ablation process. Therefore, although we tried to come as close to the former system performance as possible, it is not expedient to directly compare later deposited aSi layers to the first three series. This fourth coating series was not further analysed, as it solely served to align and test the modified PLD system.

In the last deposition series, the influence of a background gas at varying pressures was tested. The coatings were still deposited on C7979 by 200 000 pulses each. As a background gas, we used a mixture of 95% argon and 5% hydrogen which was channelled into the deposition chamber using a precision gas flow meter. As a consequence, the vacuum pressure rose from about 10^{-5} mbar without any gas inserted up to about 2×10^{-2} mbar during deposition at a maximum gas flow rate F_g of 8.4 standard litre per minute (SLM). We choose to use argon-hydrogen in this deposition series to test if hydrogen atoms could reduce the number of so called dangling bonds inside the aSi by binding them. This is of interest as in previous studies dangling bonds have been identified to influence the optical absorption of the aSi layers (see subsection 5.4.1). The argon acted mainly as a buffer gas to enable safe handling of the hydrogen. The pressure measurement inside the deposition chamber was imprecise at the relatively high pressures created inside the vacuum chamber during this deposition series. Therefore, I made use of the gas flow measurements in my analysis of the effects the background gas had on the deposited aSi layers.

5.2 Analysing Methods

The deposited aSi layers were analysed in three different ways. Firstly, the optical absorption at varying wavelengths was determined using photothermal common-path interferometry which is described in depth in chapter 4. The pulse-energy series and repetition-rate series were only measured at 1550 nm at the University of Glasgow as the C7980 substrates impeded on the measurements at longer wavelengths. The substrate-temperature series was likewise measured at 1550 nm but in addition also at 2000 nm at the University of Glasgow. I measured the background-gas series using the Hamburg PCI system at both wavelengths of 1064 nm and 2128 nm.

As the second analysing method, I took optical transmission spectra of all produced coatings and afterwards examined them using the software *SCOUT*, which is described in depth in subsection 5.2.1. Through this analysis, I was able to derive a number of coating properties like their physical thickness, wavelength dependent refractive index and the mobility gap energy of the deposited silicon.

At last, I took microscopic images of the samples, which were then investigated regarding the amount of microcrystals present inside the amorphous coatings or on their surfaces. These crystals were unintentionally produced during the coating deposition process. This work was again done in cooperation with Daniel Axmann, Malte Behrendsen and Felix Pein [Axm18, Beh18, Beh21, Pei19]. The exact analysing method is explained in subsection 5.2.2.

5.2.1 Transmission Spectra Analysis

I measured the transmission spectra of all aSi layers using a *Cary 5000 UV-Vis-NIR* spectrometer produced by *Agilent*. This is a double beam spectrophotometer, that offers precise measurements over a wide wavelength range. All spectra were taken from 200 nm to 3000 nm at an interval of 1 nm with a bandwidth of 3 nm and an integration time of 0.1 s. These spectra were then analysed using the software tool *SCOUT* by the company *WTheiss Hardware and Software*. It uses a physical model to simulate the transmission of aSi coated silica substrates, which were then fitted to our samples to determine their properties.

The basis of the model utilised by *Scout* is the so called OJL model, which describes the energetic distribution of electronic states possible in an amorphous semiconductor [O'L97], as it is depicted in figure 5.4. Like in crystalline semiconductors, the electronic states are here distributed in a lower energetic valence band and a higher energetic conduction band with a band gap between them. The width of this gap is often called mobility gap energy. In the OJL model, the respective distributions of electronic states $N_v(E)$ and $N_c(E)$ have the basic form of $\sqrt{\pm E}$, where E is the state energy. However, there is no well-ordered far field structure in the amorphous case, meaning that electronic states encroach into the otherwise forbidden region of the band gap. This behaviour is modelled by using declining exponential equations for the density of states that trace into the band gap.

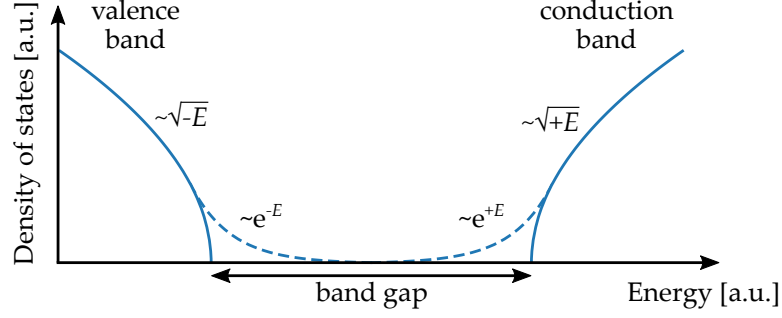


FIGURE 5.4: Depiction of the density of electronic states in an amorphous semiconductor as described by the OJL model.

The OJL model is modified for Scout by adding a decay term. It consists of multiplying the distributions of both bands with another exponential function to let the density of states reduce down to zero at high energies. This is not only sensible in a physical meaning as there should be no states at infinitely high energies, but it is also required for the later calculation of the dielectric function of the material.

As the next step, the so called joint density of states $J(E_p)$ is calculated, which is given by

$$J(E_p) = \int_{-\infty}^{+\infty} N_c(E)N_v(E - E_p)dE. \quad (5.1)$$

This describes the combination of the state densities of the valence and conduction band at an energy distance of E_p or, in other words, how big the overlap is between the state densities of each band at an energy distance of E_p . Therefore, the joint density of states expresses the average possibility that electrons can transfer from the valence into the conduction band if an energy of E_p is provided. As a consequence, $J(E_p)$ is proportional to the imaginary part of the portion of the electric susceptibility that originates from the OJL model (χ_{OJL}). It describes the probability that a photon of energy E_p is absorbed and is a part of the complex dielectric function characterising the modelled material. Since the OJL model was modified by the decay term, the real part of χ_{OJL} can now be calculated by exploiting the Kramers-Kronig relations [Luc05].

The possibility of high energy interband transitions still needs to be contemplated. Although these may occur outside of the considered energy or wavelength region of the to-be-reproduced transmission spectra, they still influence the passing electromagnetic waves at lower energies or higher wavelengths. In our Scout model, these are approximated by an harmonic oscillator with a transition energy corresponding to a wavelength in the ultraviolet range at about 166.7 nm. This may not be a correct description of the band structure near the transition energy, but at much lower energies it is an accurate approximation [Erm84]. The ultraviolet oscillator provides a susceptibility χ_{UV} that only has a real contribution at energies below its transition energy.

The relative, complex-valued dielectric function ϵ_r of the modelled material is now complete and can be expressed by adding the contributing susceptibilities:

$$\epsilon_r = \epsilon' + i\epsilon'' = \chi_{\text{vac}} + \chi_{\text{OJL}} + \chi_{\text{UV}} = 1 + \chi_{\text{OJL}} + \chi_{\text{UV}}. \quad (5.2)$$

Here, $\chi_{\text{vac}} = 1$ is the susceptibility of the vacuum. According to the definition derived from the Maxwell equations, the complex refractive index n stands in relation to the dielectric function and the relative magnetic permeability μ_r by

$$n^2 = \epsilon_r \mu_r. \quad (5.3)$$

As the magnetic permeability is usually close to 1 in optical applications, its influence can be neglected and the complex refractive index of the modelled material can be calculated. By doing that, the real and imaginary parts of the dielectric function get mixed in the real and imaginary parts of the complex refractive index:

$$n^2 = (n + ik)^2 = \epsilon' + i\epsilon'' = \epsilon_r \quad (5.4)$$

$$\Rightarrow n^2 = \frac{1}{2} \left(\sqrt{\epsilon'^2 + \epsilon''^2} + \epsilon' \right), \quad (5.5)$$

$$k^2 = \frac{1}{2} \left(\sqrt{\epsilon'^2 + \epsilon''^2} - \epsilon' \right). \quad (5.6)$$

The optical properties of a material are fully represented by the wavelength dependent refractive index n and extinction coefficient k . The silica substrates, which were used at the deposition of the aSi layers, were modelled from their transmission spectra by independently fitting them to their respective measurements shown in figure 5.3. In combination with these models, Scout is able to accurately simulate the transmission spectrum of a layer of the modelled semiconductor material on either one of the used substrates. Interference effects, that might occur in the thin layer, are addressed in the simulation just as reflections and absorptions. However, unlike the mirrors utilised in GWDs, the in Hamburg deposited aSi layers had an not negligible amount of scattering losses. These were taken into account in the simulated transmission spectra by the addition of a new virtual layer. It reduces the scatter-free power transmission coefficient T_i to

$$T_{i,\text{scatter}} = T_i C_1 \exp \left(-\frac{1}{\lambda^2 C_2^2} \right). \quad (5.7)$$

Here, C_1 and C_2 are constants that respectively describe the behaviour of the scattering independent and dependent on the wavelength λ . If no scattering is present in a sample, the first constant would take the value of $C_1 = 1$, while the second constant would approach infinity. In practise, it is sufficient enough for C_2 to take on a value of $C_2 > 25/\lambda_{\text{min}}$, where λ_{min} is the minimum wavelength within the considered spectrum.

All described model parameters are of variable strength or intensity. By fitting the simulated spectrum to a measured one, it is possible to derive several properties of that sample.

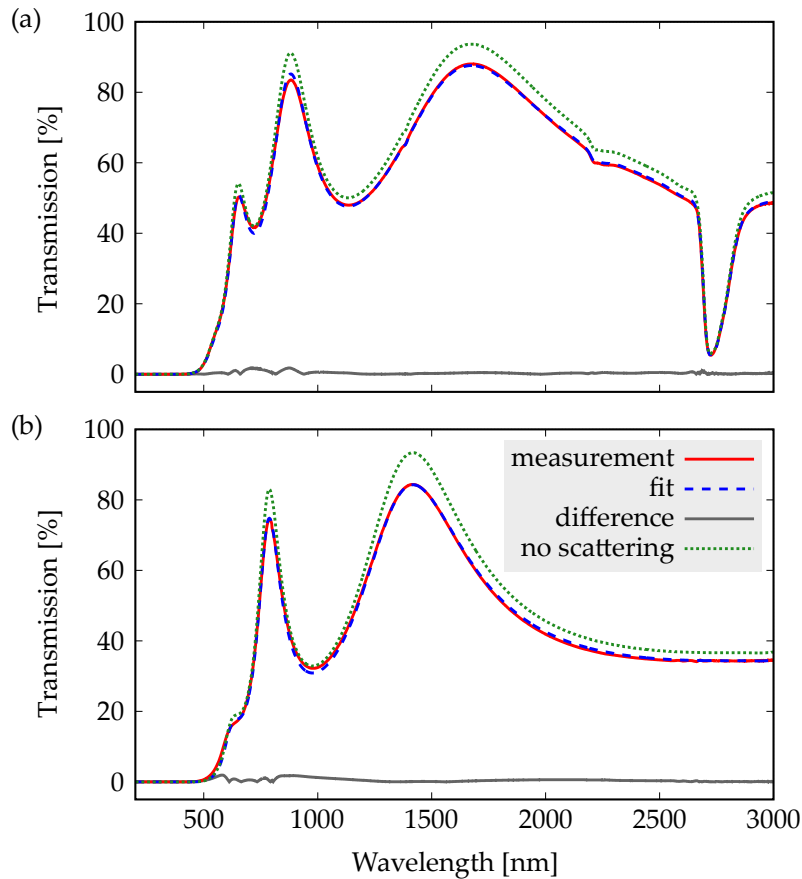


FIGURE 5.5: Examples of Scout fits compared to the measured transmission spectra of the PLD deposited aSi coatings. Shown are the measurements of the coatings F1 (a) and T3 (b), their fits by Scout, the difference between both and how the transmission spectra would look like if no scattering would be present.

Two examples of this are shown in figure 5.5. Depicted are the transmission spectra of the coating F1 (a) deposited on C7980 and the coating T3 (b), which was deposited on C7979. The differences between the measurements and fits are shown as well as the theoretical transmission spectra if there was no scattering present in these samples. The deviations of the fits shown in these example measurements are of medium strength and some fits deviate a lot less than that with a few fits even being nearly indistinguishable from their respective measurements.

The most important coating properties to derive from the Scout model for my analysis were the layer thicknesses of the aSi, its mobility gap energy, the wavelength dependent refractive index and the scattering. Literature shows a relative good agreement of measured layer thicknesses and mobility gap energies to their respective values from a fitted Scout model [EA16, Mus18, Sol10]. In combination with the small deviations of the fits which indicate valid refractive indices and scattering values, I deduce that all coating properties are accurately represented by the simulation.

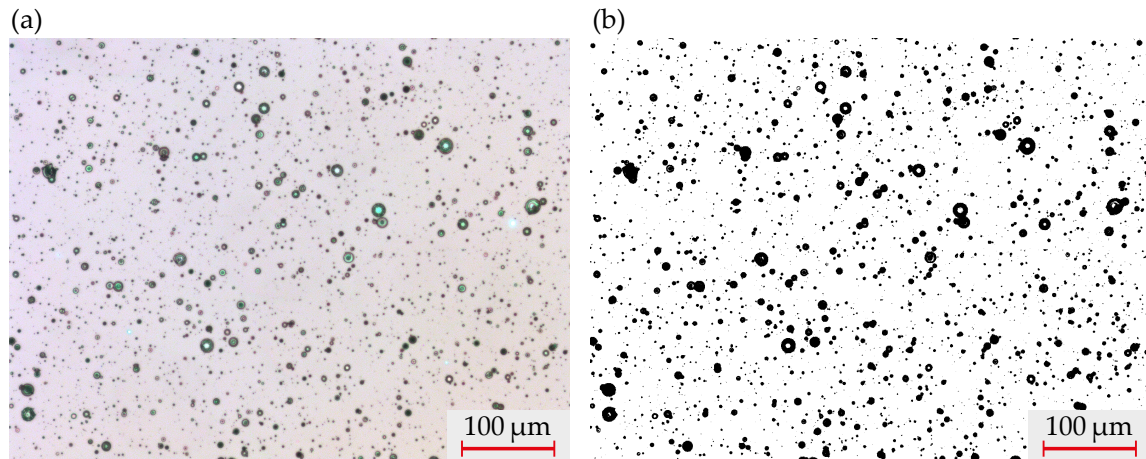


FIGURE 5.6: Example of a microscopic image of a PLD produced aSi layer and its processing. Shown is the coating T1 in altered colours (a) and the processed image by ImageJ (b). The crystallisation was here of medium strength with a total area covered by microcrystals of about 9.7%.

5.2.2 Examination of Microscopic Images

There were microscopic silicon crystals present in the coating of every PLD produced sample. These were investigated by microscopic imaging of their surfaces. For that, I used a *DM4000 M* microscope produced by *Leica Microsystems*. The images show an area of about $0.6 \times 0.45 \text{ mm}^2$ at the centre of each coating. As an example, the microscopic image of the coating T1 is depicted in figure 5.6 (a). The shown colours are altered by the application of an whitening balance to increase the contrast between the bright amorphous background and the darker microcrystals that are clearly visible.

We examined the microscopic images using the program *ImageJ* released by the *National Institutes of Health (NIH)* of the USA. In the first step, the colours were removed from the images. Afterwards the contrast was highly increased to create images of solely pure black and pure white colour. By adjusting the threshold between the dark and bright parts, it was possible to blacken the crystals and whitening the background as is depicted by figure 5.6 (b). The amount of crystals and their size could now be determined by counting the individual areas of joint black pixels using *ImageJ*. As a result, we obtained the number of pixels in the image area and their average size from which we calculated the portion of each coating, that is covered by the crystals.

5.3 Analysis Results

In this section, I present the results from my analysis of the PLD produced aSi coated silica samples. I checked the correlations between the different deposition parameters of the coating series with the properties I gained from the analysing methods described in the previous section. The focus of my analysis was on the impact the different parameters had on the optical absorption of the aSi as that is the main concern for its implementation in coatings for GWDs. The motivation is that the absorption is currently still too high for

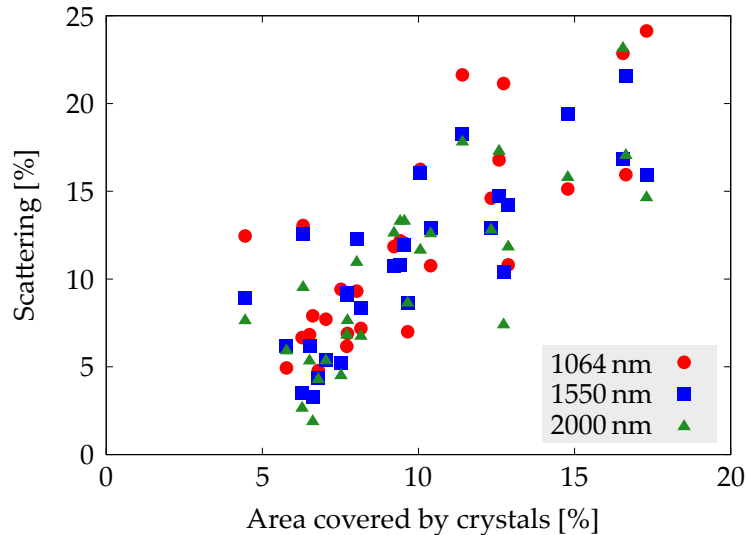


FIGURE 5.7: Scattering of the PLD produced aSi layers at various wavelengths as a function of the area portion covered by the microscopic crystals.

a classical two-material HR coating, but multi-material coatings are already feasible. A further reduction in absorption would allow to utilise aSi in more coating layers resulting in a significantly reduced thermal noise (see chapter 3).

The examination of the first three deposition series was already published in my first author paper [Ter20]. This part is therefore taken over and build upon. A complete list of deposited aSi coatings including their defining deposition parameters and their, for the analysis in this section most important coating properties, can be found in appendix B.

5.3.1 Microscopic Crystals

In the first three deposition series, the portion of the coating area that is covered by microscopic crystals varied between about 4.5 % and 12.9 % with an uncorrelated average size from about $7.4 \mu\text{m}^2$ to $26.4 \mu\text{m}^2$. The last deposited background-gas series showed an in general stronger crystallisation compared to the first three series with a covered area from about 9.2 % to 17.3 % and an average size between $16.9 \mu\text{m}^2$ and $30.4 \mu\text{m}^2$.

In all four series, I could not find any correlation between the varied deposition parameters and the amount of microscopic crystals, their average size or the covered coating area. The amount and size of crystals appeared to be random. There was also no correlation with the other coating properties investigated, namely the extinction coefficient, the refractive index or the mobility gap energy. Only the scattering was affected by the crystallisation. This is shown in figure 5.7. Depicted is the scattering according to the Scout fits at different contemplated wavelengths in relation to the crystallised area for all coatings of the four analysed series. Although there is a big spread in the amount of scattering at a given crystallisation, the expected trend of a higher crystal-covered coating area leading to a greater amount of scattering is clearly visible. The spread indicates, that there are further mechanisms influencing the scattering.

However, two of the disregarded coatings showed an increased amount of crystallisation with a covered area of about 17% and 23%. They had an unusual high absorption with an extinction coefficient that was up to seven times higher than for comparable samples. Since this connection did not show in the other coatings and as the higher absorbing sample of these two even was the less crystallized one, I conclude that the high portion of covered crystals is not the origin of the elevated absorption but rather another symptom of its cause, which in these cases probably was connected with the too small ablation areas. This hypothesis is also supported by the background-gas series that had samples with a comparable level of crystallisation. Although these samples had a partly elevated absorption (see figure 5.8(e) and (f)), the increase was significantly smaller than that of the disregarded samples. The other samples in the series, which were in parts only slightly less crystallised, also did not show any connection of their properties to the crystallisation.

In conclusion, the crystallisation increases the unwanted scattering of the samples but it does not seem to affect the other coating properties or impede on their investigations. An unusual high crystallisation however might indicate a problematic layer deposition which could lead to significantly altered coating properties as especially an increased optical absorption. Therefore, the amount of microscopic crystals can mostly be ignored in the further analysis and only high crystallised samples need to be noted.

5.3.2 Deposition Parameters

In the first coating deposition series, the laser pulse energy was varied between 400 mJ and 850 mJ at a pulse repetition rate of 10 Hz. For the second series, the repetition rate was altered from 5 Hz up to 50 Hz using a pulse energy of 550 mJ. During these first two deposition series, the substrate was held at room temperature and no buffer gas was flowing into the deposition chamber. In the third series, the substrate was heated to varying temperatures, from room temperature up to 500°C. The pulse energy and its repetition rate were held constant at 550 mJ and 15 Hz respectively and there was again no gas flow present. Finally, in the last deposition series, the gas flow was increased from zero up to 8.4 SLM (standard litre per minute). The pulse energy and its repetition rate was again at 550 mJ and 15 Hz, while the substrate heating was absent again.

The influence of all four systematically varied deposition parameters on the optical absorption of the aSi layers is depicted in figure 5.8. Shown is the extinction coefficient k at different wavelengths as a function of each respective parameter. The red, diamond-shaped points mark the coatings which either experienced slight irregularities in their deposition process or show an unusual high crystallisation which might indicate the presence of other, hidden deviations from the usual deposition parameters (see subsection 5.3.1). These irregularities might have affected the coating material properties in a way which could make the systematic comparison to the remaining layers problematic. However, there was not enough evidence to justify the immediate exclusion of these layers from my analysis. From now on throughout this chapter, the highlighting of these samples is kept.

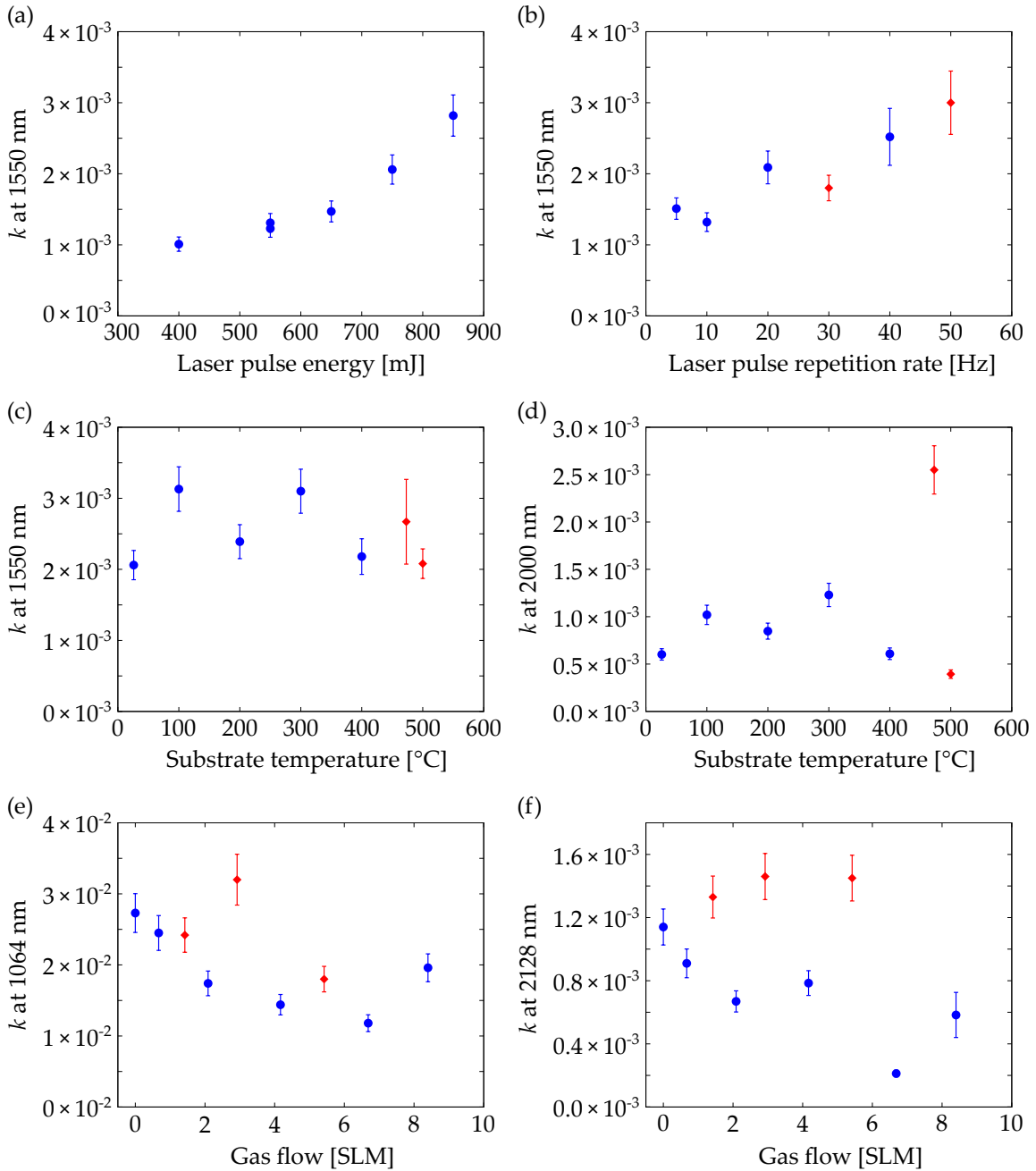


FIGURE 5.8: The extinction coefficient k of the produced aSi layers as a function of the varied deposition parameters at wavelengths of 1064 nm, 1550 nm, 2000 nm or 2128 nm. The red diamonds depict layers which either had irregularities in their respective deposition processes or showed an unusual high crystallisation.

Over all regarded samples, the values found for k at a wavelength of 1550 nm range from 1.0×10^{-3} to 3.1×10^{-3} and are therefore in the same order of magnitude than was previously found for other aSi layers that were not heat treated [Bir18, Ste18b]. Figure 5.8(a) clearly shows an increasing trend of k with the laser pulse energy. There were two coatings deposited at 550 mJ to test the reproducibility. The difference in k between these two coatings amounts to about 6.1 % and is as that well below each measurement uncertainty.

Figure 5.8(b) shows the dependency of k on the laser pulse repetition rate. As in the pulse-energy series, an increasing trend of k can be seen, though not as clear and strong. In addition, two of the measured points are marked for irregularities during the deposition. The aSi layer deposited at 30 Hz (F4) experienced a strong pressure rise from about 10^{-5} mbar to about 0.4 mbar during its deposition which resulted in a thinner than expected coating. It is unclear if or how other coating parameters were affected by this anomaly. During the deposition of the 50 Hz sample (F6), the laser beam might have hit the clamp holding the target and subsequently ablated some of its material, contaminating the produced aSi layer. In other samples this has led to a significant increase in absorption and although the coating F6 follows the discovered trend, it is still not certain if there was a slight contamination. This point should therefore be considered with care.

The absorption of the substrate-temperature series is depicted in figure 5.8(c) and (d) at wavelengths of 1550 nm and 2000 nm respectively. Other than in the first two series, no trend can be determined as k appears to be roughly constant or even oscillating, especially at 1550 nm. There are two points marked with red diamonds which resemble the coatings T6 and T7 deposited at 470°C and 500°C respectively. Both coatings were observed to have an unusual thickness distribution. Their central areas were slightly thinner than the surrounding ring-shaped areas instead of the reverse, which was usually the case. The thickness deviations in general stem from the fact, that the deposition system was originally designed for samples with a size of 1 cm² while we used samples with a diameter of 2.5 cm for handling reasons. The cause of these reversed distributions is unknown. In addition, it seems that the silver foil used to improve the heating efficiency (see subsection 5.1.2) partly melted during the deposition of sample T7 and left some residuals on the substrates backside near the edge. While the absorption of T7 was within the average range at both wavelength, a contamination due to the damaged silver foil cannot be excluded. In contrast to that, sample T6 show a strongly increased absorption at 2000 nm compared to the other layers of this coating series, although there are less indications for an abnormal deposition than for T7. This shows, that there was some deviation which means the absorption measurements at both wavelengths need to be considered with care despite a nondescript absorption at 1550 nm.

The absorption of the final gas-flow series at 1064 nm and 2128 nm is depicted in figure 5.8(e) and (f) respectively. At low gas flow rates up to about 2 SLM (standard litre per minute) there seem to be an decreasing trend of k at both wavelengths. Afterwards, k stays roughly constant at 1064 nm while it might even slightly decreases further at 2128 nm. The three marked samples P3, P5 and P7 deposited at flow rates of 1.4 SLM, 2.9 SLM and

5.4 SLM respectively showed an increased crystallisation, although we used no unusual deposition parameters and also found no irregularities during the coating deposition. The cause of the irregular crystallisation is thus unknown. While at 1064 nm only P5 has a higher than expected absorption, at 2128 nm all three highly crystallised samples show a clear increase compared to the remaining samples of the series. As explained in subsection 5.3.1, the crystallisation is not directly correlated to the absorption, but might indicate problematic layer depositions. Therefore, even if some of the absorption measurements are nondescript, these coatings need to be evaluated with care.

The variation of parameters for the deposition of aSi coatings discussed in this subsection show a significant effect on the optical absorption of the produced layers. This strong influence therefore confirms that the further exploration of deposition parameters is a possible and promising method to reduce the absorption. This could yield in materials that are better suited for mirrors of GWDs.

5.3.3 Deposition Rate

The deposition rate of the aSi coating layers has generally a significant influence on their properties and is therefore an important parameter to consider and to analyse. In previous works, a low deposition rate was speculated to decrease the optical absorption of aSi layers [Bir18]. During the repetition-rate series the deposition rate was directly varied with the frequency at which the pulses were generated as each pulse ablates a comparable amount of material. This should consequently result in a similar varying growth rate. However, the deposition rate was not constant throughout each coating run. The window through which the laser coupled into the vacuum system was to a small extent also coated with aSi during the sample production. We could not impede this unintentional process as it is a direct consequence of the deposition chamber geometry. The coating growing on the vacuum window absorbed an increasing part of the laser power which resulted in a diminishing growth rate as the amount of ablated material slightly decreased with each subsequent laser pulse. Therefore, I calculated the average deposition rate of each aSi layer from its thickness and the total growth time as a measure to compare the different coatings.

The extinction coefficient k at 1550 nm as a function of the average deposition rate is depicted for the repetition-rate series in figure 5.9(a). The maximum deposition rate of about 38 pm/s was reached by the 40 Hz coating while the minimum was only about 10 pm/s for the 5 Hz coating. There is an increase of the growth rate with frequency, which interestingly is not linear in nature, resulting in a decreasing thickness of the aSi layers. That means, the speed of the deposition negatively affects the amount of material that accumulates on the substrate surface. There is an increasing trend of k with the rising deposition rate. If the irregular deposited coatings (red diamonds) are omitted, this trend becomes more clear and in addition, the coatings are sorted by their respective laser pulse repetition rates. The 5 Hz and 10 Hz coatings showed nearly identical absorptions of roughly $k \approx 1.4 \times 10^{-3}$ although there was a large difference in their growth speed. This could

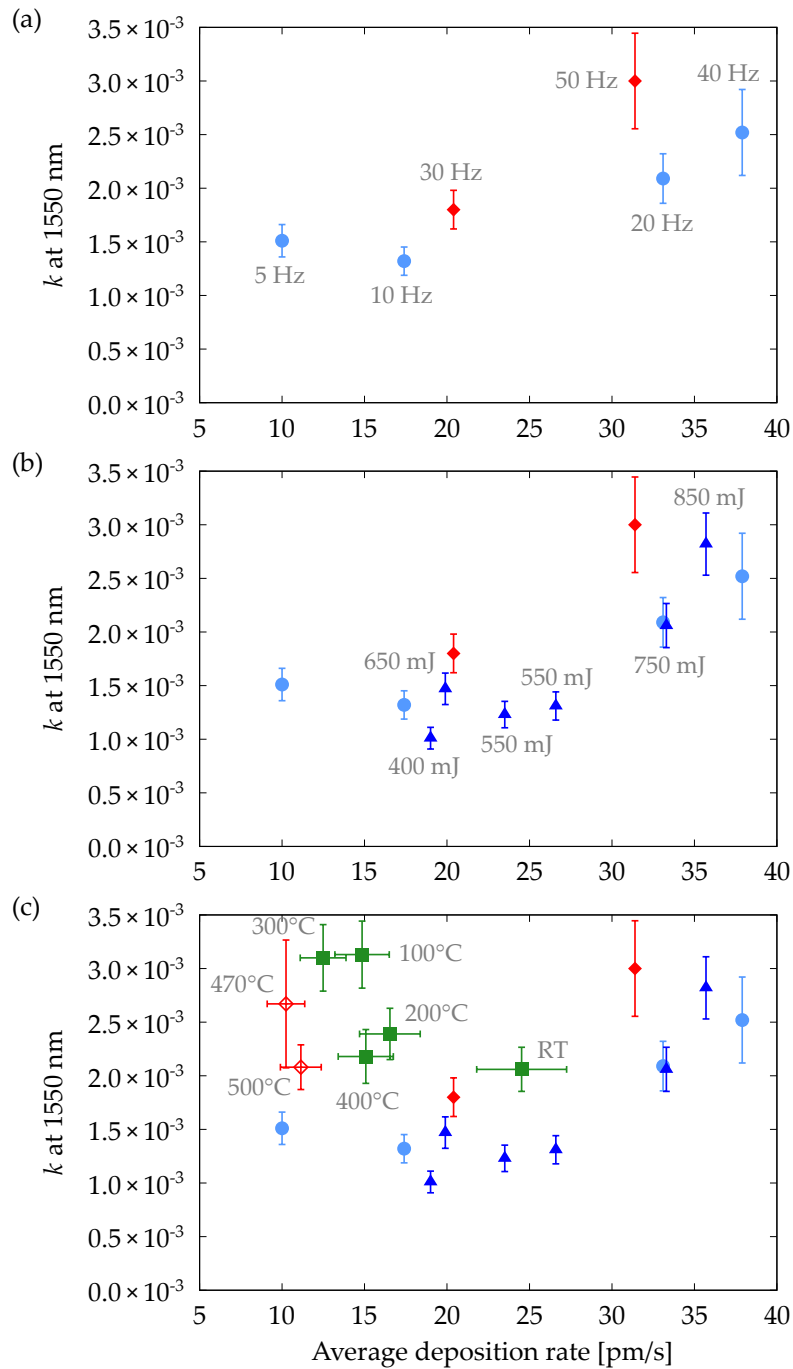


FIGURE 5.9: The extinction coefficient k at 1550 nm of the first three aSi deposition series as a function of the average deposition rate. In (a) only the repetition-rate series is shown. In (b) the pulse-energy series is added. In (c) the temperature series is included. Each point is labelled with its relevant deposition parameter. The labels were added so that the data points can be easily related to the rest of the figures and analysis. The red diamond points depict again the layers which had irregularities in their respective deposition processes.

indicate the existence of a lower limit for k near this value that the absorption cannot fall below by modifying the deposition rate.

The coatings of the pulse-energy series show a clear trend in their absorption as depicted by figure 5.8(a), but their thickness also strongly varies. This is a similar behaviour to the repetition-rate series. Therefore it was of interest to determine if both trends are caused by an increase in growth rate. In figure 5.9(b), k of the pulse-energy series is added to the graph from 5.9(a) to compare both series. The same trend as in the repetition-rate series was observed: an increase of k with the deposition rate. The coatings are also sorted by the used pulse energy during their respective production processes with the exception of the 650 mJ layer. The reasons for that are unknown as I found no irregularities in the deposition or crystallisation. Furthermore, not only the observed trend of both series is similar, but there is also a good quantitative agreement of the observed k values across both series suggesting that the deposition rate is indeed the origin for the varying absorptions in both series. The coatings deposited with relative low pulse energies have little variation in their absorptions with values for k from 1.0×10^{-3} to 1.5×10^{-3} and by that seem to agree with the existence of a lower boundary near this level as presumed before.

The last deposition series for which the absorption was measured at 1550 nm was the temperature series. The data points of the corresponding coatings are added to the previous discussed graph in figure 5.9(c). Since the temperature series was deposited using 200 000 pulses instead of 150 000 as before, their average deposition rates are not directly comparable as the diminishing growth rate with advanced pulse numbers needed to be taken into account. Therefore error bars in x direction were added. The lower ends mark the deposition rates for a continuous growth of the aSi layers over the whole 200 000 pulses while the upper ends mark the case if no additional layer thickness increase occurred after 150 000 pulses.

The coatings of the temperature series have an in general higher absorption at 1550 nm for their respective deposition rates compared to the former two series. Also, the data points are more scattered. Interestingly, the growth rates of the coatings are not sorted by their deposition temperatures but the order seem to be oscillating similar to their absorption. Moreover, there might even be a trend of increasing absorption with decreasing deposition rate if the 470°C and 500°C coatings are discarded. These phenomena show that changing the substrate temperature during deposition has a widely different effect on the coatings than varying the laser pulse energy or repetition rate. The temperature induced changes in absorption are therefore likely caused by another process than what the changing deposition rate is initiating.

The absorption of the temperature series at 2000 nm against the deposition rate is depicted by k in figure 5.10(a). Here, the coating T6, which was deposited at 470°C, was not included in the graph because of its unusually high absorption of $k \approx 2.6 \times 10^{-3}$. There are no measurements of the other coating series to compare at this wavelength, but

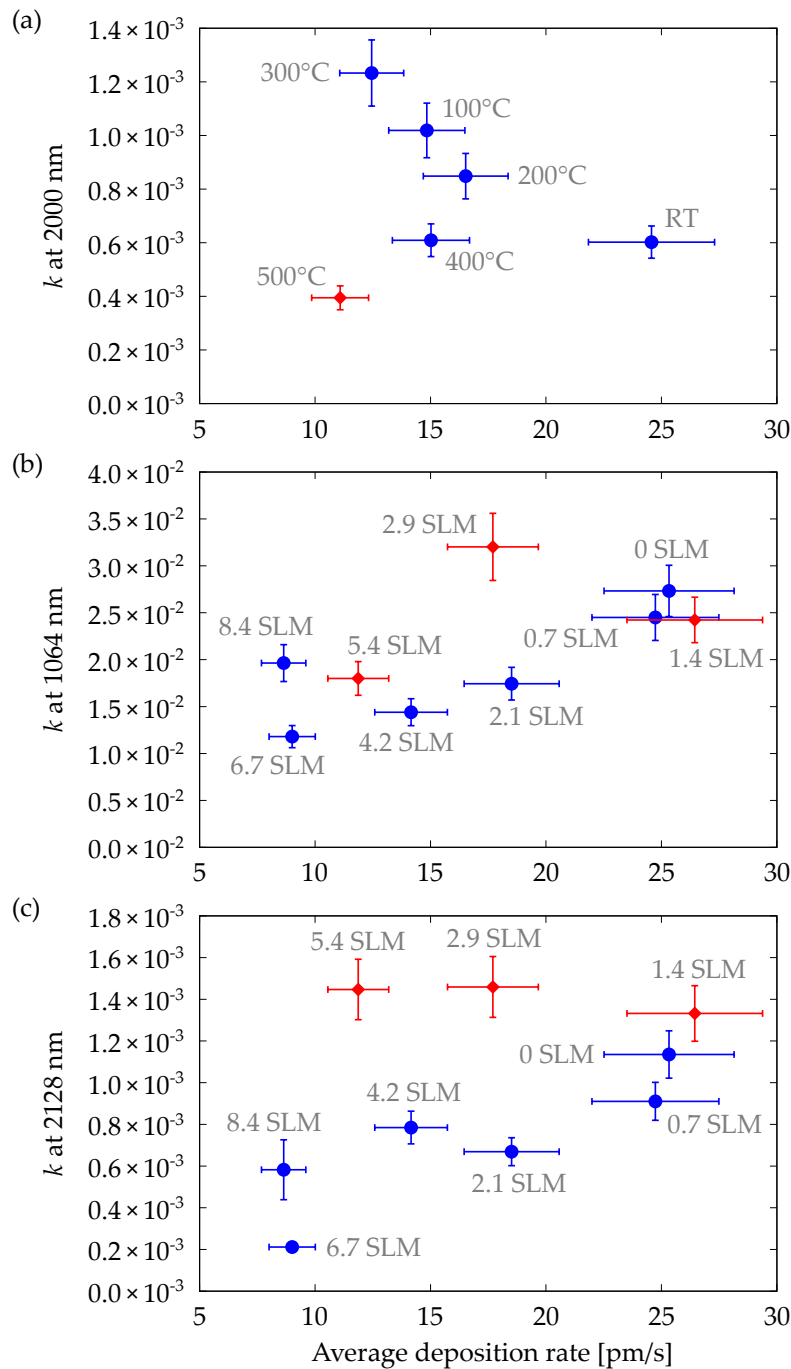


FIGURE 5.10: The extinction coefficient k at varying wavelengths of the temperature series (a) and background-gas series (b and c) as a function of the average deposition rate. Each point is labelled with its relevant deposition parameter. The red diamond points depict the layers which had irregularities in their respective deposition process or were highly crystallised. The coating T6 deposited at about 470°C was not included in graph (a) as it had a very high absorption of $k \approx 2.6 \times 10^{-3}$.

the general distribution of the data points is comparable to the measurement at 1550 nm. The correlation of k and deposition rate is again not clear which also hints at a competing absorption determining process that is not affected by the deposition rate.

The absorption to growth rate interrelation for the gas-flow series is shown in figures 5.10(b) and (c) for wavelengths of 1064 nm and 2128 nm respectively. At 1064 nm, k appears to be positively correlated to the deposition rate, especially if the highly crystallised coatings (red diamonds) are disregarded. At 2128 nm this correlation is less clear but still noticeable without the irregular aSi layers. As a consequence, the observed decrease in absorption with the increasing gas flow rate could be again simply caused by the lowering deposition rates of the aSi layers.

The analysis here shows, that the deposition rate is an important factor that strongly influences the optical absorption of the PLD produced aSi layers. Although there are still some slight inconsistencies or a spread in the absorption data, the deposition rate seems to be the main origin of the changing absorption in the pulse-energy series, the repetition-rate series and gas-flow series. Only the temperature series is in conflict with the found trend and hints at a competing process influencing the absorption.

5.3.4 Refractive Index

The refractive index n is an important property for materials to be used in mirror coatings for GWDs. It determines not only the amount of bilayers a coating has to have for a given reflectivity, but also how thick each layer should be. Both strongly affect the total coating thickness and therefore also the coating thermal noise as described in chapter 3.

The aSi layers produced using PLD had varying refractive indices. This is depicted by figure 5.11. Shown is n at 1550 nm as a function of the different varied deposition parameters for all four analysed coating series. As displayed by figure 5.11(a), the refractive index increases relatively steady with the laser pulse energy from 2.85 to 3.04. Similar to this, n also increases with the pulse repetition rate from 2.80 to 3.11 shown by figure 5.11(b). An exception to this trend is the coating F4 deposited at 30 Hz which experienced a pressure increase during its deposition. These increases in n could stem from a slightly more dense material induced by the rise in deposition rate of the layers. Interestingly, the observed refractive indices of the coatings from both series are quite a bit lower than what can be usually found in the literature with a value of about 3.5 [Pie72]. At other wavelengths, the found trend for n remains, as n almost evenly shifts to slightly higher values at lower wavelengths and correspondingly to slightly lower values at higher wavelengths.

The coatings of the temperature series had a much broader variation of their n compared to the coatings of the pulse-energy series or repetition-rate series as it is shown by figure 5.11(c). While the room temperature coating still had a similar value of $n = 2.97$, it rapidly increased with the rising substrate temperature during the deposition of the aSi. At 100°C, n reaches 3.41 and as that already surpassed all previous coatings by a large margin. The increase then slowed slightly before n reached its maximum and forming a plateau at

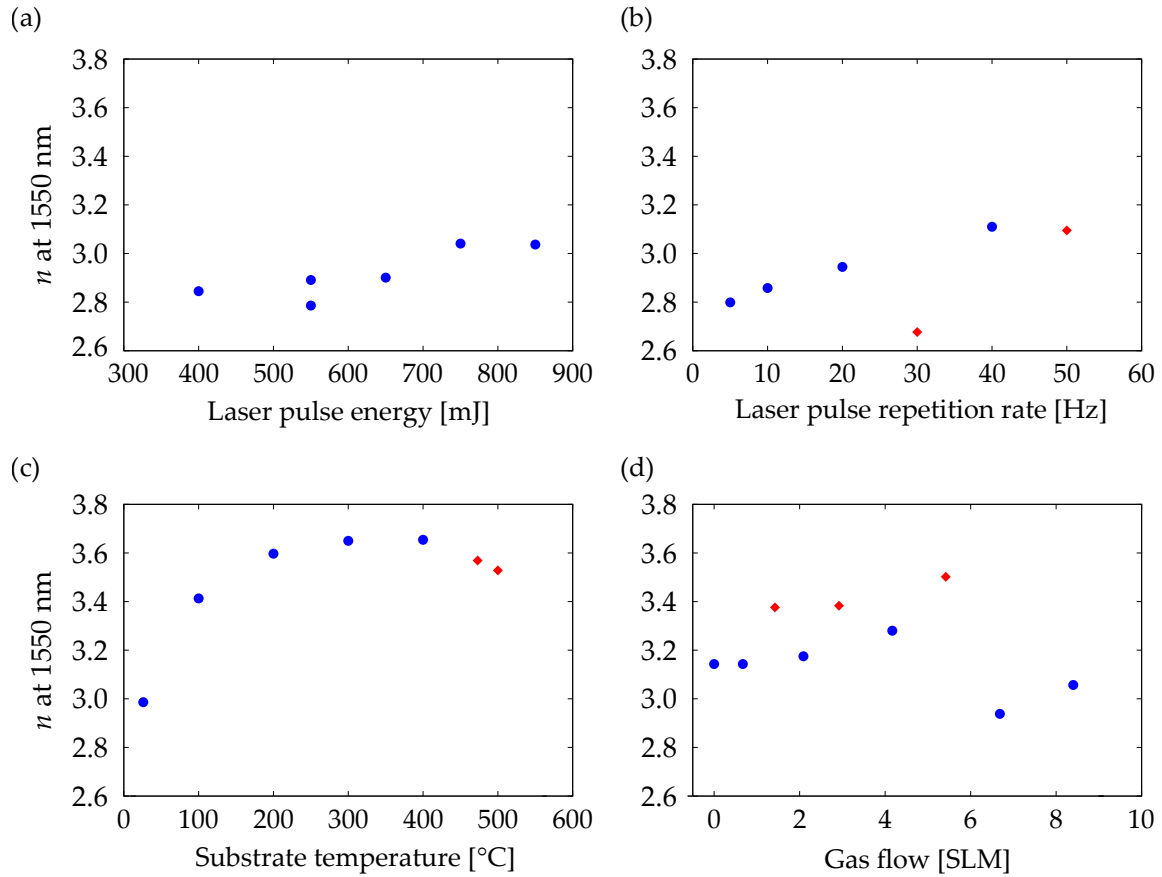


FIGURE 5.11: The refractive index n at 1550 nm of the produced aSi layers as a function of the varied deposition parameters. The red diamond points depict again the layers which either had irregularities in their respective deposition processes or were highly crystallised.

3.65 between 300°C and 400°C. These higher values generally agree much better with the literature, which is also consistent with deposition temperatures commonly being in the 100°C to 200°C range.

At even higher temperatures, we observed a decrease to $n = 3.53$ at 500°C. However, as there were inconsistencies during deposition of the coatings T6 and T7 at 470°C and 500°C respectively, it is unclear if the decrease in n is genuine or just an effect of the changed circumstances during their deposition. Supporting the hypothesis of a genuine change are the observed effects of post deposition heat treatments at different temperatures. Previous work has shown, that a heat treatment of aSi layers lowers the optical absorption and also the mechanical loss till a temperature of about 400°C to 500°C depending on the manufacturer and utilized deposition process. At even higher heat treatment temperatures the properties of aSi worsens again [Bir18, Ste18b], which probably is caused by the starting crystallization of the silicon [Ste16b]. As crystalline silicon has an n of 3.476 at 1550 nm [Li80], the observed reduction in n for amorphous silicon at high deposition temperatures can therefore be explained by the onset of crystallisation. The smooth trend of n for the temperature series with a generally much bigger spread than in the previous two series is another hint to a fundamentally different process being present that is affecting the

coating properties.

The change of n for the gas-flow series is depicted by figure 5.11(d). At first without any artificially inserted gas flow, n starts out a bit higher than comparable coatings of the other series with a value of 3.14. This shows, that there still were some differences in the aSi deposition compared to the previous series and the former state of the PLD setup could not be fully recreated as it was described in subsection 5.1.3. If the highly crystallised coatings depicted by the red diamonds are omitted, it seems that n slowly increases with the gas flow to 3.28 at 4.2SLM. However, the last two coatings P8 and P9 at gas flows of 6.7SLM and 8.4SLM show a big drop in their n to only 2.94 and 3.04 respectively. It is unknown what the cause of this drop is as no further inconsistencies during the deposition of these coatings could be found. Interestingly, the slight increase in n here is not correlated with the average deposition rate in the same way than for the pulse-energy series and repetition-rate series. These experienced an increase of n with the growth rate, while for the gas-flow series the connection seems to be reversed. This might also hint at a another process affecting the coating properties like in the temperature series.

5.3.5 Mobility Gap Energy

The mobility gap energy E_g of aSi coatings (width of their band gap, see subsection 5.2.1) has been studied in previous works. It was observed, that aSi layers with a higher mobility gap energy tending to have a lower optical absorption [Bir18]. Therefore, this correlation was also investigated for the aSi coatings we produced using PLD.

The extinction coefficient k of the pulse-energy series at 1550 nm in dependency of the mobility gap energy is depicted in figure 5.12(a). All coatings are bunched around a value of 1.8 eV while they have a significant spread in absorption. The repetition-rate series is similar in nature as shown by figure 5.12(b). With the exception of coating F4, which experienced a strong pressure rise during deposition, all coatings have a mobility gap energy of about 1.8 eV. Consequently I conclude, that the change in the mobility gap energy of less than $\pm 3\%$ of its mean value cannot be the cause for the strongly varying k of up to a factor of 3. Thus, there has to be another reason for the changing absorption. This nearly identical behaviour of both deposition series is also another indication for both to have a common cause for the observed spread in absorption.

The absorption of the temperature series as a function of the mobility gap energy is depicted in figure 5.12(c) and (d) at wavelengths of 1550 nm and 2000 nm respectively. Unlike the previous two deposition series, the mobility gap energy is spread over a much broader region. At 1550 nm, the same trend as previously observed of a decreasing k for higher gap energies can be seen if the coatings with inconsistent depositions (red diamonds) are omitted. The same is true at 2000 nm although the trend is here slightly less clear. This confirms the mobility gap energy to be one of the underlining mechanisms determining the optical absorption of the deposited aSi.

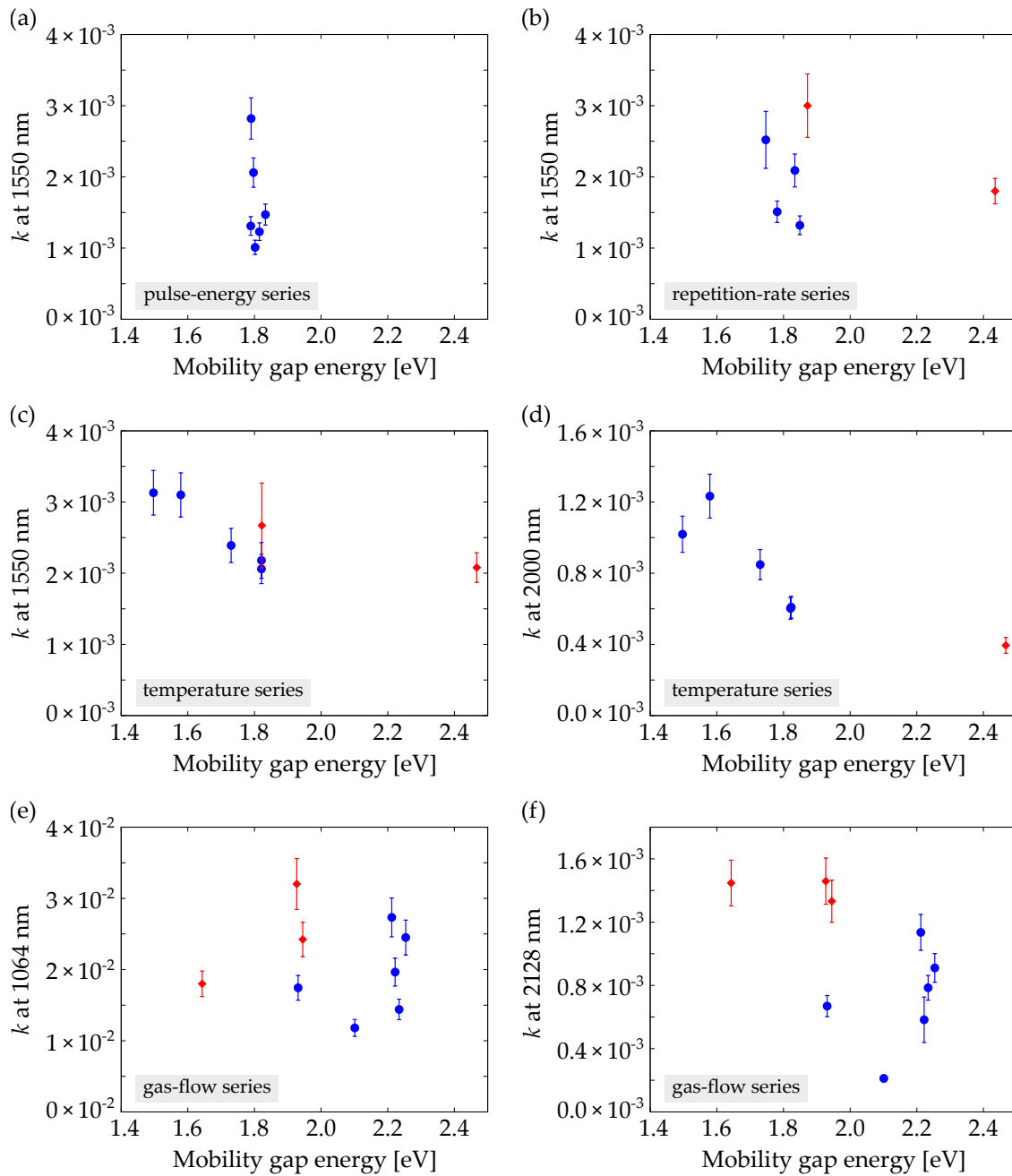


FIGURE 5.12: The extinction coefficient k of the produced aSi layers as a function of their mobility gap energy at wavelengths of 1064 nm, 1550 nm, 2000 nm or 2128 nm. The red diamonds depict layers which either had irregularities in their respective deposition processes or showed an unusual high crystallisation. The coating T6 deposited at about 470°C was not included in graph (d) as it had a very high absorption of $k \approx 2.6 \times 10^{-3}$.

In figure 5.12(e) and (f), k for the coatings of the gas-flow series is shown in dependency of their mobility gap energy. There is no trend to be recognised at either wavelength even if the high crystallised coatings are omitted. The mobility gap energies of the remaining aSi layers are mainly bunched at around 2.2 eV but there is no indication for any systematic process behind this appearance or why some coatings of this series behave differently in this regard.

5.4 Discussion

The aSi coated samples produced using PLD were analysed by various means in the previous section and several conclusions could be drawn:

- The microcrystals seem to have no influence on the coating properties other than on the scattering, but they might indicate the presence of deviations from the normal deposition procedure.
- The deposition parameters had a significant influence on the optical absorption of the resulting thin films and are therefore an important factor to consider and to further explore for the implementation of aSi in mirror coatings.
- The varying deposition rate appears to be the main origin of the change in absorption for the coatings of the pulse-energy series, the repetition-rate series and gas-flow series. Only the samples of the temperature series were not affected in the same way by their deposition rate.
- The refractive index was strongly affected by the substrate temperature during deposition and the observed decrease at high temperatures might be caused by the starting crystallization of the silicon. The influence of the varied parameters on the refractive index in the other deposition series was much smaller in comparison.
- The mobility gap energy barely varied for the pulse-energy series and repetition-rate series. The coatings of the gas-flow series experienced some inconsistent spread but are also mainly bunched together in their mobility gap energy. Only the temperature series showed a noticeable trend in their absorption with the mobility gap energy.

These investigations show, that the mechanisms responsible for changing the coating properties of the pulse-energy series and repetition-rate series are identical since both series showed matching behaviours in all examined features. Furthermore, the same mechanisms seem to be the main reason for the observed property changes in the gas-flow series as these were often similar to the pulse-energy and repetition-rate series. However, the correlations found in the coatings deposited by the temperature series were in contrast to the other series completely different in all aspects. This is a clear indication that the material properties of the deposited aSi were affected by different fundamental means than in the other deposition series.

The absorption processes that are likely determining the observed trends are further discussed in the next subsection. In addition, the possible influence the substrate material had on the coating properties is examined in subsection 5.4.2.

5.4.1 Absorption Mechanisms

Previously, there have been two underlying mechanisms identified that are responsible for the absorption variations observed in aSi layers. First, electronic interband transitions as described for example by the OJL model in subsection 5.2.1 can occur. The strength of the absorption for a given wavelength caused by these transitions is determined by the band structure of the aSi with the extend of its mobility gap energy being the main factor. As a second absorption mechanism, unpaired electrons have been discerned [Jac82, Zan77]. They are also called dangling bonds and are present in the silicon layers as a result of their amorphous structure.

The correlation of the absorption with the mobility gap energy as observed by the temperature series is similar to some findings made in [Bir18]. This trend discloses for the coatings of the temperature series that interband transitions are the dominant absorption mechanism at the contemplated wavelengths. However, although the varying substrate temperature apparently caused a spread in mobility gap energy, no clear correlation between both properties has been observed. Past evaluations of the electronic band structure have shown that the mobility gap energy increases in semiconductors with a decreasing average bond length between the atoms [Gir01]. This results in a higher density of the material which is usually also represented in higher refractive indices. Thus, the irregular mobility gap energies in combination with the smooth trend present in the refractive indices hint at multiple underlying processes being affected by a change in temperature during the deposition process as otherwise correlated trends in booth parameters were to be expected.

A dependency of the absorption on the mobility gap energy was not observed for the coatings deposited in the other three series. The interband transitions are hence unlikely to be the dominating factor determining the absorption in the near infrared for these coatings. Therefore, the variations are likely caused by a changing amount of dangling bonds which consequently are strongly affected by the growth speed of the aSi layers. In addition, the growth rate appears to slightly affect the layer densities as shown by the trends in refractive indices in the pulse-energy series and repetition-rate series.

The incentive of the gas-flow series was to investigate the possible reduction of dangling bonds by binding them with the hydrogen in the background gas and thus reducing the optical absorption. Such a correlation indeed appears to be present in the produced samples with the main influence occurring at low gas flows (see figure 5.8(e) and (f)). However, the observed reduction in absorption could have been solely the result of the changing deposition speed (see figure 5.10(b) and (c) in comparison to figure 5.9(a) and (b)). The influence of the background gas was therefore likely restricted to its physical effects

of slowing down the ablated material prior to its accumulation on the substrate in the deposition process (see subsection 5.1.1). Omitting the irregular coatings, the mobility gap energies of the deposited aSi were generally higher in the gas-flow series than in the first three deposition series. The refractive index was for the majority also higher compared to the pulse-energy series and repetition rate series. Moreover, the refractive index increased with rising gas flow rate while the deposition speed decreased at the same time, which is the opposite trend as found in the other series. Therefore, I conclude that the presence of the background gas overcompensated the influence from the lower growth rate regarding the density of the coating layers.

5.4.2 Influences of the Substrate Material

Two different substrate types were used in the deposition experiments. The first two deposition series utilised C7980 (*Corning 7980 silica*) substrates while the for the later coatings C7979 (*Corning 7979 silica*) substrates were used. The geometry and surface quality of both substrate types were identical. The primary difference of the two material types is the content of residual water and hydroxyl (OH) groups. Their higher amount in the C7980 substrates created distinct absorption peaks which were absent for the C7979 substrates as depicted by figure 5.3.

The coatings of the temperature series (C7979) showed a higher absorption compared to the coatings deposited with similar growth rates of the pulse-energy series and repetition-rate series (both C7980) as shown by figure 5.9(c). At some temperatures, this could be a result of the decrease in mobility gap energy which made the interband transitions the dominant absorption mechanism compared to the dangling bonds, but even for coatings with mobility gap energies corresponding to the other two series, a clear increase in extinction coefficient was measured. The coatings of the gas-flow series were also deposited on C7979 but their absorptions cannot be directly compared to the other series as the measurement wavelengths differed and the states of the deposition system were not exactly identical (see subsection 5.1.3).

The observed behaviour in the temperature series might indicate that the change in substrate material to C7979 negatively affected the absorption of the aSi layers. As the mobility gap energy cannot be solely responsible for the increase, there should be a gain in dangling bonds. In [Bir18], aSi coatings were also deposited on two different substrate materials: C7979 and JGS1 by *Knight Optical*. JGS1 is a fused silica type that is comparable to C7980 in its properties as the amount of water and OH residuals are similar and thus, the transmission spectra are also akin. The dangling bond densities of the aSi layers were measured via electron paramagnetic resonance. The investigation in [Bir18] showed that on the C7979 substrates, the dangling bond densities were generally lower than on the JGS1 substrates. This contradicts the above hypothesis about the dangling bonds being the reason for the higher absorption of the coatings of the temperature series. Furthermore, the measurements in [Bir18] showed a higher absorption for the aSi coatings deposited on C7979 than for the coatings on JGS1 if a similar amount of dangling

bonds was present in both cases. The mobility gap energies should therefore be lower for the C7979 coatings. While this phenomenon, in combination with the deposition temperature, might be partly responsible for the observed reduction of mobility gap energies in some coatings of the temperature series, it still does not explain the higher absorption of coatings on C7979 than on C7980 with similar mobility gap energies.

In summary, there are several indications that the substrate type could influence the quality of the deposited aSi in coatings. However, some of these signs seem to contradict each other and the various correlations can therefore neither be verified nor disputed. A third, competing absorption mechanism next to the dangling bonds and interband transitions might be able to resolve the contradicting trends, but the studies presented here provide no indication about the nature of this theoretical mechanism. Thus, further investigations on this matter and the influence of substrate materials are required.

Chapter 6

Amorphous Silicon and Silica Nano-layer Coatings

6.1 Introduction to Nano-layers

The layers of a multilayered HR coating stack typically have an optical thickness of a quarter of the considered wavelength as described by section 3.1. The concept of nano-layers is that of additionally subdividing these individual quarter wave layers into a number of thinner layers consisting of varying materials. The purpose of this so created substructure is to suppress the possible crystallisation of the coatings during the post deposition heat treatment procedure. This is caused by the lack of concentrated material in the thin nano-layers compared to ordinary quarter wave layers, which is restricting the atoms in their ability to rearrange [How87]. As a result, nano-layers might effectively enable the usage of higher heat treatment temperatures before crystallisation occurs.

In general, heat treatment of coatings is used because it was shown to have a big influence on the optical and mechanical properties of various materials (see also section 3.5). The absorption and mechanical loss is often improved with heat treatment till a certain temperature is reached at which microscopic crystals start to form. These subsequently worsen the material properties again at higher temperatures and in addition strong optical scattering arises due to the many interfaces forming between the crystals and the amorphous material.

There are two motivations for the utilisation of nano-layered coatings. Firstly, higher heat treatment temperatures due to the suppressed crystallisation might allow for further improvements of the optical or mechanical material properties before the crystallisation occurs. Secondly, the optimal heat treatment temperatures vary for different materials. For example, silica is often used as the low refractive index material in HR coatings. The optimal temperature for its heat treatment is about 900°C [Pen10] while most high refractive index materials already start to crystallise at much lower temperatures such as amorphous silicon whose properties start to worsen again at around 450°C [Bir18, Ste16b, Ste18b]. The implementation of nano-layers could help to partly equalise the different optimal heat treatment temperatures or at least enables the faster crystallizing material to

tolerate higher temperatures without a significant deterioration to improve materials like silica. It is therefore an interesting approach for these material combinations.

The rise in crystallisation temperature using nano-layers was successfully shown for a structure made of 19 alternating layers of titanium dioxide (titania) and silica [Pan14]. Each layer was only a few nanometres in thickness and combined they were forming a single quarter wave layer. In comparison to a single layered titania coating, the crystallisation temperature increased by about 50°C.

Optically, a coating layer subdivided into nano-layers behaves like a single, uniform layer, whose refractive index and absorption correspond to the effective refractive index n_{eff} and effective extinction coefficient k_{eff} of the nano-layer structure. The effective values are the respective quadratic averages of the used materials weighted by their thicknesses [Hai06]:

$$n_{\text{eff}} = \sqrt{\frac{n_1^2 d_1 + n_2^2 d_2}{d_1 + d_2}}, \quad (6.1)$$

$$k_{\text{eff}} = \sqrt{\frac{k_1^2 d_1 + k_2^2 d_2}{d_1 + d_2}}. \quad (6.2)$$

Here, n_1 and n_2 are the individual refractive indices of the materials used in the alternating nano-layers, k_1 and k_2 are their respective extinction coefficients and d_1 as well as d_2 are the total thicknesses of the layers made of the same material. The equivalence of both coating structures is shown in figure 6.1 where a nano-layer coating (a) is compared to a generic single layer coating (b). Here, the nano-layered structure consists of 35 thin layers of alternating materials where each individual layer thickness is identical. Light, that is irradiating the structure, is partly transmitted and partly reflected. As a result, its oscillating electromagnetic field is overlaid by a standing wave in reflection of the coating. This is depicted in the figure by the mean electric field intensity (black line) of a light field which wavelength corresponds to the total thickness of the layer stack so that effectively a quarter wave layer is formed. The single layer coating behaves identical to that which means it has equivalent optical properties to the nano-layer stack. Thus, there is no individual interaction of the beam with the thin nano-layers but only with the stack as a whole.

As a possible material for mirrors of GWDs is aSi an interesting candidate due to its potential for a highly reduced coating thermal noise (see subsection 3.5.6). I have investigated a nano-layer stack made of 35 alternating layers of aSi and silica, similar to the coating shown in figure 6.1(a), where the red layers corresponds to the aSi and the blue layers depict the silica. The design thicknesses for all layers were identical at 10 nm. The stack was deposited on several C7980 silica substrates by the company *Tafelmaier Dünnschicht-Technik* using the ion plating deposition method. The coating materials and deposition method are identical to those used for the production of the lower stack presented in [Tai20] and should therefore have the same properties except for their individual thicknesses.

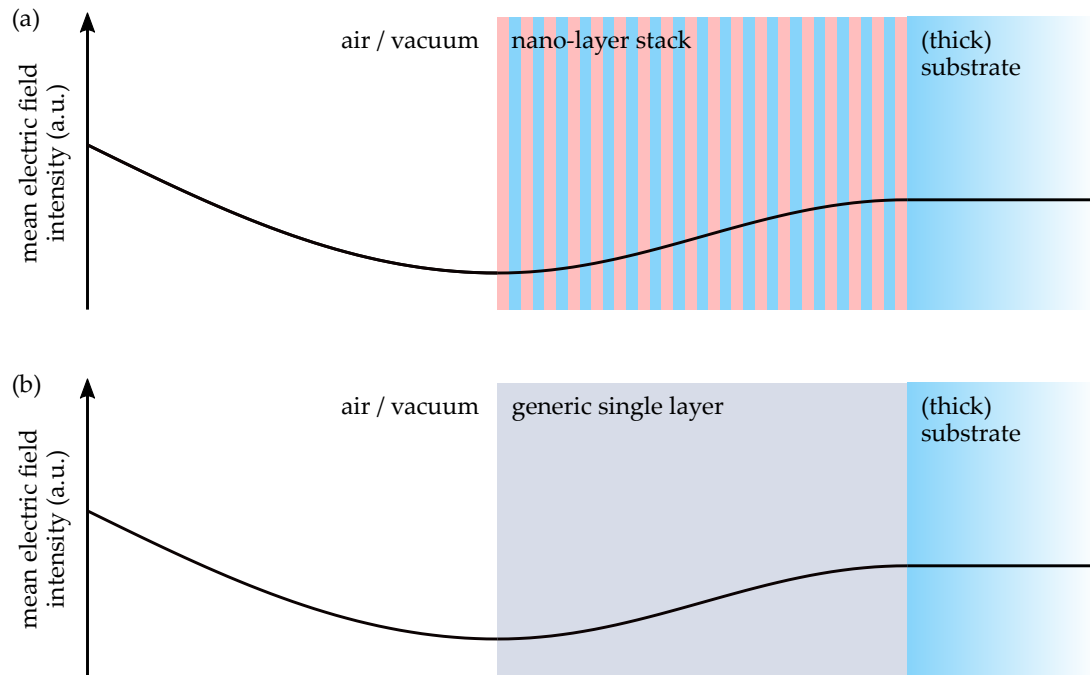


FIGURE 6.1: Schematic depiction of the structure of a nano-layer coating (a) in comparison to a generic single layer coating with equivalent optical properties (b). Here, the nano-layer coating consists of 35 thin single layers of alternating materials and identical thicknesses. In addition, the mean electric field amplitude for an irradiating light wave is shown (black line).

6.2 Characterisation of the Nano-layer Stack

In this section, the results of my investigation about the properties of the deposited aSi-silica nano-layer stack are presented. After deposition, the individual samples were heat treated at nine different temperatures ranging from 100°C up to 700°C. They were then examined by various means: their transmission spectra were taken and analysed, their optical absorption was measured and microscopic images of the coatings were inspected.

6.2.1 Transmission Spectra

I measured the transmission spectra from 200 nm to 3000 nm with a *Cary 5000 UV-Vis-NIR* spectrometer manufactured by *Agilent* and analysed them using *SCOUT*. The nano-layer stack should form an optically homogenous layer as by design both materials, the aSi and silica, should be evenly deposited in layers of regular thicknesses. Therefore, the first model to fit the spectra utilized a single homogenous layer of variable thickness, refractive index and absorption.

The refractive index of an aSi layer can vary significantly as discussed in section 5.3.4. However, the trends which the refractive index follows as a function of the wavelength generally stays identical. A typical curve progression of the refractive index of an aSi layer is exemplary shown in figure 6.2. In contrast, the refractive indices of different (pure) silica types show only very slight variations [Mal65]. As a function of the wavelength, the

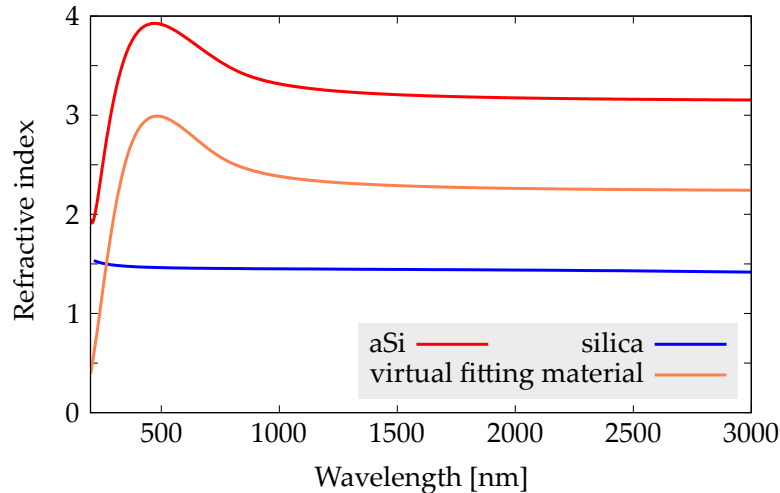


FIGURE 6.2: Refractive indices of aSi, silica and the virtual material used for the fitting of the nano-layer stack heat treated at 100°C as functions of the wavelength.

refractive index of silica is relatively flat with only a slight slope towards higher wavelengths, which is depicted in figure 6.2. Thus, following equation 6.1, the uniform, virtual material used for the fitting of the transmission spectra had to be restricted to have a refractive index with a similar dependency on the wavelength. For this virtual material, the complex, adaptable model described in subsection 5.2.1 was used. By varying the refractive index and absorption within the limits of the model as well as the layer thickness, the simulated transmission spectra were fitted to the measurements. The refractive index of the material fitted to the nano-layer stack heat treated at 100°C is shown as an example in figure 6.2. Please note that, although the utilised model was not designed for fitting nano-layer stacks, the resulting refractive index showed a suitable wavelength dependent behaviour that is describing a mixture of the pure materials. Only at wavelengths below 500 nm, the virtual material is no longer suitable to describe the nano-layer stack. However, the optical absorption of aSi is very high at these wavelengths causing the transmission of the nano-layer stacks being close to zero. The refractive index below 500 nm is therefore practically not affecting the transmission and the influence from an inaccurate refractive index in this region can be neglected.

The transmission spectra of the nano-layer stack heat treated at 100°C, the corresponding fit using a uniform, virtual material and its deviation from the measurement is shown in figure 6.3(a). Due to the restrictions on the refractive index of the virtual material, it was not possible to accurately recreate the measured transmission spectra. There are still significant differences in this example of up to several percent. As the measurement values are in alternation above and below the fit, the differences could only decrease within a single layer model if the refractive index of the uniform layer is allowed to oscillate with the wavelength. As such a behaviour was ruled out beforehand, I conclude that the nano-layer coating cannot be homogeneous in terms of optical thickness of each layer and another model is needed to describe its optical properties.

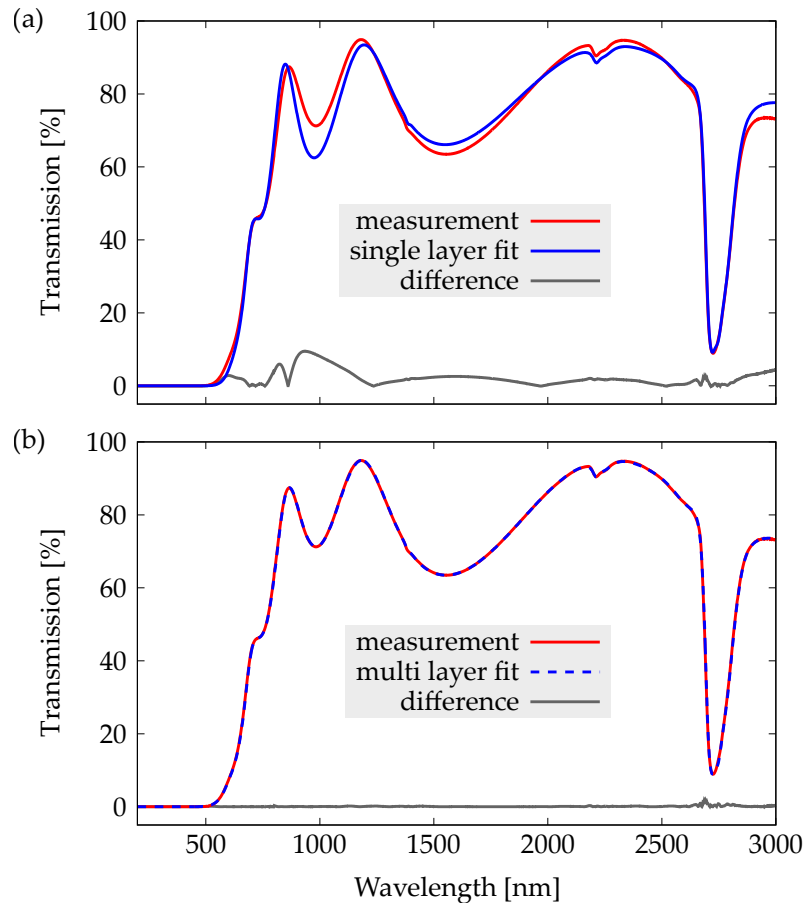


FIGURE 6.3: Examples of the different Scout fits compared to the measured transmission spectra of the heat treated nano-layer stacks. Shown are the measurement of the 100°C sample, its single layer fit (a) or multi layer fit (b) and the difference between the measurement and the respective fit.

The new assumption is that the 35 individual layers the nano-layer stack is composed of create an inhomogeneous optical layer with a varying refractive index within it. To account for that, a complex Scout model was used to fit the transmission spectra. All layers were individually included in the model with the possibility to vary each layer thickness independently. For the optical properties of the silica layers, a model with fixed refractive index and absorption predefined by Scout was used that was found to accurately describe the silica layers produced with the same deposition process discussed in [Tai20]. In case of the aSi layers, the complex, adaptable model described in subsection 5.2.1 was again utilised. This multi layer Scout model therefore allowed the refractive index and absorption of the aSi layers to change collectively, but not individually.

The multi layer fit for the 100°C sample is shown in figure 6.3(b) in comparison to the spectrum measurement. The transmission is nearly perfectly fitted with almost no deviation visible and thus it is accurately represented by the model. The total thickness of the nano-layer stack was about 468 nm with individual layers ranging from 7.4 nm to 18 nm. The aSi made up about 51 % of the total thickness and the remaining 49 % consisted of silica, which resulted in an optical thickness of about 1170 nm. This is a big discrepancy

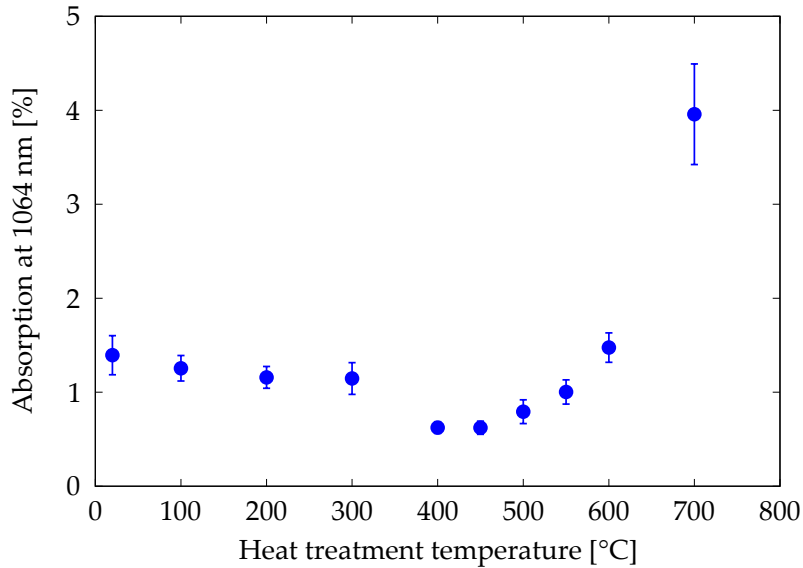


FIGURE 6.4: The total optical absorption at 1064 nm of the nano-layer stack as a function of the heat treatment temperature.

from the expected 350 nm total thickness with individual layer thicknesses of 10 nm, but it is compatible with the claim of the manufacturer that the deposition accuracy for very thin layers is relatively low. Nonetheless, such high deviation from the design is still unexpected. The different samples heat treated at varying temperatures showed the same behaviour in their thicknesses with only small differences. This allows for a direct comparison of the coating properties such as the absorption. However, due to the strong inhomogeneity of the layer stack, it was not meaningful to calculate and investigate the effective refractive index or extinction coefficient.

6.2.2 Optical Absorption

I measured the optical absorption of the nano-layer coatings at 1064 nm by photothermal common-path interferometry using the Hamburg system described in section 4.2. For measurements at 2128 nm, the nano-layer substrates (C7980) were too high absorbing, which concealed the signals of the coatings.

The absorption at 1064 nm as a function of the heat treatment temperature is shown in figure 6.4. After deposition, the nano-layer stack has an absorption of about 1.4%. Up to a heat treatment temperature of 300°C, the absorption only slowly decreases which is analogous to the behaviour observed for stacks of quarter wave layers at 2000 nm discussed in [Tai20]. However, at 1064 nm, the absorption of the quarter wave stack at first increased with heat treatment [Tai21]. At 400°C the absorption of the nano-layers dropped significantly and reached its minimum of about 0.62% at 450°C. This is similar to the quarter wave stack for which the absorption at 1064 nm and 2000 nm was shown to decrease till it reaches a minimum at 500°C. Please note that this stack was only heat treated in 100°C steps and the utilised ovens for the heat treatment differed, possibly introducing a small

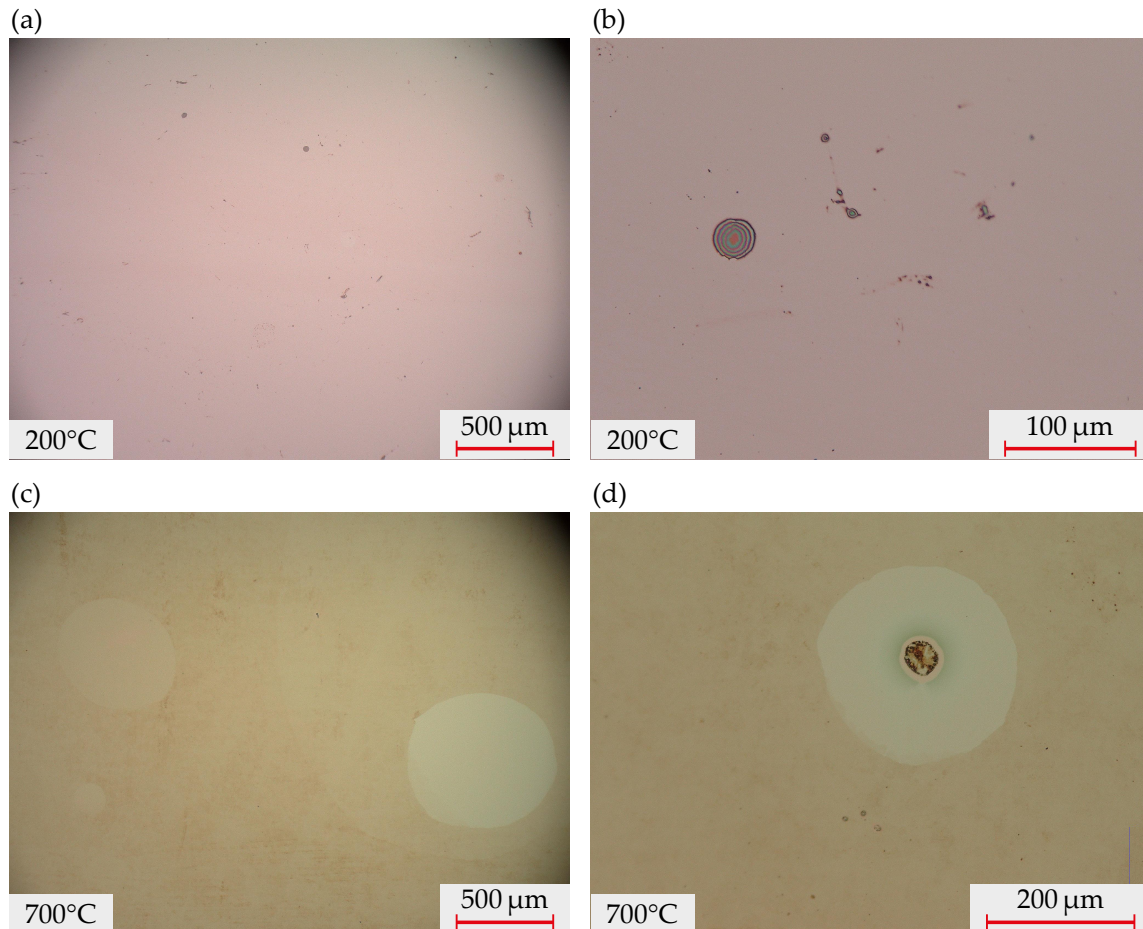


FIGURE 6.5: Examples of microscopic images of the heat treated nano-layer samples. Shown are the 200°C (a), (b) and 700°C (c), (d) coatings at two different magnifications.

offset between the measurements. At even higher heat treatment temperatures, the absorption of both the nano-layer stack at 1064 nm and the quarter wave stack at 2000 nm increased again, while the absorption at higher heat treatment temperatures were not measured at 1064 nm.

6.2.3 Microscopic Images

The surfaces of all nano-layer coatings were examined utilising microscopic images taken by Viola Spagnuolo at Maastricht University. Multiple pictures of varying magnifications were taken of different surface regions for each sample. The areas depicted by the images varied in size from about $0.42 \times 0.32 \text{ mm}^2$ up to $2.8 \times 2.1 \text{ mm}^2$. Some example images are shown in figure 6.5. The coatings that were heat treated up to a temperature of 600°C looked similar to each other. Apart from a small amount of dirt and the occasional scratch or damage on the surfaces, the coatings looked homogenous without any significant differences as it is shown in figure 6.5 (a) and (b). The sample heat treated at a temperature of 700°C looked considerably different though as it is depicted by figure 6.5 (c) and (d). The colour in general was darker and had a greenish tint compared to the other samples. The

surface was also much more inhomogeneous as most regions were blotchy. Interestingly, a few mostly circularly shaped areas remained uniformly. Like in the other coatings, the occasional surface damage was also to be found.

6.3 Discussion and Outlook

The nano-layer stack made of aSi and silica was deposited on silica substrates and subsequently heat treated at varying temperatures. The transmission spectra analysis revealed the coatings to be optically inhomogeneous. By fitting the optical parameters of the individual layers, it was possible to replicate the observed transmission spectrum well.

The total optical absorption of the coatings as a function of heat treatment temperature was investigated. The comparison to a stack made of thicker but otherwise identical layers shows similar behaviours for both cases, but with some deviations from each other, mainly for low heat treatment temperatures at 1064 nm. An increase of the optimal heat treatment temperature, which was previously shown for a titania-silica stack in [Pan14], was not observed. There could be several reasons for that. Firstly, the aSi might not behave in the same way as titania in terms of crystallisation and simply causing the nano-layers to have no influence on the optimal heat treatment temperature. Another reason could be the individual thicknesses of the nano-layers. In the titania-silica stack, the layers were only about 8.5 nm and 4.7 nm thick respectively, while the average layer thickness in the aSi-silica stack was about 13 nm for both materials, which could have been slightly too high to prevent the beginning crystallisation of the aSi during the heat treatment. Moreover, this behaviour might have been further amplified by the uneven material distribution. Therefore, it can not yet be ruled out that nano-layers might have an influence on the optimal heat treatment temperature of aSi in regards to its absorption.

The microscopic images of the coating surfaces did not reveal any significant change till a heat treatment temperature of 600°C although there was already a strong increase in absorption. Only the 700°C sample showed considerable optical differences which was accompanied by an nearly threefold increase in absorption compared to the previous heat treatment step, which is similar to the absorption increase observed in [Ste16b]. Thus, microscopic imagery might be used as an additional investigation method, but it cannot serve to determine appropriate heat treatment temperatures as starting crystallisations are concealed from it.

In short, there are further investigations and depositions of nano-layer stacks needed to be able to accurately evaluate if there are noticeable benefits by using nano-layers for the implementation of aSi in mirrors for GWDs. Especially their influence on the mechanical loss as a function of heat treatment temperature has yet to be considered. The associated measurements at both cryogenic and room temperatures of the here presented nano-layer samples are currently carried out at the University of Glasgow.

Chapter 7

Crystalline Silicon Toplayer

7.1 Concept

The reduction of the mirror coating thermal noise in GWDs is a major objective for the development of novel coatings. Considerable improvements are only viable by implementing new materials with improved properties in the HR coatings of the GWD test masses (see section 3.3). There are a multitude of different materials currently considered for the alternating high and low refractive index layers with various advantages and disadvantages (see section 3.5).

A material which would be excellently suited as a high index material is crystalline silicon (cSi). It possesses not only an exceptionally low mechanical loss [McG78, Naw08], but also a very low optical absorption [Deg13, Kee95] which can practically be neglected for thin layers with a maximum thickness of up to a few hundred nanometres. In addition, the refractive index of cSi is relatively high with a value between 3.42 and 3.48 in the relevant wavelength regions depending also on the temperature [Li80] which would result in thin individual layers, reducing the coating thermal noise even further. However, as a crystalline material cSi cannot be as easily implemented in HR coatings as, for example, amorphous materials. To be able to deposit silicon on a surface so that a monocrystalline layer grows, it needs to be also monocrystalline with a similar lattice structure than cSi. Otherwise, silicon would form polycrystalline or even amorphous layers. Coatings including polycrystalline layers are not suitable for GWDs as the various crystal orientations would cause a high scattering of the light while aSi layers have vastly different properties (see section 5.3). However, there was not yet a suitable crystalline material with a relatively low refractive index and matching lattice structure found to partner cSi in HR mirror coatings.

In [Ste16a], a coating design and manufacturing process was proposed that potentially enables the utilisation of a single cSi layer on the very top of an otherwise amorphous layer stack. This toplayer was calculated to significantly reduce the optical absorption of an example coating by about 44 % with an reduced thermal noise by about 8 % at the same time. This was achieved by reducing the number of silica-tantala bilayers in favour for a bilayer made of the cSi toplayer and silica.

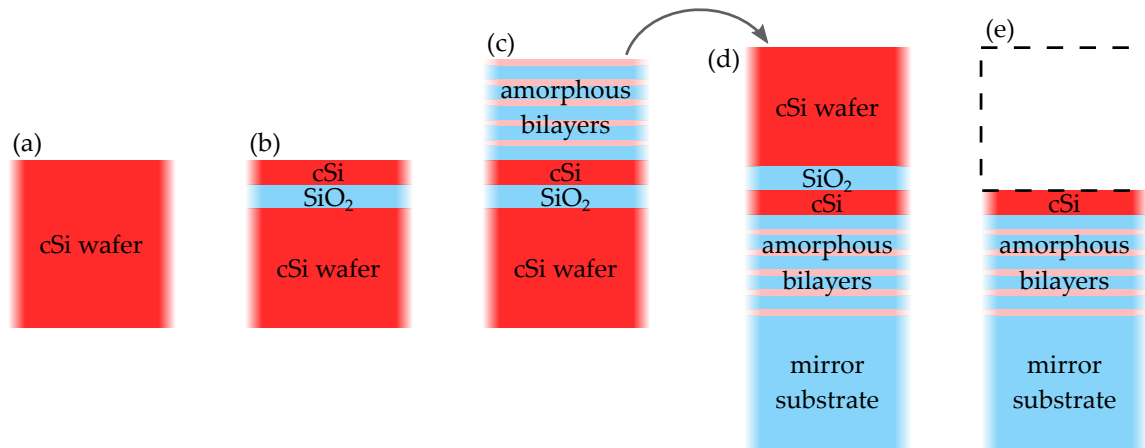


FIGURE 7.1: Schematic depiction of the production process to implement a cSi layer on top of an amorphous layer stack. The basis is a cSi wafer (a), which is then processed to form a SOI wafer (b). The amorphous layer stack is deposited on top of the SOI wafer (c) and subsequently bonded upside down on the mirror substrate (d). In the end, the bulk silicon and silica insulator layer are removed using first mechanical ablation techniques and later etching solutions (e).

7.2 Sample Production Process

The cSi layer cannot be added on top of an amorphous layer stack by the usual deposition techniques. A more complex production process is therefore needed which is schematically depicted in figure 7.1. The basis for this process is an ordinary silicon wafer (a), which is then used to produce a so called silicon on insulator (SOI) wafer (b). There are two different methods currently used to manufacture SOI layers: the separation by implantation of oxygen (SIMOX) method [Nak93] and the wafer bonding method [Oha86]. SIMOX utilises an oxygen ion beam to implant an oxygen rich layer below the surface of the cSi wafer. By heat treating the wafer at high temperatures of more than 1000°C, the oxygen reacts with the silicon in its vicinity and the silica layer is formed, resulting in a SOI wafer. For the wafer bonding method, a cSi wafer is first oxidised on its surface forming the silica layer and subsequently bonded to a second cSi wafer. The redundant material of the original wafer is then removed, so that only a thin cSi layer on top remains, creating the SOI wafer. Different types of SOI wafers with varying individual layer thicknesses are commercially available as their production is a standard procedure in the semiconductor industry.

The amorphous layer stack is deposited on top of the SOI wafer using regular deposition methods (c). The coated wafer is then bonded upside down, meaning the coated side facing the substrate, to the prospective mirror substrate (d). In the final step, the bulk silicon and insulating silica layer of the SOI wafer are removed (e). For that a combination of mechanical ablation processes like lapping and etching solutions can be utilised. The mechanical ablation is used for a swift reduction of the bulk cSi thickness to reduce the processing time while the etching ensures a clean removal of the unwanted layers without damaging the coating stack below.

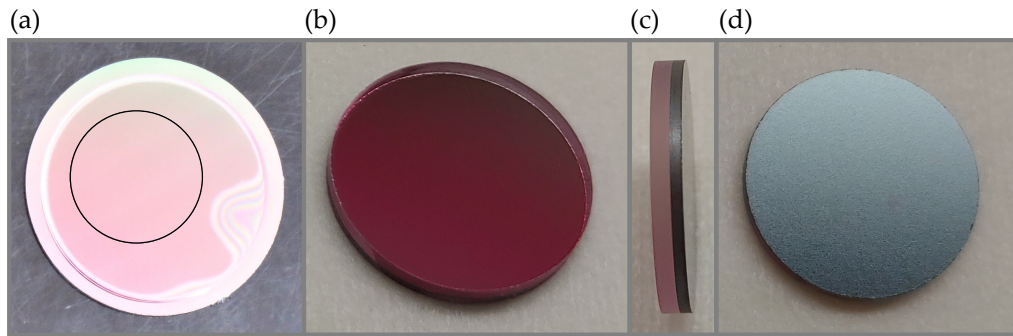


FIGURE 7.2: Example photos of a bonded prototype cSi toplayer sample. Shown is the sample after bonding the SOI wafer to the silica substrate (a). The white wave-like lines to the right and bottom of the sample are bonding defects. The black circle depicts the future cut out of the sample. Further shown is the sample after the cutting process with the silica part on top (b), from the side (c) and with the silicon part on top (d). The different colours in (a) and (b) stem from varying lighting conditions.

7.3 Prototype Samples

For the first time, several prototype samples were produced and investigated to test the proposed bonding and etching processes. Their basis was a commercial SOI wafer that had a bulk thickness of $675\ \mu\text{m}$ with a $3\ \mu\text{m}$ silica layer separating a $220\ \text{nm}$ thick crystalline layer. The wafer was cut into multiple samples with $29\ \text{mm}$ diameter by an industrial laser cutting machine by a mechanical workshop of the University of Hamburg. There was no amorphous layer stack deposited on top of the samples for this first test. Instead, the samples were directly bonded with the thin cSi layer side to fused silica substrates (C7979) of $25\ \text{mm}$ diameter. This was carried out by the *Fraunhofer Institute for Applied Optics and Precision Engineering* using a plasma activated bond technique.

The bonding result is exemplarily shown in figure 7.2(a). The smaller silica substrate can clearly be distinguished on top of the larger SOI wafer. The white wave-like lines to the right and at the bottom of the sample are defects produced during the bonding process. These stem from deviations in the surface flatness of the silica substrate and SOI wafer and were present in varying degrees in all bonded samples. The example displayed here showed a medium amount of defects. To receive defect free samples for further processing steps, smaller pieces with $15\ \text{mm}$ diameter were cut out from the bonded samples, which is implied by the black circle in figure 7.2(a). Example photos of a cut-out sample are also shown in figure 7.2 with the silica part on top (b), from the sample side (c) and with the silicon (thick wafer) part on top (d). The different colours displayed in (a) and (b) are caused by varying lighting conditions and not from physical differences of the sample itself.

I investigated the etching process on the SOI wafer by conducting a multitude of etching tests, first with various fragments and remaining cut-outs of different SOI wafers and later with the rest pieces from the cutting of the bonded samples. For the etching, an aqueous solution of 20 % potassium hydroxide (KOH) was used at temperatures varying

from 30°C to 42°C. For all etching experiments, the respective containers were placed in a heated sand bath to ensure an evenly heat distribution. The general etching process of cSi and silica using KOH solutions at different temperatures were already thoroughly studied in the past [Sei90]. The etching rate of cSi depends not only on the temperature and concentration of the solution, but also on the crystal orientation. The cSi of the SOI wafers used for the etching tests and prototype samples had an $\langle 100 \rangle$ orientation. Therefore, the expected etching rates for the conducted experiments were between 3.4 $\mu\text{m}/\text{h}$ and about 8 $\mu\text{m}/\text{h}$. As the etching speed of silica is up to 2000 times lower than that of cSi at the used temperatures, the thin silica layer of the SOI wafer should act as a buffer layer which stops the etching process.

The first etching test was conducted with pieces of a SOI wafer over 96 h in open top beakers. Both sides of the SOI wafer were equally exposed to the etching solution, but once the thin cSi layer was dissolved, the etching effectively continued only on the bulk silicon side. The thin silica layer is therefore effective in stopping the cSi etching process for a time period of at least several days. The determined cSi etch rate was significantly lower compared to the literature with only about 1.5 $\mu\text{m}/\text{h}$. The reason for that was most likely the evaporation of water which increases the KOH concentration and in turn results in decreasing etching rates. This shows, that the solution needs to be protected from evaporation by covering the beakers with a lid.

Further tests showed, that the etching process did not immediately start for some SOI wafers. Certain parts of the wafer surface remained unaffected by the solution after 24 h, while other parts began to be etched forming irregular indentations of varying depths. This was probably caused by an oxide layer on the surface of the bulk silicon, which slowly formed over time as it was stored in air where the cSi reacted with surrounding oxygen. As the solution did not break through this passivation layer evenly, the indentations were formed. A mechanical ablation of some surface material to remove the oxide layer shortly before the start of the etching process prevented the time delay and irregular start. In addition, it also greatly reduces the total etching time for the final samples. In the end, the etching rate was found to average to about 5 $\mu\text{m}/\text{h}$, which is in agreement with the literature.

Tests with the remaining bonded pieces of the cut-out samples revealed that the bond between the SOI wafers and silica substrates is not completely resistant to the etching solution. As a consequence, the bond is at first partly damaged near the sample edges creating several defects in the thin layers and later the wafer detaches from the substrate if the sample is completely submerged by the KOH solution. Therefore, the sides of samples, where the bond is exposed to the solution, needs to be protected. As there were no suitable lacquers or similar materials found that could be used to coat the sample side to shield the bond from the KOH solution, a special steel beaker I designed was used.

A cross-section of a 3D model of the steel beaker is shown in figure 7.3. The to be etched

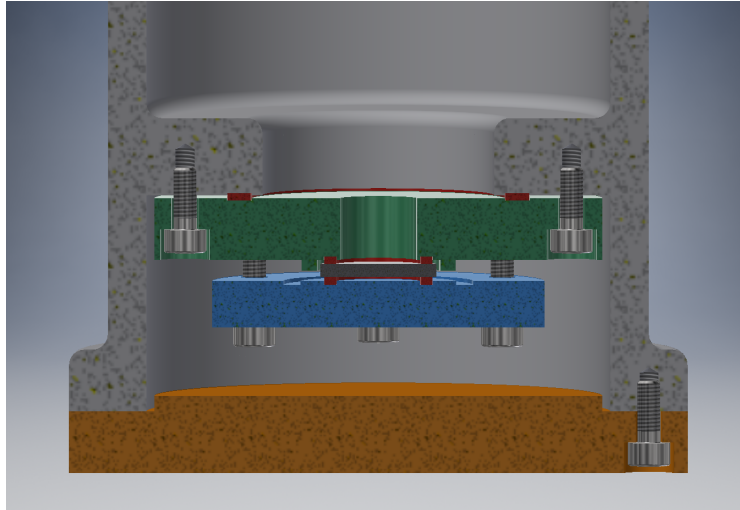


FIGURE 7.3: Cross-section of the 3D modelled steel beaker used for etching of the bonded cSi toplayer prototype samples. The sample (black) is held with the silicon (thick wafer) side up in the centre between PTFE sealing (red), which is pressed together by the adapter (green) and end plate (blue). The parts are fixed to the main beaker (grey) and a cap closes the bottom (orange). For the etching process, the top of the beaker is filled with the etching solution.

sample (black) is held with the silicon (thick wafer) side up in the centre of the beaker between sealing (red) made of Polytetrafluoroethylene (PTFE). To be leak-proof, the sealing and sample are pressed together by two steel parts: an adapter piece (green) and an end plate (blue). The adapter plate can be switched to accommodate varying sample sizes. The adapter is fixed to the main beaker (grey) with another PTFE seal between the parts. The bottom of the beaker is closed off by a cap (orange) to prevent contamination of the sensitive samples. The parts are held together by a multitude of screws. For the etching process to be carried out, the KOH solution is filled into the top part of the beaker. The tight sealing prevents the solution to reach the side of the sample where the sensitive bond is exposed, so that only the uncovered top, centre part of the cSi bulk wafer is etched. The top of the beaker is loosely closed off by another lid (not shown in the figure) to prevent the evaporation of the solution and to ensure an even etching speed while the hydrogen that is produced in the etching process can still escape. All parts except for the sealing and the sample itself are made of stainless steel, which is resistant to the KOH solution.

The etching process is stopped once the bulk silicon is removed because the thin silica layer following it is nearly unaffected by the KOH solution as shown by the etching tests and predicted by the literature [Sei90]. The resulting sample using the steel beaker is shown in figure 7.4. The rim of the sample where the PTFE sealing was located remained mostly intact, since it was only partly exposed to the KOH solution. In the centre however, the cSi was completely removed, revealing a partly translucent coating that is made of the thin silica and cSi layers of the original SOI wafer. For the removal of the silica layer on top without damaging the cSi layer below, the only viable option is the utilisation of hydrofluoric acid. However, this was not attempted for this prototype sample because



FIGURE 7.4: The cSi toplayer prototype sample after the etching process in the steel beaker. The bulk cSi was removed and only the thin silica and cSi layers of the original SOI wafer remained on the substrate.

the available chemical laboratory was not equipped to handle hydrofluoric acid, which potentially poses high health risks.

7.4 Analysis and Discussion

The produced silica and cSi coated prototype sample was analysed by measuring its transmission spectrum from 200 nm to 3000 nm with a *Cary 5000 UV-Vis-NIR* spectrometer. A representative model was then fitted to the measurement using *SCOUT* (see also subsection 5.2.1). For the silica layer, the same model with fixed optical properties that accurately described the nano-layered silica in section 6.2.1 and [Tai20] was used. The model utilised for the cSi layer was predefined by Scout and also had fixed optical properties. It was based on the measurements published in [Jel92] which were extrapolated into the remaining wavelength regions of the measured transmission spectrum.

In figure 7.5, the measured transmission spectrum as well as the fit and their difference is shown. Furthermore, the transmission without the silica layer of the sample is depicted as modelled by Scout. The deviation between the measurement and the fit is less than 3% for most of the considered wavelength region. The fit differs only in the narrow area between 400 nm and 600 nm more from the measurement. The model should therefore represent the prototype sample relatively accurate in particular in the wavelength region between 1000 nm and 2000 nm, which is of interest for mirror coating of GWDs. The modelled thickness of the cSi layer was 213 nm which is only 3% thinner than the nominal thickness of 220 nm. This small difference might stem from the slightly deviating fit. The thickness of the silica layer was modelled to be 2687 nm, which is about 10% thinner than the nominal thickness of 3 μm . However, this was expected as silica is not completely resistant to the used KOH etching solution resulting in a slow ablation of material.

The transmission spectrum reveals that the production process of the prototype sample was successfully carried out. No optical abnormalities were found since the sample behaves optically as expected from a silica-cSi bilayer as if it were deposited by common methods on a silica substrate. This shows, that the SOI technology can be used to produce thin cSi layers with optical thicknesses in the order of quarter wave layers at wavelengths

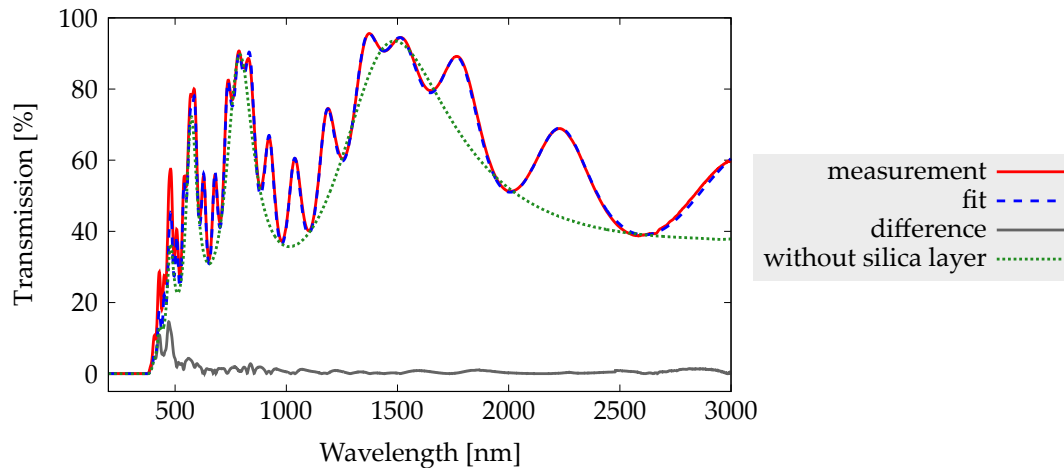


FIGURE 7.5: Scout fit compared to the transmission spectrum of the produced cSi toplayer prototype sample. Shown are the measurement of the sample, the fit by Scout, the difference between both and the transmission spectrum if the remaining silica layer was removed in the model.

relevant for future GWDs. Due to its optical behaviour, the so produced cSi layers seem also suitable to be utilised in mirror coatings.

The production of the discussed prototype sample is a promising first result for the implementation of a cSi toplayer with the next step being the investigation on the removal of the remaining silica layer and mechanical loss measurements of the cSi toplayer including the bond. Afterwards, the production of an HR sample with a complete coating including an amorphous layer stack can be attempted. In combination with aSi layers, this could yield in coatings with significantly reduced thermal noise that still fulfil the strict absorption requirements of future GWDs.

Chapter 8

Conclusion

8.1 Summary

Amorphous silicon is an interesting material candidate to be implemented in future mirror coatings for test masses of gravitational wave detectors. The optical absorption of amorphous silicon is relatively high compared to alternative materials and is restricting its utilisation in gravitational wave detectors. The reduction of the optical absorption in amorphous silicon is therefore one main concern of current research. To determine the absorption of optical samples, I set up a measuring system that utilises the technique of photothermal common-path interferometry (PCI). This system was used to measure the optical absorption in my coating studies once it was ready. In addition, I successfully simulated the complex signal formation and detection in PCI systems for a better understanding of the measuring technique. The comparison with the real system showed that the simulation was accurately representing well aligned PCI systems.

I have produced several amorphous silicon thin films under varying conditions using a pulsed laser deposition system and investigated the coating properties utilising multiple analysing methods. Here, the main focus was on the influence of various parameters on the optical absorption which was not systematically studied previously. I was able to determine several basic correlations between different properties of the amorphous silicon coatings. I also analysed the underlying absorption mechanisms with some results confirming previous research in the field and other results contradicting them.

Nano-layer coatings were proposed as a countermeasure to the crystallisation of coating materials possible allowing for higher heat treatment temperatures than in stacks made of conventional quarter wave layers. The higher temperatures might further improve the optical and mechanical properties. I have investigated nano-layer coatings made of 35 individual layers of amorphous silicon and silica adding up to an optical thickness of about 1160 nm and examined their properties using different methods. While no increase in crystallisation temperature compared to amorphous silicon quarter wave layers could be observed, an influence of the nano-layers on the optimal heat treatment temperature can also not be ruled out due to the varying thicknesses of the individual coating layers.

Crystalline silicon would be an excellent material to be used in mirror coatings for gravitational wave detectors but it cannot be grown as part of a single crystalline coating due to the lack of a matching partner material. Therefore, a method is required to mix crystalline and amorphous layers. A special production process was previously proposed to implement a single crystalline silicon toplayer on an otherwise amorphous coating stack. I have investigated the feasibility of this production process by producing a first prototype sample. The prototype was made of a single crystalline silicon and silica bilayer bonded to a fused silica substrate. The sample behaved optically as expected and no adverse effects of the bonding could be found.

8.2 Outlook

Amorphous silicon and crystalline silicon have the potential to improve the mechanical properties of mirror coatings for gravitational wave detectors over current designs and might enable future multi-material coatings to reach the strict design requirements of third generation detectors. The coating examinations and results presented in this thesis serve as a basis for further investigations of silicon based mirror coatings for gravitational wave detectors.

Additional investigations about the fundamental correlations between deposition parameters of amorphous silicon and its properties could be of interest to gain further insights on the prevailing optical absorption mechanisms. In combination with heat treatment studies, this might enable the production of amorphous silicon layers with lower optical absorption compared to coatings produced using currently common deposition parameters and techniques. In relation to this study, a systematic investigation on the influence of the substrate material on amorphous silicon might be of interest.

An additional study of amorphous silicon and silica nano-layer stacks is required to evaluate the possible benefits of nano-layered structures in amorphous silicon based mirror coatings for gravitational wave detectors. The nano-layers investigated in this study would need to be more evenly distributed than in the coating stacks discussed in this thesis. In addition, even thinner individual layers would be favourable to rule out the layer thicknesses as the reason for the reported lack of suppression in crystallisation. Furthermore, the influence on the mechanical loss has yet to be examined and corresponding measurements should be accompanying future investigations on silicon based nano-layer coatings. At the University of Glasgow, there is currently such a study on nano-layer coatings ongoing including associated mechanical loss measurements at room temperature as well as cryogenic temperatures.

The next step for the implementation of a crystalline silicon toplayer in a mirror coating is the investigation of the removal of the remaining silica layer covering the crystalline silicon of the produced prototype sample discussed in this thesis. In addition, a method needs to be found so that no rim of crystalline silicon remains on the sample after the etching process. This could be achieved by utilising another bonding technique that is

resistant to the etching solution or by using an etching method which does not affect the bond. Afterwards, samples including a suitable amorphous layer stack should be produced and investigated. These next steps are currently planned to be carried out at Maastricht University. Finally, if the toplayer concept proves to be feasible, the application on large scale mirrors for gravitational wave detectors needs to be tested.

The application of a crystalline silicon toplayer in combination with an amorphous silicon based highly reflective multi-material coating promises a reduction of 32 % in thermal noise at room temperature compared to currently used silica-tantala coatings with only a moderate increase in optical absorption at 1550 nm from 1.7 ppm to 3.2 ppm [Ste16a]. Further improvements of absorption in the amorphous silicon layers should be possible as described above and could reduce the inflicted increase in absorption. If the improvement in absorption is sufficiently large, it might even be possible to utilise a higher number of amorphous silicon layers in the coatings which would reduce the thermal noise by a total of 37% compared to current coatings. Moreover, this coating design might also additionally benefit from the application of nano-layered structures. Lastly, some future gravitational wave interferometers are planned to operate at cryogenic temperatures, which would further decrease the thermal noise. For these detectors, the utilisation of amorphous silicon is of particular interest as its mechanical loss reduces towards lower temperatures while that of currently used materials increases. Therefore, the research presented in this thesis has the potential to contribute significantly to the realization of coatings with reduced thermal noise for the next generation of gravitational wave detectors.

Appendix

Appendix A

PCI Simulation Code

The optical absorption values presented in this thesis were measured using the PCI technique (see chapter 4). I have simulated the formation and detection of the absorption signal using the open source software *Finesse* embedded in its *Python* wrapper *PyKat*. The complete simulation code is shown below. All simulations presented in this thesis were calculated with a maximum considered mode order of 40 (see line 46 in the simulation code). This ensured a high accuracy of the simulations while still keeping the calculation time to an acceptable level.

```

1 # -*- coding: utf-8 -*-
2 """
3 Created on Tue Apr 14 14:04:01 2020
4 simulation code last modified on Apr 29 2022
5
6 @author: Lukas Terkowski
7
8 Photothermal common-path interferometry (PCI):
9 interference pattern and signal strenghts
10
11 Notes:
12 - only probe beam (big beam) and its disturbance (small beam) simulated
13   -> done by overlapping the undisturbed beam and its disturbance on a BS
14 - perfectly symmetrical disturbance of the probe beam
15   -> referring to a cross angle of 0 deg between pump and probe beam
16   -> waist of pump and probe at the same position in x and y
17 - lenses modeled as "thin" lenses
18 """
19
20 from pykat import finesse          # import the whole pykat.finesse package
21 import numpy as np                # for basic math/sci/array functions
22 import matplotlib.pyplot as plt   # for plotting
23
24 # ----- Setup Parameters ----- #
25 wavelength = 1310e-9             # wavelength of the PCI probe beam
26 waist_pump = 35e-6               # size of the waist of the pump beam (disturbance)
27 waist_probe = 105e-6             # size of the waist of the probe beam
28 PD_diameter_mm = 1               # diameter of the active area of the PD in mm
29 f_IS_lens_mm = 40                # focal length of the IS lens (thin lens approx)
30 MB_diameter_mm = 6               # diameter in mm of the IS metal ball (refl. lens)
31
32 # ----- Options (True / False) ----- #
33 imaging_stage = True              # False: pure signal without an imaging stage
34 beam_parameter = True             # triggers beam parameter output

```

```

35 intensity_map = True
36 power_recon = True           # check how much power is inside the intensity maps
37 # ->if reconstructed power is much smaller than p_out, xscan_width is too small
38 distance_map = True
39 PD_signals = True           # works only for an odd number of plotpoints_xscan
40 # ->if out of bound error occurs in line 250, PD is bigger than xscan_width
41
42 # ----- Simulation Values ----- #
43 # global:
44 p_out = 1e-3                # power (W) of normalized (probe) beam
45 p_ratio_beams = 1e-2        # power ratio of small/big beam
46 maxtemorder = 40           # maximum order of considered modes
47 # -> higher for more accuracy, at least 30 for realistic results
48 # -> increases computation time significantly
49 xscan_width = 150          # +- width of plot in w0 of undisturbed (big) beam
50 # -> needs to big enough to calculate PD_signals
51 Lscan_start_mm = 120       # start position of the BP for distance scan
52 Lscan_distance_mm = 50     # travel distance of the BP distance scan
53 plotpoints_xscan = 81      # number of points for the xscan, needs to be odd
54 plotpoints_Lscan = 81      # number of points for the Lscan
55 # only without imaging stage (IS)
56 pos_beamparameter_mm = 3   # beam parameters position after beam crossing in mm
57 pos_intensity_map_mm = 3   # intensity map position after beam crossing in mm
58 # only with imaging stage (IS)
59 ISspace = 1                # IS space, that is scanned: 1, 2 or 3
60 ISspace1_mm = 150          # distance beam crossing to lens in mm
61 ISspace2_mm = 53.5         # distance lens to metal ball in mm
62 ISspace3_mm = 85           # distance metal ball to photo diode in mm
63
64 # ----- Plots Output (True / False) ----- #
65 plot_bigbeam = True
66 plot_bothbeams = True
67 plot_difference = True
68 x0profile = True
69
70 # ----- #
71 # ----- Code ----- #
72 # ----- #
73
74 # calculation of required parameters or changing of units
75 PD_radius = PD_diameter_mm / 2000
76 bigpower = 2 * p_out
77 smallpower = bigpower * p_ratio_beams
78 xscan_start = -1 * xscan_width
79 xscan_end = xscan_width
80 Lscan_start = Lscan_start_mm / 1000
81 Lscan_distance = Lscan_distance_mm / 1000
82 Lscan_end = Lscan_start + Lscan_distance
83 plotsteps_xscan = plotpoints_xscan - 1
84 plotsteps_Lscan = plotpoints_Lscan - 1
85 xscan_stepsize = xscan_width * 2 / plotsteps_xscan
86 x0index = plotpoints_xscan // 2
87 Lscan_stepsize = Lscan_distance / plotsteps_Lscan
88 pos_intensity_map = pos_intensity_map_mm / 1000
89 pos_beamparameter = pos_beamparameter_mm / 1000
90 f_IS_lens = f_IS_lens_mm / 1000
91 f_IS_MB = -1 * MB_diameter_mm / 4000
92 ISspace1 = ISspace1_mm / 1000
93 ISspace2 = ISspace2_mm / 1000
94 ISspace3 = ISspace3_mm / 1000

```

```

95
96 # changing of labels according to the input
97 if imaging_stage:
98     label_plot_title_IM = f'@ {ISspace1_mm}/{ISspace2_mm}/{ISspace3_mm} mm'
99     DM_space = f'space{Lscan_ISspace+2}'
100     label_DMplot = f'{Lscan_ISspace}. imaging stage space [mm]'
101     if Lscan_ISspace == 1:
102         label_plot_title_DM = f'@ xx/{ISspace2_mm}/{ISspace3_mm} mm'
103     elif Lscan_ISspace == 2:
104         label_plot_title_DM = f'@ {ISspace1_mm}/xx/{ISspace3_mm} mm'
105     else:
106         label_plot_title_DM = f'@ {ISspace1_mm}/{ISspace2_mm}/xx mm'
107 else:
108     label_plot_title_IM = f'@ {pos_intensity_map_mm} mm'
109     DM_space = 'space5'
110     label_DMplot = 'distance to beam crossing [mm]'
111     label_plot_title_DM = f''
112
113 # ----- Finesse Code ----- #
114 kat_big = f'''
115 lambda {wavelength}
116
117 l biglaser {bigpower} 0 0          n1          # "probe"
118 s space1 1 1                      n1 n2
119 gauss biggauss biglaser n1 {waist_probe} -1
120 '''
121
122 kat_small = f'''
123 l smalllaser {smallpower} 0 0      n3          # "pump"
124 s space2 1 1                      n3 n6
125 gauss smallgauss smalllaser n3 {waist_pump} -1
126
127 maxtem {maxtemorder}
128 '''
129
130 kat_bs = f'''
131 bs1 bs 0.5 0 0 45                 n2 dump n5 n6
132 '''
133
134 kat_noIS = f'''
135 s space5 {Lscan_start} 1          n5 n11
136 '''
137
138 kat_IS = f'''
139 s space3 {ISspace1} 1             n5 n7
140
141 lens lensIS {f_IS_lens}          n7 n8   # not a thin lens in reality
142
143 s space4 {ISspace2} 1             n8 n9
144
145 lens lensball {f_IS_MB}          n9 n10
146
147 s space5 {ISspace3} 1            n10 n11
148 '''
149
150 kat_bparameter = f'''
151 bp bpw0 x w0                     n11
152 bp bpw x w                       n11
153 bp bpz x z                       n11
154 bp bpg x g                       n11

```

```

155
156 noxaxis
157 '''
158
159 kat_bprofiler_IM = f'''
160 beam BP                                n11
161
162 xaxis BP x lin {xscan_start} {xscan_end} {plotsteps_xscan}
163 x2axis BP y lin {xscan_start} {xscan_end} {plotsteps_xscan}
164 '''
165
166 kat_bprofiler_DM = f'''
167 beam BP                                n11
168 bp bpw0 x w0                            n11
169
170 xaxis BP x lin {xscan_start} {xscan_end} {plotsteps_xscan}
171 x2axis {DM_space} L lin {Lscan_start} {Lscan_end} {plotsteps_Lscan}
172 '''
173
174 # ----- PCI Simulations ----- #
175 if beam_parameter or (intensity_map and power_recon) or PD_signals:
176     kat1 = finesse.kat()
177     kat1.parse(kat_big)
178     kat1.parse(kat_bs)
179     if imaging_stage:
180         kat1.parse(kat_IS)
181     else:
182         kat1.parse(kat_noIS)
183         kat1.space5.L = pos_beamparameter
184     kat1.parse(kat_bparameter)
185     out1 = kat1.run()
186
187 if intensity_map:
188     kat22 = finesse.kat()
189     kat22.parse(kat_big)
190     kat22.parse(kat_bs)
191     if imaging_stage:
192         kat22.parse(kat_IS)
193     else:
194         kat22.parse(kat_noIS)
195         kat22.space5.L = pos_intensity_map
196     kat22.parse(kat_bprofiler_IM)
197     out22 = kat22.run()
198     if plot_bigbeam:
199         plt.figure(dpi=200)
200         plt.pcolormesh(out22.x, out22.y, out22['BP']/1e0)
201         plt.title('only probe beam ' + label_plot_title_IM)
202         plt.xlabel('x [w0]')
203         plt.ylabel('y [w0]')
204         plt.colorbar(label='Intensity [W/m^2]')
205         plt.show()
206
207 if distance_map:
208     kat21 = finesse.kat()
209     kat21.parse(kat_big)
210     kat21.parse(kat_bs)
211     if imaging_stage:
212         kat21.parse(kat_IS)
213     else:
214         kat21.parse(kat_noIS)

```

```

215 kat21.parse(kat_bprofiler_DM)
216 out21 = kat21.run()
217 normbig_DM = out21['BP']
218 normbig_DM_swapxy = normbig_DM.transpose()
219 if plot_bigbeam:
220     plt.figure(dpi=200)
221     plt.pcolormesh(out21.y*1e3, out21.x, normbig_DM_swapxy/1e0)
222     plt.title('only probe beam ' + label_plot_title_DM)
223     plt.xlabel(label_DMplot)
224     plt.ylabel('y [w0]')
225     plt.colorbar(label='Intensity [W/m^2]')
226     plt.show()
227
228 if distance_map and x0profile and plot_bigbeam:
229     x0profileNbigDM = normbig_DM_swapxy[x0index]
230     plt.figure(dpi=200)
231     plt.plot(out21.y*1e3, x0profileNbigDM/1e0)
232     plt.title('only probe beam, x0-profile ' + label_plot_title_DM)
233     plt.xlabel(label_DMplot)
234     plt.ylabel('Intensity at center [W/m^2]')
235     plt.show()
236
237 if PD_signals and distance_map:
238     # even plotpoints_xscan numbers are not implemented
239     w0big_DM = out21['bpw0'].transpose()[x0index]
240     ring_thicknesses_big = xscan_stepsize * w0big_DM
241     PD_power_big = np.array([])
242     for i in range(plotpoints_Lscan):
243         ring_power_0 = normbig_DM[i][x0index] * 0.25*np.pi * \
244             ring_thicknesses_big[i]**2
245         power_sum_i = ring_power_0
246         n = 1
247         outer_radius_n = ring_thicknesses_big[i] * (n + 0.5)
248         while outer_radius_n < PD_radius:
249             ring_area_n = 2 * np.pi * n * ring_thicknesses_big[i]**2
250             ring_power_n = normbig_DM[i][x0index + n] * ring_area_n
251             power_sum_i = power_sum_i + ring_power_n
252             n = n + 1
253             outer_radius_n = outer_radius_n + ring_thicknesses_big[i]
254             rest_thickness = PD_radius - (outer_radius_n - ring_thicknesses_big[i])
255             rest_area = np.pi * (rest_thickness**2 + 2 * rest_thickness *
256                 (outer_radius_n - ring_thicknesses_big[i]))
257             rest_power = normbig_DM[i][x0index + n] * rest_area
258             power_sum_i = power_sum_i + rest_power
259             PD_power_big = np.append(PD_power_big, power_sum_i)
260     if plot_bigbeam:
261         plt.figure(dpi=200)
262         plt.plot(out21.y*1e3, PD_power_big*1e6)
263         plt.title('only probe beam, PD signal ' + label_plot_title_DM)
264         plt.xlabel(label_DMplot)
265         plt.ylabel('PD power at beam center [uW]')
266         plt.show()
267
268 if intensity_map:
269     kat42 = finesse.kat()
270     kat42.parse(kat_big)
271     kat42.parse(kat_small)
272     kat42.parse(kat_bs)
273     if imaging_stage:
274         kat42.parse(kat_IS)

```

```

275     else:
276         kat42.parse(kat_noIS)
277         kat42.space5.L = pos_intensity_map
278     kat42.parse(kat_bprofiler_IM)
279     out42 = kat42.run()
280     if plot_bothbeams:
281         plt.figure(dpi=200)
282         plt.pcolormesh(out42.x, out42.y, out42['BP']/((1+p_ratio_beams)*1e0))
283         plt.title('with pump beam ' + label_plot_title_IM +
284                 f', maxtem: {maxtemorder}')
285         plt.xlabel('x [w0]')
286         plt.ylabel('y [w0]')
287         plt.colorbar(label='Intensity [W/m^2]')
288         plt.show()
289
290 if distance_map:
291     kat41 = finesse.kat()
292     kat41.parse(kat_big)
293     kat41.parse(kat_small)
294     kat41.parse(kat_bs)
295     if imaging_stage:
296         kat41.parse(kat_IS)
297     else:
298         kat41.parse(kat_noIS)
299     kat41.parse(kat_bprofiler_DM)
300     out41 = kat41.run()
301     normboth_DM = out41['BP']/((1+p_ratio_beams)
302     normboth_DM_swapxy = normboth_DM.transpose()
303     if plot_bothbeams:
304         plt.figure(dpi=200)
305         plt.pcolormesh(out41.y*1e3, out41.x, normboth_DM_swapxy/1e0)
306         plt.title('with pump beam ' + label_plot_title_DM +
307                 f', maxtem: {maxtemorder}')
308         plt.xlabel(label_DMplot)
309         plt.ylabel('y [w0]')
310         plt.colorbar(label='Intensity [W/m^2]')
311         plt.show()
312
313 if distance_map and x0profile and plot_bothbeams:
314     x0profileNbothDM = normboth_DM_swapxy[x0index]
315     plt.figure(dpi=200)
316     plt.plot(out41.y*1e3, x0profileNbothDM/1e0)
317     plt.title('with pump beam, x0-profile ' + label_plot_title_DM +
318             f', maxtem: {maxtemorder}')
319     plt.xlabel(label_DMplot)
320     plt.ylabel('Intensity at center [W/m^2]')
321     plt.show()
322
323 if PD_signals and distance_map:
324     # even plotpoints_xscan numbers are not implemented
325     w0both_DM = out41['bpw0'].transpose()[x0index]
326     ring_thicknesses_both = xscan_stepsize * w0both_DM
327     PD_power_both = np.array([])
328     for i in range(plotpoints_Lscan):
329         ring_power_0 = normboth_DM[i][x0index] * 0.25*np.pi * \
330                 ring_thicknesses_both[i]**2
331         power_sum_i = ring_power_0
332         n = 1
333         outer_radius_n = ring_thicknesses_both[i] * (n + 0.5)
334         while outer_radius_n < PD_radius:

```

```

335     ring_area_n = 2 * np.pi * n * ring_thicknesses_both[i]**2
336     ring_power_n = normboth_DM[i][x0index + n] * ring_area_n
337     power_sum_i = power_sum_i + ring_power_n
338     n = n + 1
339     outer_radius_n = outer_radius_n + ring_thicknesses_both[i]
340     rest_thickness = PD_radius - (outer_radius_n - ring_thicknesses_both[i])
341     rest_area = np.pi * (rest_thickness**2 + 2 * rest_thickness *
342                        (outer_radius_n - ring_thicknesses_both[i]))
343     rest_power = normboth_DM[i][x0index + n] * rest_area
344     power_sum_i = power_sum_i + rest_power
345     PD_power_both = np.append(PD_power_both, power_sum_i)
346 if plot_bothbeams:
347     plt.figure(dpi=200)
348     plt.plot(out41.y*1e3, PD_power_both*1e6)
349     plt.title('with pump beam, PD signal ' + label_plot_title_DM +
350             f', maxtem: {maxtemorder}')
351     plt.xlabel(label_DMplot)
352     plt.ylabel('PD power at beam center [uW]')
353     plt.show()
354
355 if intensity_map and plot_difference:
356     normdiffmap_IM = out42['BP']/(1+p_ratio_beams) - out22['BP']
357     plt.figure(dpi=200)
358     plt.pcolormesh(out42.x, out42.y, normdiffmap_IM/1e0)
359     plt.title('absorption signal ' + label_plot_title_IM +
360             f', maxtem: {maxtemorder}')
361     plt.xlabel('x [w0]')
362     plt.ylabel('y [w0]')
363     plt.colorbar(label='Intensity [W/m^2]')
364     plt.show()
365
366 if intensity_map and power_recon:
367     rec_pow_big = (xscan_stepsize * out1['bpw0'])**2 * np.sum(out22['BP'])
368     rec_pow_both = (xscan_stepsize * out1['bpw0'])**2 * np.sum(out42['BP'])
369     rec_pow_both_norm = rec_pow_both/(1+p_ratio_beams)
370     rec_pow_diff = rec_pow_both_norm - rec_pow_big
371     rec_pow_big_mW = rec_pow_big*1e3
372     rec_pow_both_mW = rec_pow_both*1e3
373     rec_pow_both_norm_mW = rec_pow_both_norm*1e3
374     rec_pow_diff_mW = rec_pow_diff*1e3
375
376 if distance_map:
377     normdiffmap_DM = out41['BP']/(1+p_ratio_beams) - out21['BP']
378     maxdiff = np.amax(normdiffmap_DM)
379     maxdiffind = np.where(normdiffmap_DM == maxdiff)
380     maxdiffposx = maxdiffind[1][0] * xscan_stepsize + xscan_start
381     maxdiffposy = maxdiffind[0][0] * Lscan_stepsize + Lscan_start
382     mindiff = np.amin(normdiffmap_DM)
383     mindiffind = np.where(normdiffmap_DM == mindiff)
384     mindiffposx = mindiffind[1][0] * xscan_stepsize + xscan_start
385     mindiffposy = mindiffind[0][0] * Lscan_stepsize + Lscan_start
386     normdiffmap_DM_swapxy = normdiffmap_DM.transpose()
387 if plot_difference:
388     plt.figure(dpi=200)
389     plt.pcolormesh(out41.y*1e3, out41.x, normdiffmap_DM_swapxy/1e0)
390     plt.title(f'absorption signal ' + label_plot_title_DM +
391             f', maxtem: {maxtemorder}')
392     plt.xlabel(label_DMplot)
393     plt.ylabel('y [w0]')
394     plt.colorbar(label='Intensity [W/m^2]')

```

```

395     plt.show()
396
397 if distance_map and x0profile and plot_difference:
398     x0profileNDM = x0profileNbothDM - x0profileNbigDM
399     x0profileNDM_abs = abs(x0profileNDM)
400     x0profileNDM_maxind = np.where(x0profileNDM == np.amax(x0profileNDM))[0][0]
401     x0profileNDM_maxpos = Lscan_start + x0profileNDM_maxind * Lscan_stepsize
402     x0profileNDM_minind = np.where(x0profileNDM == np.amin(x0profileNDM))[0][0]
403     x0profileNDM_minpos = Lscan_start + x0profileNDM_minind * Lscan_stepsize
404     plt.figure(dpi=200)
405     plt.plot(out41.y*1e3, x0profileNDM_abs/1e0)
406     if Lscan_ISspace == 1:
407         plt.title('Intensity: "Butterfly" curve ' + label_plot_title_DM +
408                 f', maxtem: {maxtemorder}')
409     else:
410         plt.title('absorption signal intensity (absolute), x0-profile, ' +
411                 label_plot_title_DM + f', maxtem: {maxtemorder}')
412     plt.xlabel(label_DMplot)
413     plt.ylabel('Intensity at center [W/m^2]')
414     plt.show()
415
416 if PD_signals and distance_map and plot_difference:
417     PD_power_diff = PD_power_both - PD_power_big
418     PD_power_diff_abs = abs(PD_power_diff)
419     PD_power_diff_maxind = np.where(PD_power_diff ==
420                                     np.amax(PD_power_diff))[0][0]
421     PD_power_diff_maxpos = Lscan_start + PD_power_diff_maxind * Lscan_stepsize
422     PD_power_diff_minind = np.where(PD_power_diff ==
423                                     np.amin(PD_power_diff))[0][0]
424     PD_power_diff_minpos = Lscan_start + PD_power_diff_minind * Lscan_stepsize
425     plt.figure(dpi=200)
426     plt.plot(out21.y*1e3, PD_power_diff_abs*1e6)
427     if Lscan_ISspace == 1:
428         plt.title('PD: "Butterfly" curve ' + label_plot_title_DM +
429                 f', maxtem: {maxtemorder}')
430     else:
431         plt.title('PD: AC signal (absolute) ' + label_plot_title_DM +
432                 f', maxtem: {maxtemorder}')
433     plt.xlabel(label_DMplot)
434     plt.ylabel('AC power at beam center [uW]')
435     plt.show()
436
437 # ----- Final Output ----- #
438 if beam_parameter:
439     print('-----')
440     print('Final beam parameters (only probe beam)')
441     if imaging_stage:
442         print(f'ISspace1 = {ISspace1_mm} mm')
443         print(f'ISspace2 = {ISspace2_mm} mm')
444         print(f'ISspace3 = {ISspace3_mm} mm')
445     else:
446         print(f'distance to beam crossing: {pos_beamparameter_mm} mm')
447     print('w0 = {:.2f} um'.format(out1['bpw0']*1e6))
448     print('w(z) = {:.2f} um'.format(out1['bpw']*1e6))
449     print('z = {:.2f} mm'.format(out1['bpz']*1e3))
450     print('g = {:.2f} deg (Gouy phase)'.format(out1['bpg']*180/np.pi))
451
452 if intensity_map and power_recon:
453     print('-----')
454     print('Reconstructed powers from the intensity maps')

```

```

455     print('big beam: {:.3f} mW'.format(rec_pow_big_mW))
456     print('both beams: {:.3f} mW'.format(rec_pow_both_mW))
457     print('norm. both beams: {:.3f} mW'.format(rec_pow_both_norm_mW))
458     print('norm. diff.: {:.2e} mW'.format(rec_pow_diff_mW))
459
460 if distance_map and not (x0profile and plot_difference and Lscan_ISspace == 1):
461     print('-----')
462     print('max neg. signal intensity')
463     print('value: {:.2f} W/m^2'.format(mindiff/1e0))
464     if mindiffposx != 0:
465         print('x-position (w0): {:.1f}'.format(mindiffposx))
466     print('position: {:.1f} mm'.format(mindiffposy*1e3))
467     print('max pos. signal intensity')
468     print('value: {:.2f} W/m^2'.format(maxdiff/1e0))
469     if maxdiffposx != 0:
470         print('x-position (w0): {:.1f}'.format(maxdiffposx))
471     print('position: {:.1f} mm'.format(maxdiffposy*1e3))
472
473 if distance_map and x0profile and plot_difference and Lscan_ISspace == 1:
474     print('-----')
475     if mindiffposx != 0 or maxdiffposx != 0:
476         print('ATTENTION:')
477         print('the x-position of the maximum negative or positive signal')
478         print('intensity (defining the first and second peak) is not 0 and')
479         print('therefore not on the x0-profile graph displayed here.')
480         print('-----')
481         print('max neg. signal intensity')
482         print('value: {:.1f} W/m^2'.format(mindiff/1e0))
483         print('x-position (w0): {:.1f}'.format(mindiffposx))
484         print('position: {:.1f} mm'.format(mindiffposy*1e3))
485         print('max pos. signal intensity')
486         print('value: {:.1f} W/m^2'.format(maxdiff/1e0))
487         print('x-position (w0): {:.1f}'.format(maxdiffposx))
488         print('position: {:.1f} mm'.format(maxdiffposy*1e3))
489         print('-----')
490     print('Intensity - "butterfly" curve, peak analysis')
491     print('first peak value: {:.2f} W/m^2'
492           .format(-1*np.amin(x0profileNDM)/1e0))
493     print('first peak position: {:.1f} mm'.format(x0profileNDM_minpos*1000))
494     print('second peak value: {:.2f} W/m^2'
495           .format(np.amax(x0profileNDM)/1e0))
496     print('second peak position: {:.1f} mm'.format(x0profileNDM_maxpos*1000))
497     print('peak ratio: {:.3f}'
498           .format(np.amax(x0profileNDM)/(-1*np.amin(x0profileNDM))))
499
500 if distance_map and PD_signals and plot_difference and not Lscan_ISspace == 1:
501     print('-----')
502     if mindiffposx != 0 or maxdiffposx != 0:
503         print('ATTENTION:')
504         print('the x-position of the maximum negative or positive signal')
505         print('intensity is not 0, where the PD is positioned in this')
506         print('simulation. There might be a better PD position to get the')
507         print('maximum AC signal.')
508         print('-----')
509         print('max neg. signal intensity')
510         print('value: {:.1f} W/m^2'.format(mindiff/1e0))
511         print('x-position (w0): {:.1f}'.format(mindiffposx))
512         print('position: {:.1f} mm'.format(mindiffposy*1e3))
513         print('max pos. signal intensity')
514         print('value: {:.1f} W/m^2'.format(maxdiff/1e0))

```

```

515     print('x-position (w0): {:.1f}'.format(maxdiffposx))
516     print('position: {:.1f} mm'.format(maxdiffposy*1e3))
517     print('-----')
518     print('max neg. AC signal')
519     print('value: {:.2f} uW'.format(np.amin(PD_power_diff)*1e6))
520     print('position: {:.1f} mm'.format(PD_power_diff_minpos*1e3))
521     print('max pos. AC signal')
522     print('value: {:.2f} uW'.format(np.amax(PD_power_diff)*1e6))
523     print('position: {:.1f} mm'.format(PD_power_diff_maxpos*1e3))
524
525 if distance_map and PD_signals and plot_difference and Lscan_ISspace == 1:
526     print('-----')
527     if mindiffposx != 0 or maxdiffposx != 0:
528         print('ATTENTION:')
529         print('the x-position of the maximum negative or positive signal')
530         print('intensity is not 0, where the PD is positioned in this')
531         print('simulation. There might be a better PD position to get the')
532         print('maximum AC signal.')
533         print('-----')
534         print('max neg. signal intensity')
535         print('value: {:.1f} W/m^2'.format(mindiff/1e0))
536         print('x-position (w0): {:.1f}'.format(mindiffposx))
537         print('position: {:.1f} mm'.format(mindiffposy*1e3))
538         print('max pos. signal intensity')
539         print('value: {:.1f} W/m^2'.format(maxdiff/1e0))
540         print('x-position (w0): {:.1f}'.format(maxdiffposx))
541         print('position: {:.1f} mm'.format(maxdiffposy*1e3))
542         print('-----')
543     print('AC-signal: "butterfly" curve, peak analysis')
544     print('first peak value: {:.2f} uW'
545           .format(-1*np.amin(PD_power_diff)*1e6))
546     print('first peak position: {:.1f} mm'.format(PD_power_diff_minpos*1e3))
547     print('second peak value: {:.2f} uW'
548           .format(np.amax(PD_power_diff)*1e6))
549     print('second peak position: {:.1f} mm'.format(PD_power_diff_maxpos*1e3))
550     print('peak ratio: {:.3f}'
551           .format(np.amax(PD_power_diff)/(-1*np.amin(PD_power_diff))))

```

Appendix B

List of Produced aSi Coatings Using PLD

I produced a total number of 46 aSi coatings using PLD during the course of this thesis as described by subsection 5.1.3. While I thoroughly analysed 28 of them (see section 5.3), the other 18 coating were disregarded for my studies as they only served to test certain aspects of the PLD system or unforeseen circumstances rendered them unusable. Table B.1 lists the disregarded samples including the reasons for doing so. Tables B.2 and B.3 list all produced coatings chronologically, their defining deposition parameters and their most important properties.

TABLE B.1: List of produced aSi coatings using PLD, that were disregarded for a further analysis. A big part of the system control had to be replaced after the deposition of the Si35 coating, which made various following system tests necessary.

Coating name	Reason for disregarding the coating
Si08	small ablation area, high crystallisation ($\approx 17\%$)
Si09	small ablation area, high crystallisation ($\approx 23\%$)
Si10	ablation of target holder
Si20	ablation of target holder
Si24	ablation of target holder, changed velocity filter speed
Si25	changed velocity filter speed
Si26	ablation of target holder, laser beam path dealigned
Si27	laser beam path dealigned
Si29	beam scanning failure
Si36	general system function test
Si37	general system function test, ablation of target holder
Si38	general system function test
Si39	general system function test
Si40	general system function test, ablation of target holder
Si41	general system function test, ablation of target holder
Si42	general system function test, ablation of target holder
Si43	general system function test
Si44	general system function test

TABLE B.2: Complete chronological list of the produced aSi coatings using PLD including their most important properties and relevant deposition parameters, part 1.

Coating name	Deposition parameters									Coating properties						
	Analysis designation	Substrate material (C79xx)	Pulse energy (mJ)	Pulse repetition rate (Hz)	Pulse number	Substrate temperature (°C)	Gas flow into the chamber (SLM)	Ablation area (mm ²)	Crystallised area (%)	Scattering at 1550 nm (%)	Thickness (nm)	Average deposition rate (pm/s)	Refractive index at 1550 nm	Mobility gap energy (eV)	Extinction coefficient at 1550 nm ($\times 10^{-3}$)	Extinction coefficient at 2000 nm ($\times 10^{-4}$)
Si08	-	80	600	10	150k	RT	-	74	17.0	20.9	138	9.2	3.25	1.58	9.9	-
Si09	-	80	700	10	150k	RT	-	63	23.0	27.9	218	14.5	2.92	1.91	3.6	-
Si10	-	80	500	10	150k	RT	-	259	6.3	7.8	335	22.3	2.80	1.91	2.5	-
Si11	E1	80	400	10	150k	RT	-	154	8.0	12.3	285	19.0	2.85	1.80	1.0	-
Si12	E2	80	550	10	150k	RT	-	106	9.4	10.8	400	26.7	2.89	1.79	1.3	-
Si13	E3	80	550	10	150k	RT	-	146	12.6	14.7	353	23.5	2.79	1.82	1.2	-
Si14	E4	80	650	10	150k	RT	-	146	10.4	12.9	298	19.9	2.90	1.83	1.5	-
Si15	E5	80	750	10	150k	RT	-	148	10.0	16.0	499	33.3	3.04	1.80	2.1	-
Si16	E6	80	850	10	150k	RT	-	160	6.3	12.6	535	35.7	3.04	1.79	2.8	-
Si17	F2	80	550	10	150k	RT	-	208	7.7	9.2	260	17.4	2.86	1.85	1.3	-
Si18	F3	80	550	20	150k	RT	-	134	12.9	14.2	248	33.1	2.95	1.83	2.1	-
Si19	F4	80	550	30	150k	RT	-	160	4.5	8.9	102	20.4	2.68	2.44	1.8	-
Si20	-	80	550	30	150k	RT	-	193	10.7	9.7	156	31.3	3.31	1.54	5.4	-
Si21	F1	80	550	5	150k	RT	-	199	5.8	6.2	300	10.0	2.80	1.78	1.5	-
Si22	F5	80	550	40	150k	RT	-	191	6.3	3.5	142	37.9	3.11	1.75	2.5	-
Si23	F6	80	550	50	150k	RT	-	175	6.8	4.3	94	31.4	3.10	1.87	3.0	-
Si24	-	80	550	40	150k	RT	-	251	16.0	12.1	112	29.9	3.24	1.78	8.1	-
Si25	-	80	550	40	150k	RT	-	245	7.6	3.2	143	38.0	3.06	1.78	2.4	-
Si26	-	80	550	15	200k	RT	-	299	3.4	2.9	111	8.3	2.68	2.06	-	-
Si27	-	80	550	15	200k	RT	-	143	5.9	4.0	115	8.6	2.74	2.00	-	-
Si28	T1	79	550	15	200k	RT	-	194	9.7	8.6	291	21.8	2.97	1.82	2.1	6.0
Si29	-	79	550	15	200k	200	-	155	11.2	13.1	175	13.1	3.64	1.51	3.3	9.5
Si30	T4	79	550	15	200k	300	-	204	7.5	5.2	148	11.1	3.65	1.58	3.1	12.3
Si31	T3	79	550	15	200k	200	-	199	7.7	9.1	196	14.7	3.60	1.73	2.4	8.5
Si32	T5	79	550	15	200k	400	-	256	8.2	8.4	178	13.4	3.65	1.82	2.2	6.1
Si33	T7	79	550	15	200k	500	-	219	7.0	5.4	131	9.9	3.53	2.47	2.1	3.9
Si34	T2	79	550	15	200k	100	-	228	6.5	6.2	176	13.2	3.41	1.50	3.1	10.2
Si35	T6	79	550	15	200k	470	-	200	6.6	3.3	122	9.1	3.57	1.82	2.7	25.5

TABLE B.3: Complete chronological list of the produced aSi coatings using PLD including their most important properties and relevant deposition parameters, part 2. The coatings from Si36 to Si44 were produced to test and adjust the deposition system after parts of its control electronics and software were replaced.

Coating name	Analysis designation	Substrate material (C79XX)	Deposition parameters							Coating properties						
			Pulse energy (mJ)	Pulse repetition rate (Hz)	Pulse number	Substrate temperature (°C)	Gas flow into the chamber (SLM)	Ablation area (mm ²)	Crystallised area (%)	Scattering at 1550 nm (%)	Thickness (nm)	Average deposition rate (pm/s)	Refractive index at 1550 nm	Mobility gap energy (eV)	Extinction coefficient at 1064 nm ($\times 10^{-2}$)	Extinction coefficient at 2128 nm ($\times 10^{-4}$)
Si36	-	79	550	15	200k	RT	-	184	8.0	3.3	157	11.8	3.12	1.77	1.0	-
Si37	-	79	550	15	200k	RT	-	213	6.8	4.1	166	12.4	3.07	1.63	0.9	-
Si38	-	79	550	15	200k	RT	-	173	9.3	10.3	193	14.5	3.24	1.46	2.3	-
Si39	-	79	700	15	200k	RT	-	171	11.3	14.9	274	20.5	2.83	1.81	0.8	-
Si40	-	79	700	15	200k	RT	-	270	7.0	10.4	249	18.7	3.07	2.10	2.1	-
Si41	-	79	550	15	200k	RT	-	253	6.5	6.7	181	13.6	2.92	1.75	1.2	-
Si42	-	79	330	15	200k	RT	-	252	8.3	3.3	133	10.0	3.21	1.83	1.8	-
Si43	-	79	450	15	200k	RT	-	175	7.2	9.4	201	15.1	2.81	1.53	1.0	-
Si44	-	79	550	15	200k	RT	-	250	7.2	7.2	175	13.1	3.04	1.94	1.3	-
Si45	P1	79	700	15	200k	RT	-	221	9.2	10.7	300	22.5	3.14	2.21	2.7	11.4
Si46	P2	79	700	15	200k	RT	0.7	214	9.6	12.0	293	22.0	3.14	2.25	2.5	9.1
Si47	P3	79	700	15	200k	RT	1.4	228	16.6	16.8	313	23.5	3.38	1.95	2.4	13.3
Si48	P4	79	700	15	200k	RT	2.1	245	14.8	19.4	219	16.5	3.18	1.93	1.7	6.7
Si49	P5	79	700	15	200k	RT	2.9	166	16.6	21.6	210	15.7	3.38	1.93	3.2	14.6
Si50	P6	79	700	15	200k	RT	4.2	181	12.7	10.4	168	12.6	3.28	2.23	1.4	7.9
Si51	P7	79	700	15	200k	RT	5.4	174	17.3	15.9	141	10.6	3.50	1.64	1.8	14.5
Si52	P8	79	700	15	200k	RT	6.7	156	12.3	12.9	107	8.0	2.94	2.10	1.2	2.1
Si53	P9	79	700	15	200k	RT	8.4	144	11.4	18.2	102	7.7	3.04	2.22	2.0	5.8

Appendix C

Resources

I have utilised various digital resources for the work presented in this thesis as well as for the creation of the present document.

The formation of the PCI produced absorption signal, its detection and the functionality of the imaging stage were simulated using *Finesse* embedded in its *Python* wrapper *PyKat*. For that, the scientific environment *Spyder* was utilised. The correct lens positions and focal lengths in the Hamburg PCI system were calculated using *JamMT* by Nico Lastzka. For the evaluation of the absorption measurements, *MATLAB* by *MathWorks* in combination with a script written by Zeno Tornasi was used. The transmission spectra were analysed using *SCOUT* by *WTheiss Hardware and Software*. The microscopic images of the PLD produced aSi coatings were examined using *ImageJ* by the US-American *National Institutes of Health*. The general analysis of the coating data was carried out using *Excel* by *Microsoft*. For the design of the steel etching beaker, the 3D CAD software *Inventor* by *Autodesk* was used.

The various figures were produced utilising multiple resources. The PCI simulation figures were created using the *Python* package *matplotlib.pyplot*. The graphs presenting data were made using *Gnuplot* in combination with the *ConTEXT* editor to write and pass the scripts. The different schematic depictions were drawn using *Inkscape* in combination with a component library by Alexander Franzen, which was revised by Jan Gniesmer. *Inkscape* was also utilised to revise all other figures. Finally, the \LaTeX distribution *MiKTeX* in combination with the *TeXstudio* editor and a modified template from <http://www.LaTeXTemplates.com> was used for the creation of this document.

Bibliography

- [Abb16a] B. P. Abbott, R. Abbott, T. D. Abbott, M. R. Abernathy, F. Acernese *et al.* *GW150914: The Advanced LIGO Detectors in the Era of First Discoveries*. *Physical Review Letters* **116**, 131103 (2016).
URL <https://link.aps.org/doi/10.1103/PhysRevLett.116.131103>
- [Abb16b] B. P. Abbott, R. Abbott, T. D. Abbott, M. R. Abernathy, F. Acernese *et al.* *GW151226: Observation of Gravitational Waves from a 22-Solar-Mass Binary Black Hole Coalescence*. *Physical Review Letters* **116**, 241103 (2016).
URL <https://link.aps.org/doi/10.1103/PhysRevLett.116.241103>
- [Abb16c] B. P. Abbott, R. Abbott, T. D. Abbott, M. R. Abernathy, F. Acernese *et al.* *Observation of Gravitational Waves from a Binary Black Hole Merger*. *Physical Review Letters* **116**, 061102 (2016).
URL <https://link.aps.org/doi/10.1103/PhysRevLett.116.061102>
- [Abb17] B. P. Abbott, R. Abbott, T. D. Abbott, F. Acernese, K. Ackley *et al.* *A gravitational-wave standard siren measurement of the Hubble constant*. *Nature* **551** (7678), 85–88 (2017). ISSN 1476-4687.
URL <https://doi.org/10.1038/nature24471>
- [Abb19a] B. P. Abbott, R. Abbott, T. D. Abbott, S. Abraham, F. Acernese *et al.* *Binary Black Hole Population Properties Inferred from the First and Second Observing Runs of Advanced LIGO and Advanced Virgo*. *The Astrophysical Journal* **882** (2), L24 (2019).
URL <https://doi.org/10.3847/2041-8213/ab3800>
- [Abb19b] B. P. Abbott, R. Abbott, T. D. Abbott, S. Abraham, F. Acernese *et al.* *Tests of general relativity with the binary black hole signals from the LIGO-Virgo catalog GWTC-1*. *Physical Review D* **100**, 104036 (2019).
URL <https://link.aps.org/doi/10.1103/PhysRevD.100.104036>
- [Abb20] B. P. Abbott, R. Abbott, T. D. Abbott, S. Abraham, F. Acernese *et al.* *Prospects for observing and localizing gravitational-wave transients with Advanced LIGO, Advanced Virgo and KAGRA*. *Living Reviews In Relativity* **23**, 3 (2020).
URL <https://doi.org/10.1007/s41114-020-00026-9>
- [Abb21a] B. P. Abbott, R. Abbott, T. D. Abbott, S. Abraham, F. Acernese *et al.* *A Gravitational-wave Measurement of the Hubble Constant Following the Second Observing Run of Advanced LIGO and Virgo*. *The Astrophysical Journal* **909** (2), 218 (2021).

- URL <https://doi.org/10.3847/1538-4357/abdc7>
- [Abb21b] R. Abbott, T. Abbott, F. Acernese, K. Ackley, C. Adams *et al.* *GWTC-3: Compact Binary Coalescences Observed by LIGO and Virgo During the Second Part of the Third Observing Run*. arXiv preprint, arXiv:2111.03606 (2021).
URL <https://arxiv.org/abs/2111.03606>
- [Abb21c] R. Abbott, T. D. Abbott, S. Abraham, F. Acernese, K. Ackley *et al.* *Population Properties of Compact Objects from the Second LIGO–Virgo Gravitational-Wave Transient Catalog*. *The Astrophysical Journal Letters* **913** (1), L7 (2021).
URL <https://doi.org/10.3847/2041-8213/abe949>
- [Abb21d] R. Abbott, T. D. Abbott, S. Abraham, F. Acernese, K. Ackley *et al.* *Tests of general relativity with binary black holes from the second LIGO–Virgo gravitational-wave transient catalog*. *Physical Review D* **103**, 122002 (2021).
URL <https://link.aps.org/doi/10.1103/PhysRevD.103.122002>
- [Abb22] R. Abbott, H. Abe, F. Acernese, K. Ackley, N. Adhikari *et al.* *First joint observation by the underground gravitational-wave detector KAGRA with GEO 600*. *Progress of Theoretical and Experimental Physics* **2022** (6) (2022). ISSN 2050-3911. 063F01.
URL <https://doi.org/10.1093/ptep/ptac073>
- [Abe11a] M. Abernathy, F. Acernese, P. Ajith, B. Allen, P. Amaro Seoane *et al.* *Einstein gravitational wave Telescope conceptual design study*. EGO (2011).
URL <https://art.torvergata.it/handle/2108/102907>
- [Abe11b] M. R. Abernathy, S. Reid, E. Chalkley, R. Bassiri, I. W. Martin *et al.* *Cryogenic mechanical loss measurements of heat-treated hafnium dioxide*. *Classical and Quantum Gravity* **28** (19), 195017 (2011).
URL <https://doi.org/10.1088/0264-9381/28/19/195017>
- [Abe21] M. Abernathy, A. Amato, A. Ananyeva, S. Angelova, B. Baloukas *et al.* *Exploration of co-sputtered Ta₂O₅–ZrO₂ thin films for gravitational-wave detectors*. *Classical and Quantum Gravity* **38** (19), 195021 (2021).
URL <https://doi.org/10.1088/1361-6382/ac1b06>
- [Acc11] T. Accadia, F. Acernese, F. Antonucci, P. Astone, G. Ballardin *et al.* *Status of the Virgo project*. *Classical and Quantum Gravity* **28** (11), 114002 (2011).
URL <https://doi.org/10.1088/0264-9381/28/11/114002>
- [Ace14] F. Acernese, M. Agathos, K. Agatsuma, D. Aisa, N. Allemandou *et al.* *Advanced Virgo: a second-generation interferometric gravitational wave detector*. *Classical and Quantum Gravity* **32** (2), 024001 (2014).
URL <https://doi.org/10.1088/0264-9381/32/2/024001>
- [Adh20] R. X. Adhikari, K. Arai, A. F. Brooks, C. Wipf, O. Aguiar *et al.* *A cryogenic silicon interferometer for gravitational-wave detection*. *Classical and Quantum Gravity*

- 37 (16), 165003 (2020).
URL <https://doi.org/10.1088/1361-6382/ab9143>
- [Aff14] C. Affeldt, K. Danzmann, K. L. Dooley, H. Grote, M. Hewitson *et al.* *Advanced techniques in GEO 600*. *Classical and Quantum Gravity* **31** (22), 224002 (2014).
URL <https://doi.org/10.1088/0264-9381/31/22/224002>
- [Agr06] J. Agresti, G. Castaldi, R. DeSalvo, V. Galdi, V. Pierro *et al.* *Optimized multilayer dielectric mirror coatings for gravitational wave interferometers*. In: M. J. Ellison (editor), *Advances in Thin-Film Coatings for Optical Applications III*. International Society for Optics and Photonics (SPIE, 2006), volume 6286, 62 – 71.
URL <https://doi.org/10.1117/12.678977>
- [Aie19] L. Aiello, E. Cesarini, V. Fafone, M. Lorenzini, Y. Minenkov, I. Nardecchia, A. Rocchi, and V. Sequino. *Thermal compensation system in advanced and third generation gravitational wave interferometric detectors*. *Journal of Physics: Conference Series* **1226** (1), 012019 (2019).
URL <https://doi.org/10.1088/1742-6596/1226/1/012019>
- [Ale09] A. Alexandrovski, M. Fejer, A. Markosian, and R. Route. *Photothermal common-path interferometry (PCI): new developments*. In: W. A. Clarkson, N. Hodgson, and R. K. Shori (editors), *Solid State Lasers XVIII: Technology and Devices*. International Society for Optics and Photonics (SPIE, 2009), volume 7193, 79 – 91.
URL <https://doi.org/10.1117/12.814813>
- [AS17] P. Amaro-Seoane, H. Audley, S. Babak, J. Baker, E. Barausse *et al.* *Laser interferometer space antenna*. arXiv preprint, arXiv:1702.00786 (2017).
URL <https://arxiv.org/abs/1702.00786>
- [Aso13] Y. Aso, Y. Michimura, K. Somiya, M. Ando, O. Miyakawa *et al.* *Interferometer design of the KAGRA gravitational wave detector*. *Physical Review D* **88**, 043007 (2013).
URL <https://link.aps.org/doi/10.1103/PhysRevD.88.043007>
- [Ast12] S. M. Aston, M. A. Barton, A. S. Bell, N. Beveridge, B. Bland *et al.* *Update on quadruple suspension design for Advanced LIGO*. *Classical and Quantum Gravity* **29** (23), 235004 (2012).
URL <https://doi.org/10.1088/0264-9381/29/23/235004>
- [Axm18] D. Axmann. *Herstellung und Charakterisierung von Nanoschichten für zukünftige Spiegel von Gravitationswellendetektoren*. Bachelor thesis, Universität Hamburg (2018).
- [Bad21] M. Bader. *Seismic and Newtonian noise modeling for Advanced Virgo and Einstein Telescope*. Ph.D. thesis, Vrije Universiteit Amsterdam (2021).
- [Bar94] Š. Barta. *Effective Young's modulus and Poisson's ratio for the particulate composite*. *Journal of Applied Physics* **75** (7), 3258–3263 (1994).
URL <https://doi.org/10.1063/1.356132>

- [Bar18] L. Barsotti, S. Gras, M. Evans, and P. Fritschel. *The updated Advanced LIGO design curve*. LIGO Scientific Collaboration, technical note, LIGO-T1800044-v5 (2018).
URL <https://dcc.ligo.org/LIGO-T1800044/public>
- [Bar19] B. C. Barish. *LIGO and Gravitational Waves II: Nobel Lecture, December 8, 2017*. *Annalen der Physik* **531** (1), 1800357 (2019).
URL <https://onlinelibrary.wiley.com/doi/abs/10.1002/andp.201800357>
- [Beh18] M. Behrendsen. *Variation von Herstellungsparametern von Spiegelschichten in Bezug auf Gravitationswellendetektoren*. Bachelor thesis, Universität Hamburg (2018).
- [Beh21] M. Behrendsen. *Herstellung und Analyse von Spiegelschichten mittels Laserstrahlverdampfen im Bezug auf Gravitationswellendetektoren*. Master thesis, Universität Hamburg (2021).
- [Bek12] M. G. Beker, J. F. J. van den Brand, E. Hennes, and D. S. Rabeling. *Newtonian noise and ambient ground motion for gravitational wave detectors*. *Journal of Physics: Conference Series* **363**, 012004 (2012).
URL <https://doi.org/10.1088/1742-6596/363/1/012004>
- [Bir18] R. Birney, J. Steinlechner, Z. Tornasi, S. MacFoy, D. Vine *et al.* *Amorphous Silicon with Extremely Low Absorption: Beating Thermal Noise in Gravitational Astronomy*. *Physical Review Letters* **121**, 191101 (2018).
URL <https://link.aps.org/doi/10.1103/PhysRevLett.121.191101>
- [Bro16] A. F. Brooks, B. Abbott, M. A. Arain, G. Ciani, A. Cole *et al.* *Overview of Advanced LIGO adaptive optics*. *Applied Optics* **55** (29), 8256–8265 (2016).
URL <http://opg.optica.org/ao/abstract.cfm?URI=ao-55-29-8256>
- [Car80] W. H. Carter. *Spot size and divergence for Hermite Gaussian beams of any order*. *Applied Optics* **19** (7), 1027–1029 (1980).
URL <http://opg.optica.org/ao/abstract.cfm?URI=ao-19-7-1027>
- [Che02] A.-C. Cheung, T. Ma, and H. Chen. *High-resolution cavity enhanced absorption spectroscopy using an optical cavity with ultra-high reflectivity mirrors*. *Chemical Physics Letters* **353** (3), 275–280 (2002). ISSN 0009-2614.
URL [https://doi.org/10.1016/S0009-2614\(02\)00035-0](https://doi.org/10.1016/S0009-2614(02)00035-0)
- [Col13] G. D. Cole, W. Zhang, M. J. Martin, J. Ye, and M. Aspelmeyer. *Tenfold reduction of Brownian noise in high-reflectivity optical coatings*. *Nature Photonics* **7** (8), 644–650 (2013). ISSN 1749-4893.
URL <https://doi.org/10.1038/nphoton.2013.174>
- [Col16] G. D. Cole, W. Zhang, B. J. Bjork, D. Follman, P. Heu *et al.* *High-performance near- and mid-infrared crystalline coatings*. *Optica* **3** (6), 647–656 (2016).
URL <http://opg.optica.org/optica/abstract.cfm?URI=optica-3-6-647>

- [Cra19] K. Craig, J. Steinlechner, P. G. Murray, A. S. Bell, R. Birney *et al.* *Mirror Coating Solution for the Cryogenic Einstein Telescope*. *Physical Review Letters* **122**, 231102 (2019).
URL <https://link.aps.org/doi/10.1103/PhysRevLett.122.231102>
- [Cum13] A. V. Cumming, L. Cunningham, G. D. Hammond, K. Haughian, J. Hough *et al.* *Silicon mirror suspensions for gravitational wave detectors*. *Classical and Quantum Gravity* **31** (2), 025017 (2013).
URL <https://doi.org/10.1088/0264-9381/31/2/025017>
- [Cum21] R. B. Cummings, R. Bassiri, I. W. Martin, and I. MacLaren. *Argon bubble formation in tantalum oxide-based films for gravitational wave interferometer mirrors*. *Optical Materials Express* **11** (3), 707–718 (2021).
URL <http://opg.optica.org/ome/abstract.cfm?URI=ome-11-3-707>
- [Deg13] J. Degallaix, R. Flaminio, D. Forest, M. Granata, C. Michel *et al.* *Bulk optical absorption of high resistivity silicon at 1550 nm*. *Optics Letters* **38** (12), 2047–2049 (2013).
URL <http://opg.optica.org/ol/abstract.cfm?URI=ol-38-12-2047>
- [Dem09] W. Demtröder. *Experimentalphysik 2: Elektrizität und Optik*. Springer-Lehrbuch (Springer Berlin Heidelberg, 2009). ISBN 978-3-540-68210-3. 5. edition.
URL <https://link.springer.com/book/10.1007%2F978-3-540-68219-6>
- [DF20] C. Darsow-Fromm, M. Schröder, J. Gurs, R. Schnabel, and S. Steinlechner. *Highly efficient generation of coherent light at 2128 nm via degenerate optical-parametric oscillation*. *Optics Letters* **45** (22), 6194–6197 (2020).
URL <http://opg.optica.org/ol/abstract.cfm?URI=ol-45-22-6194>
- [EA16] A. A. El-Amin and A. Solieman. *Influence of Heat Treatment on the Optical Properties of Thermal Evaporated SnO₂ Thin Films*. *Silicon* **8** (4), 517–523 (2016). ISSN 1876-9918.
URL <https://doi.org/10.1007/s12633-014-9250-y>
- [Eas07] R. Eason. *Pulsed laser deposition of thin films: applications-led growth of functional materials* (John Wiley & Sons, 2007).
- [Ein16a] A. Einstein. *Die Grundlage der allgemeinen Relativitätstheorie*. *Annalen der Physik* **49**, 769–822 (1916).
URL <https://onlinelibrary.wiley.com/doi/10.1002/andp.2005517S151>
- [Ein16b] A. Einstein. *Näherungsweise Integration der Feldgleichungen der Gravitation*. *Sitzungsberichte der Königlich Preußischen Akademie der Wissenschaften* **1**, 688–696 (1916).
URL <https://onlinelibrary.wiley.com/doi/abs/10.1002/3527608958.ch7>
- [Erm84] M. Erman, J. B. Theeten, P. Chambon, S. M. Kelso, and D. E. Aspnes. *Optical properties and damage analysis of GaAs single crystals partly amorphized by ion implantation*. *Journal of Applied Physics* **56** (10), 2664–2671 (1984).

- URL <https://doi.org/10.1063/1.333785>
- [Eva08] M. Evans, S. Ballmer, M. Fejer, P. Fritschel, G. Harry *et al.* *Thermo-optic noise in coated mirrors for high-precision optical measurements*. *Physical Review D* **78**, 102003 (2008).
URL <https://link.aps.org/doi/10.1103/PhysRevD.78.102003>
- [Fab00] F. Fabbri, G. Padeletti, T. Petrisor, G. Celentano, and V. Boffa. *Surface morphology of pulsed laser deposited $YBa_2Cu_3O_{7-\delta}$ and $NdBa_2Cu_3O_{7-\delta}$ thin films on $SrTiO_3$ substrates*. *Superconductor Science and Technology* **13** (10), 1492–1498 (2000).
URL <https://doi.org/10.1088/0953-2048/13/10/315>
- [Fen01] S. Feng and H. G. Winful. *Physical origin of the Gouy phase shift*. *Optics Letters* **26** (8), 485–487 (2001).
URL <http://opg.optica.org/ol/abstract.cfm?URI=ol-26-8-485>
- [Fla05] É. É. Flanagan and S. A. Hughes. *The basics of gravitational wave theory*. *New Journal of Physics* **7**, 204–204 (2005).
URL <https://doi.org/10.1088/1367-2630/7/1/204>
- [Fla10] R. Flaminio, J. Franc, C. Michel, N. Morgado, L. Pinard *et al.* *A study of coating mechanical and optical losses in view of reducing mirror thermal noise in gravitational wave detectors*. *Classical and Quantum Gravity* **27** (8), 084030 (2010).
URL <https://doi.org/10.1088/0264-9381/27/8/084030>
- [Fre82] J. E. Fredrickson, C. N. Waddell, W. G. Spitzer, and G. K. Hubler. *Effects of thermal annealing on the refractive index of amorphous silicon produced by ion implantation*. *Applied Physics Letters* **40** (2), 172–174 (1982).
URL <https://doi.org/10.1063/1.93032>
- [Gao12] L. Gao, F. Lemarchand, and M. Lequime. *Exploitation of multiple incidences spectro-metric measurements for thin film reverse engineering*. *Optics Express* **20** (14), 15734–15751 (2012).
URL <http://opg.optica.org/oe/abstract.cfm?URI=oe-20-14-15734>
- [Gir01] P. K. Giri, S. Tripurasundari, G. Raghavan, B. K. Panigrahi, P. Magudapathy *et al.* *Crystalline to amorphous transition and band structure evolution in ion-damaged silicon studied by spectroscopic ellipsometry*. *Journal of Applied Physics* **90** (2), 659–669 (2001).
URL <https://doi.org/10.1063/1.1379055>
- [Gon00] G. González. *Suspensions thermal noise in the LIGO gravitational wave detector*. *Classical and Quantum Gravity* **17** (21), 4409–4435 (2000).
URL <https://doi.org/10.1088/0264-9381/17/21/305>
- [Gra20a] M. Granata, A. Amato, L. Balzarini, M. Canepa, J. Degallaix *et al.* *Amorphous optical coatings of present gravitational-wave interferometers*. *Classical and Quantum*

- Gravity **37** (9), 095004 (2020).
URL <https://doi.org/10.1088/1361-6382/ab77e9>
- [Gra20b] M. Granata, A. Amato, G. Cagnoli, M. Coulon, J. Degallaix *et al.* *Progress in the measurement and reduction of thermal noise in optical coatings for gravitational-wave detectors*. *Applied Optics* **59** (5), A229–A235 (2020).
URL <http://opg.optica.org/ao/abstract.cfm?URI=ao-59-5-A229>
- [Gre13] J. A. Greer. *History and current status of commercial pulsed laser deposition equipment*. *Journal of Physics D: Applied Physics* **47** (3), 034005 (2013).
URL <https://doi.org/10.1088/0022-3727/47/3/034005>
- [Gro10] H. Grote. *The GEO 600 status*. *Classical And Quantum Gravity* **27** (8), 084003 (2010).
URL <https://doi.org/10.1088/0264-9381/27/8/084003>
- [Hai06] A. Haija, W. L. Freeman, and T. Roarty. *Effective characteristic matrix of ultrathin multilayer structures*. *Optica Applicata* **36** (1), 39–50 (2006).
URL <https://opticaapplicata.pwr.edu.pl/article.php?id=2006100039>
- [Hal21] E. D. Hall, K. Kuns, J. R. Smith, Y. Bai, C. Wipf *et al.* *Gravitational-wave physics with Cosmic Explorer: Limits to low-frequency sensitivity*. *Physical Review D* **103**, 122004 (2021).
URL <https://link.aps.org/doi/10.1103/PhysRevD.103.122004>
- [Har06] G. M. Harry, H. Armandula, E. Black, D. R. M. Crooks, G. Cagnoli *et al.* *Thermal noise from optical coatings in gravitational wave detectors*. *Applied Optics* **45** (7), 1569–1574 (2006).
URL <http://opg.optica.org/ao/abstract.cfm?URI=ao-45-7-1569>
- [Har12] G. Harry, T. Bodiya, and R. DeSalvo. *Optical Coatings and Thermal Noise in Precision Measurement* (Cambridge University Press, 2012). ISBN 978-1-107-00338-5.
URL <https://www.doi.org/10.1017/CB09780511762314>
- [Hei14] D. Heinert, K. Craig, H. Grote, S. Hild, H. Lück, and others. *Thermal noise of folding mirrors*. *Physical Review D* **90**, 042001 (2014).
URL <https://link.aps.org/doi/10.1103/PhysRevD.90.042001>
- [Hon13] T. Hong, H. Yang, E. K. Gustafson, R. X. Adhikari, and Y. Chen. *Brownian thermal noise in multilayer coated mirrors*. *Physical Review D* **87**, 082001 (2013).
URL <https://link.aps.org/doi/10.1103/PhysRevD.87.082001>
- [How87] D. G. Howitt and A. B. Harker. *The oriented growth of anatase in thin films of amorphous titania*. *Journal of Materials Research* **2** (2), 201–210 (1987).
URL <https://www.doi.org/10.1557/JMR.1987.0201>
- [Jac82] W. B. Jackson and N. M. Amer. *Direct measurement of gap-state absorption in hydrogenated amorphous silicon by photothermal deflection spectroscopy*. *Physical Review B*

- 25, 5559–5562 (1982).
URL <https://link.aps.org/doi/10.1103/PhysRevB.25.5559>
- [Jel92] G. Jellison. *Optical functions of silicon determined by two-channel polarization modulation ellipsometry*. *Optical Materials* **1** (1), 41–47 (1992). ISSN 0925-3467.
URL [https://doi.org/10.1016/0925-3467\(92\)90015-F](https://doi.org/10.1016/0925-3467(92)90015-F)
- [Jon75] R. Jones. *Mechanics of composite materials* (Scripta Book Co., 1975).
URL <https://doi.org/10.1201/9781498711067>
- [Kä97] F. X. Kärtner, N. Matuschek, T. Schibli, U. Keller, H. A. Haus *et al.* *Design and fabrication of double-chirped mirrors*. *Optics Letters* **22** (11), 831–833 (1997).
URL <http://www.osapublishing.org/ol/abstract.cfm?URI=ol-22-11-831>
- [Kee95] M. J. Keevers and M. A. Green. *Absorption edge of silicon from solar cell spectral response measurements*. *Applied Physics Letters* **66** (2), 174–176 (1995).
URL <https://doi.org/10.1063/1.113125>
- [Koc19] P. Koch, G. D. Cole, C. Deutsch, D. Follman, P. Heu *et al.* *Thickness uniformity measurements and damage threshold tests of large-area GaAs/AlGaAs crystalline coatings for precision interferometry*. *Optics Express* **27** (25), 36731–36740 (2019).
URL <http://opg.optica.org/oe/abstract.cfm?URI=oe-27-25-36731>
- [Kon11] N. M. Kondratiev, A. G. Gurkovsky, and M. L. Gorodetsky. *Thermal noise and coating optimization in multilayer dielectric mirrors*. *Physical Review D* **84**, 022001 (2011).
URL <https://link.aps.org/doi/10.1103/PhysRevD.84.022001>
- [Kre03] H.-U. Krebs, M. Weisheit, J. Faupel, E. Süske, T. Scharf *et al.* *Pulsed Laser Deposition (PLD) – A Versatile Thin Film Technique*. In: B. Kramer (editor), *Advances in Solid State Physics* (Springer Berlin Heidelberg, Berlin, Heidelberg, 2003), 505–518. ISBN 978-3-540-44838-9.
URL https://doi.org/10.1007/978-3-540-44838-9_36
- [Kub66] R. Kubo. *The fluctuation-dissipation theorem*. *Reports on Progress in Physics* **29** (1), 255–284 (1966).
URL <https://doi.org/10.1088/0034-4885/29/1/306>
- [Kuo19] L.-C. Kuo, H.-W. Pan, C.-L. Chang, and S. Chao. *Low cryogenic mechanical loss composite silica thin film for low thermal noise dielectric mirror coatings*. *Optics Letters* **44** (2), 247–250 (2019).
URL <http://opg.optica.org/ol/abstract.cfm?URI=ol-44-2-247>
- [Lal21] É. Lalande, A. W. Lussier, C. Lévesque, M. Ward, B. Baloukas *et al.* *Zirconia-titania-doped tantala optical coatings for low mechanical loss Bragg mirrors*. *Journal of Vacuum Science & Technology A* **39** (4), 043416 (2021).
URL <https://doi.org/10.1116/6.0001074>

- [Lei15] M. Leidinger, S. Fieberg, N. Waasem, F. Kühnemann, K. Buse *et al.* *Comparative study on three highly sensitive absorption measurement techniques characterizing lithium niobate over its entire transparent spectral range.* *Optics Express* **23** (17), 21690–21705 (2015).
URL <http://opg.optica.org/oe/abstract.cfm?URI=oe-23-17-21690>
- [Li80] H. H. Li. *Refractive index of silicon and germanium and its wavelength and temperature derivatives.* *Journal of Physical and Chemical Reference Data* **9** (3), 561–658 (1980).
URL <https://doi.org/10.1063/1.555624>
- [LIG] LIGO Laboratory. *LIGO R&D - Parametric Instabilities.* <https://www.ligo.caltech.edu/page/research-development>. Online; accessed 8-July-2022.
- [Liu14] X. Liu, D. R. Queen, T. H. Metcalf, J. E. Karel, and F. Hellman. *Hydrogen-Free Amorphous Silicon with No Tunneling States.* *Physical Review Letters* **113**, 025503 (2014).
URL <https://link.aps.org/doi/10.1103/PhysRevLett.113.025503>
- [Lou03] R. Loudon. *The quantum theory of light* (OUP Oxford, 2003). ISBN 0-19-850177-3. 3. edition.
- [Lou21] J. Lough, E. Schreiber, F. Bergamin, H. Grote, M. Mehmet *et al.* *First Demonstration of 6 dB Quantum Noise Reduction in a Kilometer Scale Gravitational Wave Observatory.* *Physical Review Letters* **126**, 041102 (2021).
URL <https://link.aps.org/doi/10.1103/PhysRevLett.126.041102>
- [Luc05] V. Lucarini, J. J. Saarinen, K.-E. Peiponen, and E. M. Vartiainen. *Kramers-Kronig relations in optical materials research*, volume 110 (Springer Science & Business Media, 2005).
URL <https://doi.org/10.1007/b138913>
- [Mal65] I. H. Malitson. *Interspecimen Comparison of the Refractive Index of Fused Silica.* *Journal Of The Optical Society Of America* **55** (10), 1205–1209 (1965).
URL <http://opg.optica.org/abstract.cfm?URI=josa-55-10-1205>
- [Mar08] I. Martin, H. Armandula, C. Comtet, M. M. Fejer, A. Gretarsson *et al.* *Measurements of a low-temperature mechanical dissipation peak in a single layer of Ta₂O₅ doped with TiO₂.* *Classical and Quantum Gravity* **25** (5), 055005 (2008).
URL <https://doi.org/10.1088/0264-9381/25/5/055005>
- [Mar09] I. W. Martin, E. Chalkley, R. Nawrodt, H. Armandula, R. Bassiri *et al.* *Comparison of the temperature dependence of the mechanical dissipation in thin films of Ta₂O₅ and Ta₂O₅ doped with TiO₂.* *Classical and Quantum Gravity* **26** (15), 155012 (2009).
URL <https://doi.org/10.1088/0264-9381/26/15/155012>
- [Mar10] I. W. Martin, R. Bassiri, R. Nawrodt, M. M. Fejer, A. Gretarsson *et al.* *Effect of heat treatment on mechanical dissipation in Ta₂O₅ coatings.* *Classical and Quantum*

- Gravity **27** (22), 225020 (2010).
URL <https://doi.org/10.1088/0264-9381/27/22/225020>
- [Mar12] I. Martin and S. Reid. *Coating thermal noise*. In: G. Harry, T. P. Bodiya, and R. DeSalvo (editors), *Optical Coatings and Thermal Noise in Precision Measurement* (Cambridge University Press, 2012), 31–54.
URL <https://doi.org/10.1017/CB09780511762314.006>
- [Mar14] I. W. Martin, R. Nawrodt, K. Craig, C. Schwarz, R. Bassiri *et al.* *Low temperature mechanical dissipation of an ion-beam sputtered silica film*. *Classical and Quantum Gravity* **31** (3), 035019 (2014).
URL <https://doi.org/10.1088/0264-9381/31/3/035019>
- [Mar16] D. V. Martynov, E. D. Hall, B. P. Abbott, R. Abbott, T. D. Abbott *et al.* *Sensitivity of the Advanced LIGO detectors at the beginning of gravitational wave astronomy*. *Physical Review D* **93**, 112004 (2016).
URL <https://link.aps.org/doi/10.1103/PhysRevD.93.112004>
- [Mar18] M. Marchiò, R. Flaminio, L. Pinard, D. Forest, C. Deutsch *et al.* *Optical performance of large-area crystalline coatings*. *Optics Express* **26** (5), 6114–6125 (2018).
URL <http://opg.optica.org/oe/abstract.cfm?URI=oe-26-5-6114>
- [Mat15] F. Matichard, B. Lantz, R. Mittleman, K. Mason, J. Kissel *et al.* *Seismic isolation of Advanced LIGO: Review of strategy, instrumentation and performance*. *Classical and Quantum Gravity* **32** (18), 185003 (2015).
URL <https://doi.org/10.1088/0264-9381/32/18/185003>
- [McG78] D. F. McGuigan, C. C. Lam, R. Q. Gram, A. W. Hoffman, D. H. Douglass *et al.* *Measurements of the mechanical Q of single-crystal silicon at low temperatures*. *Journal of Low Temperature Physics* **30** (5), 621–629 (1978). ISSN 1573-7357.
URL <https://doi.org/10.1007/BF00116202>
- [MR21] M. Molina-Ruiz, Y. J. Rosen, H. C. Jacks, M. R. Abernathy, T. H. Metcalf *et al.* *Origin of mechanical and dielectric losses from two-level systems in amorphous silicon*. *Physical Review Materials* **5**, 035601 (2021).
URL <https://link.aps.org/doi/10.1103/PhysRevMaterials.5.035601>
- [Mur15] P. G. Murray, I. W. Martin, K. Craig, J. Hough, R. Robie *et al.* *Ion-beam sputtered amorphous silicon films for cryogenic precision measurement systems*. *Physical Review D* **92**, 062001 (2015).
URL <https://link.aps.org/doi/10.1103/PhysRevD.92.062001>
- [Mus18] N. Musila, M. Munji, J. Simiyu, E. Masika, and R. Nyenge. *Optical Properties and Analysis of OJL Model's Electronic inter-band Transition Parameters of TiO₂ Films*. *Path of Science* **4** (7), 3001–3012 (2018). ISSN 2413-9009.
URL <https://pathofscience.org/index.php/ps/article/view/528>

- [Nak93] S. Nakashima and K. Izumi. *Analysis of buried oxide layer formation and mechanism of threading dislocation generation in the substoichiometric oxygen dose region*. Journal of Materials Research **8** (3), 523–534 (1993).
URL <https://doi.org/10.1557/JMR.1993.0523>
- [Naw08] R. Nawrodt, A. Zimmer, T. Koettig, C. Schwarz, D. Heinert *et al.* *High mechanical Q-factor measurements on silicon bulk samples*. Journal of Physics: Conference Series **122**, 012008 (2008).
URL <https://doi.org/10.1088/1742-6596/122/1/012008>
- [Oha86] H. Ohashi, J. Ohura, T. Tsukakoshi, and M. Simbo. *Improved dielectrically isolated device integration by silicon-wafer direct bonding(SDB) technique*. In: *1986 International Electron Devices Meeting* (1986), 210–213.
URL <https://doi.org/10.1109/IEDM.1986.191151>
- [O’L97] S. K. O’Leary, S. R. Johnson, and P. K. Lim. *The relationship between the distribution of electronic states and the optical absorption spectrum of an amorphous semiconductor: An empirical analysis*. Journal of Applied Physics **82** (7), 3334–3340 (1997).
URL <https://doi.org/10.1063/1.365643>
- [Pan14] H.-W. Pan, S.-J. Wang, L.-C. Kuo, S. Chao, M. Principe *et al.* *Thickness-dependent crystallization on thermal anneal for titania/silica nm-layer composites deposited by ion beam sputter method*. Optics Express **22** (24), 29847–29854 (2014).
URL <http://opg.optica.org/oe/abstract.cfm?URI=oe-22-24-29847>
- [Pan18a] H.-W. Pan, L.-C. Kuo, L.-A. Chang, S. Chao, I. W. Martin *et al.* *Silicon nitride and silica quarter-wave stacks for low-thermal-noise mirror coatings*. Physical Review D **98**, 102001 (2018).
URL <https://link.aps.org/doi/10.1103/PhysRevD.98.102001>
- [Pan18b] H.-W. Pan, L.-C. Kuo, S.-Y. Huang, M.-Y. Wu, Y.-H. Juang *et al.* *Silicon nitride films fabricated by a plasma-enhanced chemical vapor deposition method for coatings of the laser interferometer gravitational wave detector*. Physical Review D **97**, 022004 (2018).
URL <https://link.aps.org/doi/10.1103/PhysRevD.97.022004>
- [Pei19] F. Pein. *Siliziumbeschichtungen für Gravitationswellendetektoren*. Bachelor thesis, Universität Hamburg (2019).
- [Pen10] S. Penn, J. Podkaminer, J. Luo, C. Luongo, and S. Kipperman. *Recent Measurements of Mechanical Loss for aLIGO Coating Research* (2010). LSC-Virgo Mar 2010 Meeting.
URL <https://dcc.ligo.org/LIGO-G1000356>
- [Pie72] D. T. Pierce and W. E. Spicer. *Electronic Structure of Amorphous Si from Photoemission and Optical Studies*. Physical Review B **5**, 3017–3029 (1972).
URL <https://link.aps.org/doi/10.1103/PhysRevB.5.3017>

- [Pin17] L. Pinard, C. Michel, B. Sassolas, L. Balzarini, J. Degallaix *et al.* *Mirrors used in the LIGO interferometers for first detection of gravitational waves*. *Applied Optics* **56** (4), C11–C15 (2017).
URL <http://opg.optica.org/ao/abstract.cfm?URI=ao-56-4-C11>
- [Pra19] K. Prasai, J. Jiang, A. Mishkin, B. Shyam, S. Angelova *et al.* *High Precision Detection of Change in Intermediate Range Order of Amorphous Zirconia-Doped Tantalum Thin Films Due to Annealing*. *Physical Review Letters* **123**, 045501 (2019).
URL <https://link.aps.org/doi/10.1103/PhysRevLett.123.045501>
- [Rau95] S. Rau, C. Enss, S. Hunklinger, P. Neu, and A. Würger. *Acoustic properties of oxide glasses at low temperatures*. *Physical Review B* **52**, 7179–7194 (1995).
URL <https://link.aps.org/doi/10.1103/PhysRevB.52.7179>
- [Rau07] C. Rauscher, V. Janssen, and R. Minihold. *Fundamentals of Spectrum Analysis* (Rohde & Schwarz, 2007). ISBN 9783939837015.
- [Rei16] S. Reid and I. W. Martin. *Development of Mirror Coatings for Gravitational Wave Detectors*. *Coatings* **6** (4) (2016). ISSN 2079-6412.
URL <https://www.mdpi.com/2079-6412/6/4/61>
- [Rei19] D. Reitze, R. X. Adhikari, S. Ballmer, B. Barish, L. Barsotti *et al.* *Cosmic explorer: the US contribution to gravitational-wave astronomy beyond LIGO*. arXiv preprint, arXiv:1907.04833 (2019).
URL <https://arxiv.org/abs/1907.04833>
- [Rob18] R. Robie. *Characterisation of the mechanical properties of thin-film mirror coating materials for use in future interferometric gravitational wave detectors*. Dissertation, University of Glasgow (2018).
URL <https://theses.gla.ac.uk/30645>
- [Sat17] S. Sato, S. Kawamura, M. Ando, T. Nakamura, K. Tsubono *et al.* *The status of DECIGO*. *Journal of Physics: Conference Series* **840**, 012010 (2017).
URL <https://doi.org/10.1088/1742-6596/840/1/012010>
- [Sau90] P. R. Saulson. *Thermal noise in mechanical experiments*. *Physical Review D* **42**, 2437–2445 (1990).
URL <https://link.aps.org/doi/10.1103/PhysRevD.42.2437>
- [Sch09] J. Schou. *Physical aspects of the pulsed laser deposition technique: The stoichiometric transfer of material from target to film*. *Applied Surface Science* **255** (10), 5191 – 5198 (2009). ISSN 0169-4332.
URL <https://doi.org/10.1016/j.apsusc.2008.10.101>
- [Sch17] R. Schnabel. *Squeezed states of light and their applications in laser interferometers*. *Physics Reports* **684**, 1–51 (2017). ISSN 0370-1573.
URL <https://doi.org/10.1016/j.physrep.2017.04.001>

- [Sei90] H. Seidel, L. Csepregi, A. Heuberger, and H. Baumgärtel. *Anisotropic Etching of Crystalline Silicon in Alkaline Solutions: I. Orientation Dependence and Behavior of Passivation Layers*. *Journal Of The Electrochemical Society* **137** (11), 3612–3626 (1990).
URL <https://doi.org/10.1149/1.2086277>
- [Sha17] B. Shapiro, R. X. Adhikari, O. Aguiar, E. Bonilla, D. Fan *et al.* *Cryogenically cooled ultra low vibration silicon mirrors for gravitational wave observatories*. *Cryogenics* **81**, 83–92 (2017). ISSN 0011-2275.
URL <https://doi.org/10.1016/j.cryogenics.2016.12.004>
- [Sol10] A. Solieman and A. Abu-Sehly. *Modelling of optical properties of amorphous selenium thin films*. *Physica B: Condensed Matter* **405** (4), 1101–1107 (2010). ISSN 0921-4526.
URL <https://doi.org/10.1016/j.physb.2009.11.014>
- [Som12] K. Somiya. *Detector configuration of KAGRA—the Japanese cryogenic gravitational-wave detector*. *Classical and Quantum Gravity* **29** (12), 124007 (2012).
URL <https://doi.org/10.1088/0264-9381/29/12/124007>
- [SS19] M. Soares-Santos, A. Palmese, W. Hartley, J. Annis, J. Garcia-Bellido *et al.* *First Measurement of the Hubble Constant from a Dark Standard Siren using the Dark Energy Survey Galaxies and the LIGO/Virgo Binary–Black-hole Merger GW170814*. *The Astrophysical Journal* **876** (1), L7 (2019).
URL <https://doi.org/10.3847/2041-8213/ab14f1>
- [Sta21] Stanford Photo-Thermal Solutions Team. *PCI software Version 7.6.2 Manual*. Stanford Photo-Thermal Solutions, Pahoah, Hawaii, USA (2021).
URL <https://www.stan-pts.com>
- [Ste15] J. Steinlechner, I. W. Martin, J. Hough, C. Krüger, S. Rowan *et al.* *Thermal noise reduction and absorption optimization via multimaterial coatings*. *Physical Review D* **91**, 042001 (2015).
URL <https://link.aps.org/doi/10.1103/PhysRevD.91.042001>
- [Ste16a] J. Steinlechner and I. W. Martin. *High index top layer for multimaterial coatings*. *Physical Review D* **93**, 102001 (2016).
URL <https://link.aps.org/doi/10.1103/PhysRevD.93.102001>
- [Ste16b] J. Steinlechner, I. W. Martin, R. Bassiri, A. Bell, M. M. Fejer *et al.* *Optical absorption of ion-beam sputtered amorphous silicon coatings*. *Physical Review D* **93**, 062005 (2016).
URL <https://link.aps.org/doi/10.1103/PhysRevD.93.062005>
- [Ste17] J. Steinlechner, C. Krüger, I. W. Martin, A. Bell, J. Hough *et al.* *Optical absorption of silicon nitride membranes at 1064 nm and at 1550 nm*. *Physical Review D* **96**, 022007 (2017).
URL <https://link.aps.org/doi/10.1103/PhysRevD.96.022007>

- [Ste18a] J. Steinlechner. *Development of mirror coatings for gravitational-wave detectors*. Philosophical Transactions of the Royal Society A: Mathematical, Physical and Engineering Sciences **376** (2120), 20170282 (2018).
URL <https://doi.org/10.1098/rsta.2017.0282>
- [Ste18b] J. Steinlechner, I. W. Martin, A. S. Bell, J. Hough, M. Fletcher *et al.* *Silicon-Based Optical Mirror Coatings for Ultrahigh Precision Metrology and Sensing*. Physical Review Letters **120**, 263602 (2018).
URL <https://link.aps.org/doi/10.1103/PhysRevLett.120.263602>
- [Ste21] J. Steinlechner and I. W. Martin. *How can amorphous silicon improve current gravitational-wave detectors?* Physical Review D **103**, 042001 (2021).
URL <https://link.aps.org/doi/10.1103/PhysRevD.103.042001>
- [Tai20] S. C. Tait, J. Steinlechner, M. M. Kinley-Hanlon, P. G. Murray, J. Hough, *et al.* *Demonstration of the Multimaterial Coating Concept to Reduce Thermal Noise in Gravitational-Wave Detectors*. Physical Review Letters **125**, 011102 (2020).
URL <https://link.aps.org/doi/10.1103/PhysRevLett.125.011102>
- [Tai21] S. C. Tait. *Studies of Mechanical and Optical Properties of Thin Film Coatings for Future Gravitational Wave Detectors*. Dissertation, University of Glasgow (2021).
URL <https://theses.gla.ac.uk/82514>
- [Tel12] F. Tellkamp. *PLD-Grown Thin Film Saturable Absorbers*. Dissertation, Universität Hamburg (2012).
- [Ter20] L. Terkowski, I. W. Martin, D. Axmann, M. Behrendsen, F. Pein *et al.* *Influence of deposition parameters on the optical absorption of amorphous silicon thin films*. Physical Review Research **2**, 033308 (2020).
URL <https://link.aps.org/doi/10.1103/PhysRevResearch.2.033308>
- [Tho95] K. S. Thorne. *Gravitational waves*. arXiv preprint, gr-qc/9506086 (1995).
URL <https://arxiv.org/abs/gr-qc/9506086>
- [Top96] K. A. Topp and D. G. Cahill. *Elastic properties of several amorphous solids and disordered crystals below 100 K*. Zeitschrift für Physik B Condensed Matter **101** (2), 235–245 (1996). ISSN 1431-584X.
URL <https://doi.org/10.1007/s002570050205>
- [Vaj21] G. Vajente, L. Yang, A. Davenport, M. Fazio, A. Ananyeva *et al.* *Low Mechanical Loss TiO₂ : GeO₂ Coatings for Reduced Thermal Noise in Gravitational Wave Interferometers*. Physical Review Letters **127**, 071101 (2021).
URL <https://link.aps.org/doi/10.1103/PhysRevLett.127.071101>
- [Vil10] A. E. Villar, E. D. Black, R. DeSalvo, K. G. Libbrecht, C. Michel *et al.* *Measurement of thermal noise in multilayer coatings with optimized layer thickness*. Physical Review D **81**, 122001 (2010).
URL <https://link.aps.org/doi/10.1103/PhysRevD.81.122001>

- [Vla18] K. V. Vlasova, A. I. Makarov, N. F. Andreev, and A. Y. Konstantinov. *High-sensitive absorption measurement in transparent isotropic dielectrics with time-resolved photothermal common-path interferometry*. *Applied Optics* **57** (22), 6318–6328 (2018).
URL <http://opg.optica.org/ao/abstract.cfm?URI=ao-57-22-6318>
- [Wae13] S. H. Waeselmann, S. Heinrich, C. Kränkel, and G. Huber. *Structural and optical properties of epitaxially grown Nd³⁺-doped InYO₃ thin films on Lu₂O₃*. In: *2013 Conference on Lasers and Electro-Optics - International Quantum Electronics Conference* (Optica Publishing Group, 2013), CE_P_1.
URL http://opg.optica.org/abstract.cfm?URI=CLEO_Europe-2013-CE_P_1
- [Wae16] S. H. Waeselmann. *Waveguiding and Laser Action in Rare-Earth-Doped Sesquioxide and Sapphire Films*. Dissertation, Universität Hamburg (2016).
- [Yam15] W. Yam, S. Gras, and M. Evans. *Multimaterial coatings with reduced thermal noise*. *Physical Review D* **91**, 042002 (2015).
URL <https://link.aps.org/doi/10.1103/PhysRevD.91.042002>
- [Zan77] P. J. Zanzucchi, C. R. Wronski, and D. E. Carlson. *Optical and photoconductive properties of discharge-produced amorphous silicon*. *Journal of Applied Physics* **48** (12), 5227–5236 (1977).
URL <https://doi.org/10.1063/1.323553>

Acknowledgements

Here, I would like to thank all people, who made this thesis possible and supported me during my work at the University of Hamburg.

A big thanks goes towards my supervisor Roman Schnabel, who provided the working space, secured some funding necessary for my project and allowed me to pursue my doctoral thesis in his working group.

I especially want to thank Jessica Steinlechner, who devised or greatly inspired most of the presented scientific research about coatings for gravitational wave detectors. I also want to thank her for the great cooperation, scientific discussions and advises she provided as well as for the funding she secured.

Next, I would like to thank Daniel Axmann, Felix Pein and in particular Malte Behrendsen, who provided great help with the PLD system during their work on their respective bachelor and master theses.

Another thank goes towards Julian Gurs and Tobias Schoon for providing the 2128 nm light for my absorption measurements using the Hamburg PCI system.

Thanks to the members of the Non-linear Quantum optics working group for their general support, for creating a friendly, productive working environment and for the good time I had in the past years.

I also want to thank the members of the gravitational wave working groups at the University of Glasgow and Maastricht University, with whom I closely collaborated.

I would like to thank Oliver Gerberding for agreeing to provide the second assessment of this thesis.

Finally, a big thanks goes towards my family and friends, who were always very supportive during my whole time at the University.

Eidesstattliche Versicherung / Declaration on oath

Hiermit versichere ich an Eides statt, die vorliegende Dissertationsschrift selbst verfasst und keine anderen als die angegebenen Hilfsmittel und Quellen benutzt zu haben.

Hamburg, den 22.07.2022

Unterschrift des Doktoranden